Dissertation

Measurement of the LHC beam profile using the Beam Gas Vertex detector

Prepared under the supervision of

Christoph SCHWANDA (University supervisor, TU Wien)

Christos ZAMANTZAS (CERN supervisor, BE-BI-BL)

Sotirios VLACHOS (Project leader, CERN, BE-BI-BL)

submitted to Technischen Universität Wien

Faculty of Physics

by

Dipl.-Ing. Benedikt Würkner, BSc

Successfully defended in Vienna on the 20th of November 2019

Committee:

- Univ. Prof. Dr. Helmut LEEB (dean of studies)
- Privatdoz. Dr. Christoph SCHWANDA (PhD supervisor)
- Dr. Stephen GIBSON (external reviewer and examiner)
  Additionally
- Dr. Leonid RIVKIN (external reviewer)

TECHNISCHE UNIVERSITÄT WIEN

Abstract

Measurement of the LHC beam profile using the Beam Gas Vertex detector

by Dipl.-Ing. Benedikt WÜRKNER, BSc

The Beam Gas Vertex (BGV) demonstrator was developed for the Large Hadron Collider (LHC) to demonstrate the feasibility of a beam profile measurement device using a tracking detector to reconstruct beam-gas interactions. It has been successfully installed on beam 2 in 2015. If the evaluation of the concept using the demonstrator is successful, the design will be optimized, manufactured and installed on both beams for the HL-LHC upgrade that will be performed between 2024 and 2026.

My main contributions to the BGV project were the analysis of data taken by the detector, optimization of the reconstruction algorithm based on this data, the development and qualification of the beam size measurement algorithms, the alignment of the detector as well as the development of adequate monitoring.

As a first step the applicability of the usage of beam-gas interactions for beam size measurements was shown. The results showed that the assumed number of tracks per interaction detected by the setup was too low to apply vertexing as the method of measuring the beam size. Thus the correlation method was used to calculate the beam size and all the properties of the BGV were qualified using this method. It could be shown, that the achievable precision of the BGV depends on the number of events acquired down to a limit of a few μm. Futhermore I was able to measure many different kinds of beams allowing for the characterization of the BGV in changing conditions. It has been shown, that the BGV is capable of performing bunch by bunch measurements as well as averaged results with the limit for the number of bunches that can be acquired at the same time currently determined by the available computing capacity.

As a final step the results acquired with the BGV were compared to other beam size measurement devices already installed in the LHC.

TECHNISCHE UNIVERSITÄT WIEN

Zusammenfassung

Measurement of the LHC beam profile using the Beam Gas Vertex detector

von Dipl.-Ing. Benedikt WÜRKNER, BSc

Der Strahl-Gas-Vertex (Beam Gas Vertex, BGV) Detektor ist Messgerät am LHC (Large Hadron Collider *Großer Hadronen Beschleuniger*), das entwickelt wurde um die Anwendbarkeit der Messung von Strahl-Gas Kollisionen als Methode zur Bestimmung des Strahlprofils zu bestätigen. Die Installation am Strahlrohr 2 des LHC wurde 2015 erfolgreich abgeschlossen. Mittelfristig ist das Ziel, dass im Falle einer erfolgreichen Bestätigung das Design verbessert wird und dann zwei neue BGV hergestellt und auf beiden Strahlrohren des LHC installiert werden. Dies soll zwischen 2024 und 2026 durchgeführt werden, da der LHC im Rahmen des HL-LHC (High Luminosity LHC) Upgradeprogramms ebenfalls verbessert wird.

Der Hauptteil meiner Arbeit und somit mein Beitrag zum Projekt waren die Datenanalyse der genommenen Daten, die Anpassung des Rekonstruktionsalgorithmus basierend auf den genommenen Daten, die Entwicklung und Qualifikation des die Strahl-Größe bestimmenden Algorithmus, die präzise Positionsbestimmung des Detektors und die darauf basierenden Korrekturen sowie die Entwicklung von passenden Grafiken zur Darstellung der Ergebnisse.

Als ersten Schritt habe ich die Anwendbarkeit der Methode anhand von gemessenen Daten nachgewiesen. Die Resultate haben gezeigt, dass die Anzahl an Spuren pro Strahl-Gas Kollision zu gering ist um mittels Vertexrekonstruktion die Strahlgröße mit ausreichender Genauigkeit zu berechnen. Daher wurde eine zweite Methode untersucht, die sogenannte Korrelationsmethode. Diese erlaubt es anhand der Korrelation zwischen Spuren des selben Ereignisses die Strahlgröße zu bestimmen und ist dabei annähernd unabhängig von der Messgenauigkeit. Dies konnte auch nachgewiesen werden, da unter Anwendung der Korrelationsmethode die statistische Messgenauigkeit nur von der Anzahl der gemessenen Ereignisse abhängt bis zu einem Limit von ein paar μm. Weiters war es mir möglich viele verschiedene Strahlarten zu messen und dadurch den BGV in vielen verschiedenen Ausgangslagen zu charakterisieren.

Es konnte gezeigt werden, dass der BGV in der Lage ist, den Strahl paketweise zu messen sowie natürlich auch den Durchschnitt über alle Pakete. Das momentane Limit für die maximale Anzahl an Paketen die individuell gemessen werden können ist nur von der vorhandenen Rechenkapazität limitiert und wurde bereits im Rahmen des 2019/20 Upgradezyklus verbessert.

Als letzten Schritt wurden die Ergebnisse mit anderen Strahlmessgeräten verglichen.

Acknowledgements

Writing a PhD was the longest project I have undertaken until now and I wouldn't have managed without the support of numerous people that have helped me along the way.

I am very grateful to have had the opportunity to conduct my PhD at CERN. Doing so allowed me to get an in-depth view on contemporary research in the larges particle accelerator laboratory of the world and has advanced my academic knowledge tremendously. But CERN is not just a place, its also people and a special mindset of furthering the knowledge of humanity. Working in such an environment can have a profound effect on ones self and on the way one looks at the world. There are many people that I have worked and interacted with during my time at CERN and I would like to now thank a few of them individually.

Firstly I would like to thank my PhD supervisor Christoph Schwanda. Inspite of us being separated by a thousand kilometers he was always reachable for me and willing to help me with my thesis. His focus on the proper structuring and early definition of milestones is one of the main reasons I managed to finish my thesis within my intended timeframe.

Furthermore I would like to thank my section leader, Christos Zamantzas, for always having an open ear for any questions. His openness towards new ideas and his willingness to know what I was up to and how I was doing was a big part of why I felt welcome in the section from the beginning. I was also very happy that he always found time for a short chat with me inspite of basically everybody wanting to occupy his time.

My project leader, Sotirios Vlachos, who was always looking out for me and helped me wherever possible. I've learned a lot about statistics and scientific publications from him which helped me a lot in the progress of actually writing this thesis.

My office mate and project partner Andreas Alexopoulos, who taught me a lot about programming, cars, languages and life in general.

Robert Kieffer who brought his energetic spirit to the team coupled with his broad knowledge of CERN relevant topics and who always had some crazy idea up his sleeve to improve the system even further.

My BE-BI-BL section, especially all the people that over the years have joined me for lunch, coffee and lifechanging discussions. Namely, and please forgive me if I forgot somebody, Volker, Kristian, Francesco, Steve, Mathieu, Alen, Anders, Sara, Lorenzo and of course Tasos, how could anybody ever forget you? Furthermore to all the people we adopted in our lunch group, namely Matteo, Araceli, Joanna, Ishkhan and Giuseppe. I'll always have fond memories of all the interesting discussions we've had and am looking forward to seeing you again soon.

My family who encouraged me to move away for three years to pursue my dream of working at CERN even if it meant that I would see them a lot less. Danke, dass ihr immer Verständnis für meine großen Pläne habts.

Last, but definitely not least, possibly even most importantly, Lizzie who joined me on this adventure of living in Switzerland and who made it all work out inspite of the odds and language being against her. Thank you for coming with me my love, this meant more to me than I could ever express. You gave me the strength and stability to go through with my PhD and helped me deal with the stress of future plans and the ever looming problem of what to do after academia.

Contents

List of Figures

List of Tables

List of Abbreviations

BGV	**B**eam **G**as **V**ertex
TES	**T**ransient **E**vent **S**torage
LINAC	**LIN**ear **AC**celerator
PSB	**P**roton **S**ynchrotron **B**ooster
PS	**P**roton **S**ynchrotron
SPS	**S**uper **P**roton **S**ynchrotron
LHC	**L**arge **H**adron **C**ollider
HL-LHC	**H**igh-**L**uminosity **LHC**
ATLAS	**A** **T**oroidal **L**HC **A**pparatu**S**
ALICE	**A** **L**arge **I**on **C**ollider **E**xperiment
CMS	**C**ompact **M**yon **S**olenoid
LHCb	**LHC** **b**eauty Experiment
RF	**R**adio **F**requency
WS	**W**ire **S**canner
BSRT	**B**eam **S**ynchrotron **R**adiation **T**elescope
BGI	**B**eam **G**as **I**onization Detector
SiPM	**Si**licon **P**hoto**M**ultiplier
ADC	**A**nalog **D**igital **C**onverter
HLT	**H**igher **L**evel **T**rigger
GeoID	**Geo**metric **ID**

For my Family

Chapter 1

Introduction

1.1 The BGV - A Demonstrator

The LHC Beam Gas Vertex (BGV) detector is a non-invasive beam profile monitor envisioned to be used as part of the high luminosity LHC upgrade (HL-LHC)[1]. The concept was originally developed as part of the LHCb experiment at CERN and the feasibility was first confirmed there before a dedicated detector was commissioned [2]. The current LHC BGV Demonstrator is constructed of parts taken from the LHCb experiment to reduce the costs of the setup as well as using the experties present in that collaboration.

The main goal was to demonstrate the feasibility and applicability of the working principles as a beam instrumentation device. To this end a dedicated detector was installed at beam 2 of the LHC. A detailed description of the detector layout can be found in chapter 3 on page 21.

1.2 Layout of work

In this thesis I will describe the design of the BGV detector and the measurements that can and have been performed.

The second chapter gives an overview of the accelerator complex at CERN with its current crown jewel, the LHC, where the BGV is installed.

The third chapter describes the BGV detector in detail including hardware design considerations, simulation and data processing

The fourth chapter goes into details about the data selection, treatment and some basic statistical information regarding the nature of the data.

The fifth chapter describes the beam profile measurement methodology, especially the correlation method, and how the results are obtained.

In the sixth chapter the results of the two data taking years are presented and compared to other beam size measurement devices.

Finally in the seventh chapter a summary is given and the knowledge that could be relevant for the future final system is presented.

My main contributions to the BGV project were

The implementation of monitoring algorithms for data taken with the BGV, previously only monitors comparing simulated data with reconstructed data were implemented. As a part of this the relevant plots needed to be chosen, the required data exported and displayed.

Implementation of the beam size measurement algorithm, the correlation method, and the corresponding methodology of independent slices in time

The alignment of the detector planes with respect to each other and the beam reference system using only the relative information available to them.

Chapter 2

The CERN accelerator complex

This chapter covers the basics of particle accelerators including the main components of synchrotrons (radio frequency cavities and bending magnets). A simple linear approximation for the particle motion is taken to develop the equations describing the motion of particles along the reference beam orbit. As a part of this important accelerator concepts such as the beta function and normalized emittance are introduced. Furthermore the accelerator chain supplying the LHC is discussed and the chapter finishes with a description of existing beam instrumentation devices that were used to evaluate the performance of the BGV demonstrator.

2.1 Accelerator physics

2.1.1 Energy mass equivalence

The rest mass of an elementary particle can be represented as an Energy according to $E = m \cdot c^2$ [3].

The commonly used definition of a particles mass is therefore $m = \frac{E}{c^2}$ with the units $\frac{\mathrm{GeV}}{(\mathrm{m\,s^{-1}})^2}$ where commonly the constant c is used as a unit ($c = 1$). Using this the rest mass of the electron becomes $m_e = 0.5\,\mathrm{MeV}$ and the rest mass of the proton becomes $m_p = 938\,\mathrm{MeV}$. Thus it requires a minimum of the respective energy to create a given particle.

Colliding two particles of a given mass in the rest system of the particles allows for all their kinetic and rest energy to be used for the creation of particles. The probability for any given particle to emerge from a collision is defined as the branching fraction of the possible particles. These can also be predicted by physics models making them a very attractive possibility to check how well a theory describes reality.

To generate heavier particles from the only two known stable particles (electron and proton) one needs to accelerate them to energies high enough to create the desired particle(s) at a sufficiently high probability.

2.1.2 Basics of particle acceleration

A charged particle of charge e is subject to a force according to Lorentz' law:

$$\vec{F} = e(\vec{E} + \vec{v} \times \vec{B}) \tag{2.1}$$

wherein $\vec{E}$ and $\vec{B}$ are the electric and magnetic field vectors and $\vec{v}$ is the velocity of the particle. Longitudinal electric fields can therefore be used to accelerate (or decelerate) a charged particle in the direction of the electric field gradient while magnetic fields can be used to apply a perpendicular force to change the particle's trajectory.

A particle of one elementary charge passing through an electrical potential difference of 1 V gains (or deposits) an energy of 1 eV which translates into a change of momentum. This principle is applied in particle accelerators to accelerate a particle. In the case of the accelerators used at CERN, which are relevant for this thesis, this is done using radio frequency (RF) cavities.

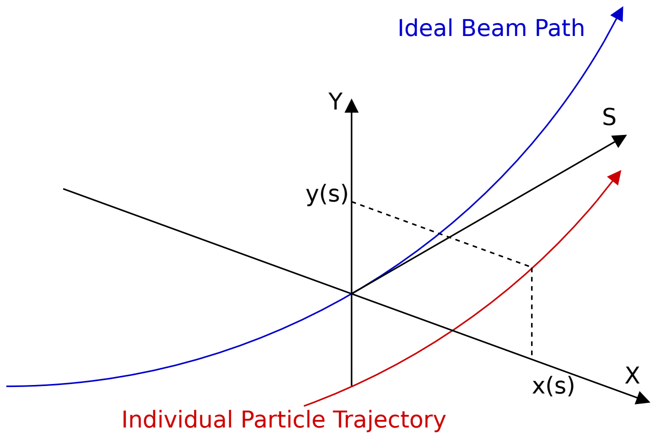

FIGURE 2.1: Coordinate system of the beam. The coordinate system follows the beam trajectory along s with the x coordinate being perpendicular to the trajectory while pointing away from the centre of the accelerator and the y coordinate pointing upwards.

The most important magnets used in particle accelerators are dipoles and quadrupoles for guiding and focusing the particles respectively. The coordinate system is usually defined along the particle trajectory with the position given as s and the perpendicular components for any s given by $x(s)$ and $y(s)$ respectively (see figure 2.1). By design the magnetic field has a null component in the s direction and therefore it can be expressed as

$$\vec{B} = B_x\vec{i} + B_y\vec{j} \tag{2.2}$$

with $\vec{i}$ and $\vec{j}$ as the unit vectors of the transverse plane.

Expanding the x and y to the first order gives

$$B_x = B_x(0,0) + \frac{\partial B_x}{\partial x}x + \frac{\partial B_x}{\partial y}y \tag{2.3}$$

$$B_y = B_y(0,0) + \frac{\partial B_y}{\partial x}x + \frac{\partial B_y}{\partial y}y \tag{2.4}$$

the field components in a linear form which will be used to develop the beam motion equations.

Dipole magnets are designed to provide a constant field B_y in the gap of the magnet where the beam pipe is placed. The bending radius ρ of a particle with change e and momentum p travelling in the x-plane comes from the equilibrium between the centrifugal and centripedal Lorentz forces

$$\rho = \frac{p}{eB_y}. \tag{2.5}$$

Quadrupole magnets are designed to have a gradient field leading to a change in force applied based on the particles position. The force rises linearly with the distance from the centre. From Maxwell's equation $\vec{\nabla} \times \vec{B} = 0$ it follows that

$$\frac{\partial B_x}{\partial y} = \frac{\partial B_y}{\partial x} \tag{2.6}$$

which leads to a quadrupole focusing in one axis while de-focusing in the other. By placing two quadrupoles with alternated polarities consecutively in an accelerator system a net focusing effect can be achieved in both transverse directions. The most common structure is the so-called FODO cell with a horizontally focusing (F) quadrupol, followed by a drift space (O), followed by a horizontally defocusing (D) quadrupole which is in turn again followed by another drift-space (0). The length of the required drift-space can be calculated from geometrical optics and needs to be small compared to the magnets focal length for a net focusing effect.

The space between the FODO cells consists of either dipoles to bend the particles on a trajectory around the accelerator ring or of straight sections where experiments or beam instrumentation devices are positioned. Additional higher order magnets (sextupoles, octopoles, ...) are also added to the accelerator to correct for imperfections of the respective lower order magnets. Their higher order corrections are beyond the scope of this thesis which will only consider a linear approximation.

To develop a mathematical formulation for a FODO cell we will now only consider one plane of the transformation performed by a quadrupole since the perpendicular plane is equivalent to a DOFO cell. The transformations can be seen like the transformation performed by a thin lens which can be represented as the following matrices for optical lens systems

$$\begin{bmatrix} 1 & 0 \\ -\frac{1}{f} & 1 \end{bmatrix} \qquad \begin{bmatrix} 1 & 0 \\ \frac{1}{f} & 1 \end{bmatrix} \qquad \begin{bmatrix} 1 & L \\ 0 & 1 \end{bmatrix} \tag{2.7}$$

for focusing, defocusing and propagation respectively.

Constructing a FODO cell out of these matrices gives:

$$\begin{bmatrix} 1 & L \\ 0 & 1 \end{bmatrix} \cdot \begin{bmatrix} 1 & 0 \\ \frac{1}{f} & 1 \end{bmatrix} \cdot \begin{bmatrix} 1 & L \\ 0 & 1 \end{bmatrix} \cdot \begin{bmatrix} 1 & 0 \\ -\frac{1}{f} & 1 \end{bmatrix} = \begin{bmatrix} 1 - \frac{L}{f} - \frac{L^2}{f^2} & 2L + \frac{L^2}{f} \\ -\frac{L}{f^2} & 1 + \frac{L}{f} \end{bmatrix} \tag{2.8}$$

Consequently the whole lattice of an accelerator can be constructed out of similar matrices leading to a matrix M describing all the elements of an accelerator. The description of the particle motion after n revolutions is given by M^n. To have a stable motion of particles with the initial conditions x_0 and x'_0 the quantity

$$M^n \begin{bmatrix} x_0 \\ x'_0 \end{bmatrix} \tag{2.9}$$

must remain finite for all n. As shown in [4] the stability condition for this is simply

$$-1 \leq \frac{1}{2}\text{Trace}(M) \leq 1 \tag{2.10}$$

which applied to equation (2.8) corresponds to

$$-1 \leq 1 - \frac{1}{2}\left(\frac{L}{f}\right)^2 \leq 1 \tag{2.11}$$

which simplifies to:

$$\left|\frac{L}{2f}\right| \leq 1. \tag{2.12}$$

This gives the rather simple condition that the focal length f needs to be at least half the drift space length L.

2.1.3 Transverse linear motion

The reference orbit described in the previous section is the mathematically perfect orbit around which the magnetic lattice is constructed. If a particle's starting position (x_0,y_0) and slope (x'_0,y'_0) are non-zero it performs oscillations around the reference orbit. These so-called *Betatron oscillations* will be described in this section using a simplified first order approximation with decoupled transverse planes (i.e. independent x and y). A complete derivation is given in [4] with the most important results given here for completeness.

Taking the Lorentz law in the absence of an electric field one starts with

$$\frac{d\vec{p}}{dt} = e\vec{v} \times \vec{B}. \tag{2.13}$$

By neglecting the radiative (synchrotron) losses the momentum can be represented as $\vec{p} = \gamma m\dot{\vec{R}}$ with $\vec{R} = (\rho + x, y)$ as the position vector of the particle. The left hand side of equation (2.13) thus becomes

$$\frac{d\vec{p}}{dt} = \frac{d}{dt}\gamma m\dot{\vec{R}} = \gamma m\ddot{\vec{R}}. \tag{2.14}$$

After a lengthy derivation which can be found in [4, p. 66] we arrive at the equations of motion in the two transverse planes

$$x'' + \left[\frac{1}{\rho^2(s)} + \frac{1}{B\rho}\frac{\partial B_y(s)}{\partial x}\right]x = 0 \tag{2.15}$$

$$y'' - \frac{1}{B\rho}\frac{\partial B_y(s)}{\partial x}y = 0 \tag{2.16}$$

where the time-dependence of the motion equation has been replaced by a dependence on s, the position along the reference orbit. An additional important point is the introduction of the parameter $B\rho$ which is called *magnetic rigidity* which is equal to the ratio p/e (follows from equation (2.5) on page 4).

The term $\frac{1}{\rho^2(s)}$ is the "centripetal" term originating from the x plane being the bending plane. For large accelerators it is usually small in comparison to the gradient term.

The motion equations both resemble a simple harmonic oscillator

$$x'' + K_1(s)x = 0 \tag{2.17}$$

$$y'' + K_2(s)y = 0 \tag{2.18}$$

with the difference, that the "spring constant" depends on the position in the accelerator. The parameter K_i can be considered constant within each component of the accelerator leading to the solutions of an harmonic oscillator being applicable in each individual component.

These solutions can be represented as matrices in the same way as equation (2.8) on page 5 with the solution for $K = 0$ being the matrix for a drift-space of length L

$$\begin{bmatrix} x \\ x' \end{bmatrix}_{out} = \begin{bmatrix} 1 & L \\ 0 & 1 \end{bmatrix} \begin{bmatrix} x \\ x' \end{bmatrix}_{in}. \tag{2.19}$$

For $K > 0$ over a distance L the solution for the equation of motion is a harmonic oscillator as given by

$$\begin{bmatrix} x \\ x' \end{bmatrix}_{out} = \begin{bmatrix} \cos(\sqrt{K}L) & \frac{1}{\sqrt{K}}\sin(\sqrt{K}L) \\ -\sqrt{K}\sin(\sqrt{K}L) & \cos(\sqrt{K}L) \end{bmatrix} \begin{bmatrix} x \\ x' \end{bmatrix}_{in}, \tag{2.20}$$

whereas for $K < 0$ the result is

$$\begin{bmatrix} x \\ x' \end{bmatrix}_{out} = \begin{bmatrix} \cosh(\sqrt{|K|}L) & \frac{1}{\sqrt{|K|}}\sinh(\sqrt{|K|}L) \\ -\sqrt{|K|}\sinh(\sqrt{|K|}L) & \cosh(\sqrt{|K|}L) \end{bmatrix} \begin{bmatrix} x \\ x' \end{bmatrix}_{in}. \tag{2.21}$$

Consequently the optical lattice of an accelerator can be constructed by placing a combination of elements with appropriate K in distances L so that the stability criterion equation (2.10) on page 5 is fulfilled.

A second solution for the linear motion equation can be found by using Hill's equation [5] which correspond to the solutions for a harmonic oscillator with a periodic function as the constant. This equation is applicable for the case that for the equation of motion

$$x'' + K(s)x = 0 \tag{2.22}$$

exists a distance C such that

$$K(s + C) = K(s). \tag{2.23}$$

This condition is fulfilled in circular accelerators giving way to the applicability of this solution. The repetition distance C can be as large as the circumference of the accelerator but is typically of the size of a FODO cell.

The solution, as provided by Hill, is of the form

$$x = Aw(s)\cos[\psi(s) + \delta] \tag{2.24}$$

with A and δ as the two constants of integration indicating the initial conditions. One can require $w(s)$ to be a periodic function with the periodicity C to fulfill the required conditions.

Substituting the general solution equation (2.24) in equation (2.17) on the facing page gives

$$0 = A(w'' - w\psi'^2 + Kw)\cos(\psi + \delta) - A(w\psi'' + 2w'\psi')\sin(\psi + \delta). \tag{2.25}$$

Since the functions w and ψ need to be independent of δ to be a general solution (since δ depends on the initial conditions) we require that the coefficients of the sine and cosine vanish independently. Taking the coefficient of the sine term and multiplying by w gives

$$w^2\psi'' + 2ww'\psi' = (w^2\psi')' = 0 \tag{2.26}$$

which can also be expressed as

$$\psi' = \frac{k}{w(s)^2} \tag{2.27}$$

with k as an arbitrary constant of integration. Inserting equation (2.27) on the previous page into the coefficient of the cosine in equation (2.25) on the preceding page yields the differential equation that w must satisfy:

$$w^3(w'' + Kw) = k^2. \tag{2.28}$$

If one rewrites equation (2.24) on the previous page to

$$x = w(s)(A_1 \cos\psi + A_2 \sin\psi) \tag{2.29}$$

with the derivative

$$x' = \left(A_1 w' + \frac{A_2 k}{w}\right)\cos\psi + \left(A_2 w' - \frac{A_1 k}{w}\right)\sin\psi) \tag{2.30}$$

then the initial conditions x_0, x'_0 at $s = s_0$ give the constants A_1 and A_2 as follows

$$A_1 = \frac{x_0}{w} \tag{2.31}$$

$$A_2 = \frac{x'_0 w - x_0 w'}{k}. \tag{2.32}$$

This motion equation can also be represented using the matrix form as used previously leading to

$$\begin{bmatrix} x \\ x' \end{bmatrix}_{s_0+C} = \begin{bmatrix} \cos\Delta\psi_C - \frac{ww'}{k}\sin\Delta\psi_C & \frac{w^2}{k}\sin\Delta\psi_C \\ \frac{(ww'/k)^2-1}{w^2/k}\sin\Delta\psi_C & \cos\Delta\psi_C + \frac{ww'}{k}\sin\Delta\psi_C \end{bmatrix} \begin{bmatrix} x \\ x' \end{bmatrix}_{s_0}. \tag{2.33}$$

The phase $\Delta\psi_C$ is calculated by integrating along the path by the period C

$$\psi(s_0 \to s_0 + C) = \Delta\psi_C = \int_{s_0}^{s_0+C} \frac{k\,ds}{w^2(s)}. \tag{2.34}$$

Due to the periodic nature of $w(s)$ the integral does not depend on the choice of s_0.

Taking a close look at equation (2.33) it becomes apparent that the main dependencies w and w' both scale with the arbitrary constant k. We therefore introduce the following variables which were first developed by Courant and Snyder [6]

$$\beta(s) \equiv \frac{w^2(s)}{k}, \tag{2.35}$$

$$\alpha(s) \equiv -\frac{1}{2}\frac{d\,\beta(s)}{ds}, \tag{2.36}$$

$$\gamma(s) \equiv \frac{1 + \alpha(s)^2}{\beta(s)}. \tag{2.37}$$

Placing these in equation (2.33) yields

$$\begin{bmatrix} x \\ x' \end{bmatrix}_{s_0+C} = \begin{bmatrix} \cos\Delta\psi_C + \alpha\sin\Delta\psi_C & \beta\sin\Delta\psi_C \\ \gamma\sin\Delta\psi_C & \cos\Delta\psi_C - \alpha\sin\Delta\psi_C \end{bmatrix} \begin{bmatrix} x \\ x' \end{bmatrix}_{s_0} \tag{2.38}$$

This gives the general solution of the equation of motion which contains the periodic beta function hence the name.

Updating equation (2.24) on page 7 the equation of motion can now be written as

$$x = A\sqrt{\beta(s)}\cos[\psi(s) + \delta] \tag{2.39}$$

with the constant k absorbed into the constant A.

2.1.4 Beta function

The Courant-Snyder parameter $\beta(s)$ is a periodic function with a periodicity C which is historically also called betatron function named after the betatron oscillations of a bunch of particles. It can be used to calculate the phase advance in an accelerator by using equation (2.34) on the preceding page with

$$\psi(s_1 \to s_2) = \int_{s_1}^{s_2} \frac{ds}{\beta(s)}. \tag{2.40}$$

To calculate the number of betatron oscillations performed during a full turn of the accelerator, the so-called *tune*, one needs to calculate the ring integral of equation (2.40) like

$$\nu \equiv \frac{1}{2\pi} \oint_s \frac{ds}{\beta(s)}. \tag{2.41}$$

Following from equation (2.39) it is clear that the local amplitude of the particles' oscillation around the reference orbit depends on $\sqrt{\beta(s)}$. Therefore the extent of the beam at a given location in the accelerator can be given as a function of β which will be discussed in the next section.

2.1.5 Emittance

After only dealing with the movement of a single particle in a particle accelerator so far, we will now characterize an ensemble of particles. Such an ensemble of particles can generally be described by a density function in six dimensions,

$$\rho = \varphi(x, p_x, y, p_y, s, E) \tag{2.42}$$

in which x, y, s are the three space coordinates of the three planes. p_x, p_y are the momenta in the corresponding directions while E is the particle energy.

Using $E = \gamma m_0 c^2$ the relativistic particle momentum can be represented as

$$p = \gamma m_0 v = \frac{E \cdot v}{c^2} \tag{2.43}$$

with $p_x \approx px'$ and $p_y \approx py'$ as the momenta in the respective directions. For the situation of stable energy in an accelerator the momenta are constant and therefore commonly replaced by the slopes of the respective coordinates

$$\rho = \varphi(x, x', y, y', s, E). \tag{2.44}$$

Since we continue to neglect the coupling between the three axis we can consider this six dimensional space as three independent sub-spaces (x, x'), (y, y') and (s, E).

We will now develop the transverse phase space (x, x') which can in the same way be applied to the (y, y') phase space.

If we again start from equation (2.39) on the preceding page and remove the trigonometric functions by at first constructing

$$\alpha(s)x(s) + \beta(s)x'(s) = -A\sqrt{\beta(s)}\sin[\psi(s) + \delta] \tag{2.45}$$

and then squaring both equations we get

$$x^2 = A^2\beta(s)\cos^2[\psi(s) + \delta] \tag{2.46}$$

$$\alpha(s)^2x(s)^2 + \beta(s)^2x'(s)^2 + 2\alpha(s)\beta(s)x(s)x'(s) = A^2\beta(s)\sin^2[\psi(s) + \delta]. \tag{2.47}$$

Summing the two equations gives

$$x^2 + \alpha(s)^2x(s)^2 + \beta(s)^2x'(s)^2 + 2\alpha(s)\beta(s)x(s)x'(s) = A^2\beta(s) \tag{2.48}$$

which can be simplified to

$$A^2 = \gamma(s)x(s)^2 + 2\alpha(s)x(s)x'(s) + \beta(s)x'(s)^2 \tag{2.49}$$

which looks exactly like the equation for an ellipse

$$ax^2 + 2bxy + cy^2 = d. \tag{2.50}$$

From analytical geometry, the area of an ellipse is

$$\frac{\pi d}{\sqrt{ac - b^2}} \tag{2.51}$$

which for this case equals to

$$\frac{\pi A^2}{\sqrt{\beta\gamma - \alpha^2}} = \pi A^2. \tag{2.52}$$

The constant A^2 is called the *emittance* of the particle defined as

$$\varepsilon = A^2 = \frac{\text{Ellipse area}}{\pi}. \tag{2.53}$$

It follows that the area of the ellipse given by the Courant-Snyder parameters is constant under the given conditions (constant energy, linear approximation). Since the functions α, β and γ depend on the location s the actual shape of the ellipse depends on the current position along the accelerator but the area of the ellipse (i.e. the particle emittance) remains constant.

Extrapolating this behavior to many particles ([4] page 81) shows that for many particles equation (2.49) becomes

$$\gamma(s)x(s)^2 + 2\alpha(s)x(s)x'(s) + \beta(s)x'(s)^2 = \varepsilon_{\text{rms}}. \tag{2.54}$$

Following from the RMS value via the definition of the variance it also follows that

$$\varepsilon_{\text{rms}} = \frac{\sigma_x^2(s)}{\beta(s)} \tag{2.55}$$

with β the betatron function at the location s and σ_x the beam size. Consequently β and σ_x vary along the accelerator to respect the invariance of the emittance.

2.1.6 Normalized emittance

To consider the behavior of emittance during acceleration we need to move away from the previous assumption of constant energy. The divergence of a particle given by $x' = p_x/p_s$ depends on the ratio between transversal and longitudinal components of the momentum. During acceleration, which is performed using longitudinal electric fields, the longitudinal momentum is increased but the transverse component remains unchanged. A first order approximation of the momentum increase is therefore $\Delta p = \Delta p_s$ with a divergence increment given by

$$x' + \Delta x' = \frac{p_x}{p_s + \Delta p_s} = \frac{p_x}{p_s \left[1 + \frac{\Delta p_s}{p_s}\right]} \approx x' \left[1 - \frac{\Delta p}{p}\right] \tag{2.56}$$

which leads to

$$\Delta x' = -x' \frac{\Delta p}{p}. \tag{2.57}$$

The *normalized emittance* is generally defined as:

$$\varepsilon_n = \gamma_L \frac{v}{c} \varepsilon = \gamma_L \beta_r \frac{1}{\beta} \left[\sigma^2 - \left(D \frac{dp}{p}\right)^2\right] \tag{2.58}$$

where the Lorentz factor $\gamma_L = E/(m_0 c^2)$ is the ratio between the energies of the particles and their rest mass, while the relativistic factor $\beta_r = v/c$ scales their velocity to the speed of light. D is the dispersion function describing off-momentum particles.

The normalized emittance is invariant with the momentum and location making it a true invariant along the whole length of the accelerator and during its operation cycle. This provides the great advantage that it can be measured by independent instruments based on different parameters at individual locations and then compared.

2.1.7 Luminosity

As discussed in section 2.1.1 colliding two beams of particles in their centre of mass (cms) frame allows for their total kinetic energy to be converted into particles of higher mass. To this end beams of particles are made to circulate in opposite directions in particle colliders such as the LHC (section 2.2.5). Each collider has one or more interaction regions where the trajectories of the particles are made to intercept. When two particles collide many different reactions are possible, each is characterized by a cross-section σ which can be split into elastic and inelastic cross-section and depends on the centre of mass energy[7].

The interaction rate at the collision point depends on the total cross-section σ

$$\dot{n} = \mathcal{L} \cdot \sigma \tag{2.59}$$

and scales with the proportionality factor $\mathcal{L}$ called *luminosity*. The luminosity contains all the information of the actual beam parameters and is therefore a quantity depending solely on the accelerator and its configuration. It is therefore usually used to compare the production capabilities of accelerators with each other.

For two colliding bunches containing n_1 and n_2 particles at a crossing angle of zero with a repetition frequency f the luminosity is given by

$$\mathcal{L} = f \frac{n_1 n_2}{4\pi \sigma_x \sigma_y} \tag{2.60}$$

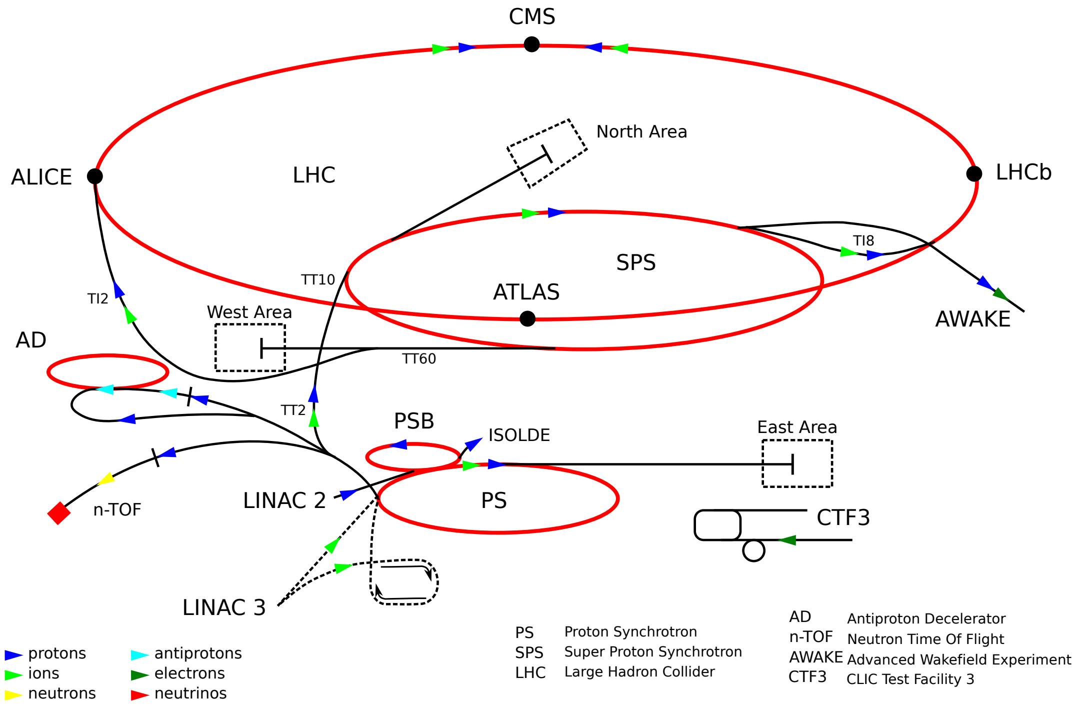

FIGURE 2.2: CERN accelerator complex

with σ_x and σ_y the standard deviations of the Gaussian beam profiles at the interaction point. This mathematical formulation for zero degrees of crossing angle is a geometric quantity that depends only on the overlap volume of the two beams. When the crossing angle is changed this overlap region changes. Additional beam-beam interactions can increase or lower this rate as well.

Luminosity is given in units of $cm^{-2}s^{-1}$ while the cross-section has the units of a surface usually given in *barn*[1] with $1\,\mathrm{b} = 1 \times 10^{-28}\,\mathrm{m}^2$.

Using equation (2.55) on page 10 it is now possible to represent the luminosity as a function of the transverse emittances ε_i and the betatron functions β_i^* at the interaction point leading to

$$\mathcal{L} = f \frac{n_1 n_2}{4\pi\sqrt{\varepsilon_x \beta_x^* \varepsilon_y \beta_y^*}} \tag{2.61}$$

2.2 Accelerators at CERN

The particle accelerator complex at CERN is composed of many individual accelerators that are tightly linked to efficiently accelerate particles in a multi stage approach. In figure 2.2 an overview over the full complex is given. In this section a short description of each accelerator is given with the main focus on the LHC where the BGV is located. The focus of the description is placed on the acceleration of protons since this is the most common scenario for the LHC and thus the BGV.

[1]Named after the farm building during the time of the Manhattan Project to have a secretive unit for the cross-section of a nucleus.

2.2.1 Linear Accelerator (LINAC)

The linear accelerator is the first step in the accelerator chain. Protons are accelerated using LINAC2 while LINAC3 is used for ions.

The first step before any acceleration can begin is the isolation of the protons. This is done by using a duoplasmatron [8] wherein a plasma is generated from hydrogen gas. Using electric fields the positively charged protons are extracted into the linear accelerator.

LINAC2 [9] is a 37 m long linear accelerator. It uses radio-frequency cavities structured in three drift tubes to accelerate protons from the duoplasmatron with a beam intensity of up to 180 mA which is currently the highest intensity achieved for a proton beam. Once the protons are accelerated up to an energy of 50 MeV they are injected into the Booster.

2.2.2 Booster (PSB)

The proton synchrotron booster was constructed to increase the number of protons the PS can receive [10]. It consists of four superimposed synchrotron rings that accept the 50 MeV protons coming from LINAC2 and accelerate them to 1.4 GeV. The circumference of the Booster is 157 m which is exactly one quarter of the PS circumference to allow for the injection of the four layers into the PS.

2.2.3 Proton Synchrotron (PS)

The construction of the proton synchrotron was finished in 1959 and it is therefore the longest running accelerator at CERN [11]. It has a circumference of 628 m and nowadays mostly accelerates protons coming from the PSB from 1.4 GeV to 26 GeV.

Additionally the PS is responsible for creating the bunch structure for the LHC by employing RF gymnastics [12] to split the six bunches, injected from the PSB in two iterations (4+2), into 72 bunches. To achieve this goal at injection energy each of the six bunches is split into three by increasing the harmonic of the PS from $h = 7$ to $h = 21$ leading to 18 filled buckets. This beam is accelerated to the nominal 26 GeV. On this plateau the harmonic is doubled twice consecutively leading to $h = 84$ with one bunch each in the first 72 buckets. This beam is then extracted towards the SPS.

2.2.4 Super Proton Synchrotron (SPS)

The SPS was the first accelerator built underground at CERN. It is located roughly 40 m below both french and swiss territory in a tunnel with 6.9 km circumference. After its commissioning in June 1976 the SPS was first used as a proton accelerator reaching energies of up to 400 GeV. Only a few years later, in 1981, it was modified to be used as a proton-antiproton collider. In 1991 the SPS was adapted again to allow for the acceleration of electrons and positrons for the LEP experiment while at the same time still providing protons for fixed target experiments.

The main upgrades for the SPS to be used as injector for the LHC were the upgrade and qualification of the 450 GeV beam energy as well as a new extraction system for these energies towards the two extraction lines leading to the LHC. All of the upgrades applied to the SPS for LHC operations are described in Ref. [13].

2.2.5 Large Hadron Collider (LHC)

The LHC is currently the largest particle accelerator on earth and is housed in a tunnel of 26.66 km circumference [14] located between 80 and 130 m underground. It was constructed in the tunnel which previously housed the LEP [15] accelerator and its construction was completed in 2007. Contrary to the previously described accelerators the LHC is designed as a collider with two beam pipes allowing for the acceleration of bunches with the same charge both clockwise and anti-clockwise at the same time. The main structural and functional component of the LHC is the superconducting dipole. Each of the 1232 dipoles is 14.3 m long and in total they make up 17.6 km of the LHC structure. Their main objective is to bend the particles on a trajectory around the accelerator as described in section 2.1.2 on page 3. Of the focusing quadrupoles 360 are installed in the ring and with their length of 3.3 m each they make up about 1.2 km of the LHC.

The LHC is split in eight equally spaced arcs with straight sections in between them. The arcs contain most of the magnets and bend the beam to form the full circle while the straight sections contain the experiments, injection and extraction kickers, RF cavities, beam instrumentation, collimators and more. Eight access shafts numbered clockwise starting in the south allow access to the straight sections of the accelerator tunnel. In four straight sections the beams are made to collide by directing them towards each other. These are the locations of the four experiments (1-ATLAS, 2-ALICE, 5-CMS, 8-LHCb). The remaining four access shafts allow access to other important components of the accelerator such as momentum cleaning (point 3), the RF cavities (point 4), the beam dump (point 6) and the betatron cleaning (point 7).

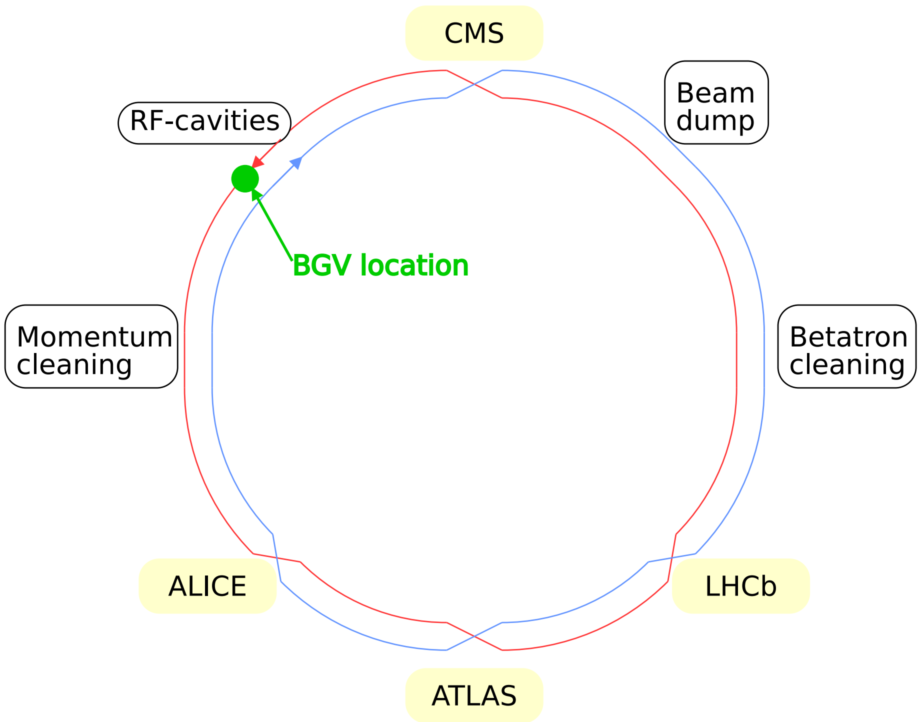

FIGURE 2.3: Overview of the LHC layout showing the location of the four Experiments as well as the location of the four additional access points.

The LHC is designed for the energy range from 450 GeV to 7000 GeV per beam but at the time of this thesis only a maximum of 6500 GeV has been achieved.

By design the revolution frequency is 11 245 Hz following from its circumference and the speed of the particles being basically the speed of light ($\beta = v/c = 0.999999989587645$).

The RF system of the LHC is operating at 400 MHz with a harmonic number of 26.66km/(c/400 MHz) = 35640 which equals the number of RF buckets. The tenfold increase in frequency is done to keep the space occupied by each RF bucket short and thereby limit the area a bunch can populate. Only the first of every 10 RF buckets is populated thus the LHC effectively runs at 40 MHz which is equal to a distance of about 7.5 m between filled buckets. Additionally of the 3564 buckets offered by the accelerator only 2808 can be filled with bunches due to limitations with the injection and extraction kicker magnets [16]. The rise-time of the injection kickers requires almost 1 µs (39 buckets) while the extraction kickers towards the beam-dumps need three times as long requiring for the last 119 buckets to be left empty. The final gap in the filling scheme is called the *abort gap* and is limited by the rise time of the extraction kickers towards the beam-dumps at full energy.

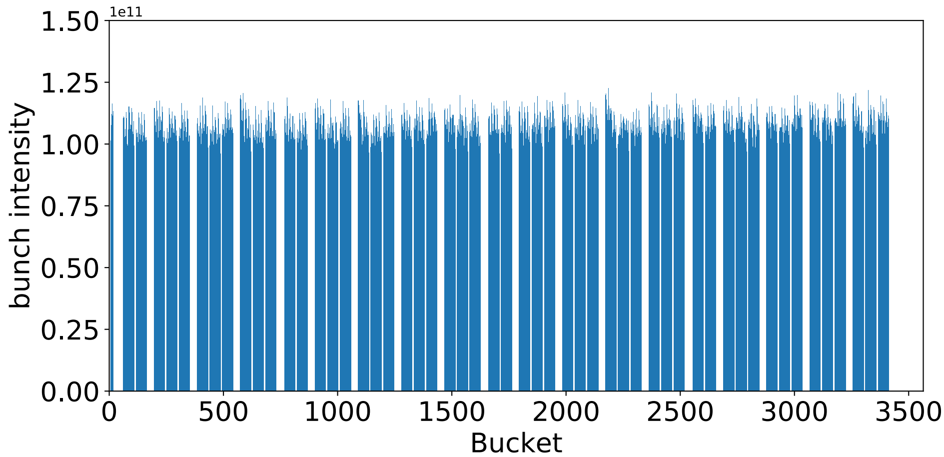

FIGURE 2.4: Filling scheme of fill 7334. The kicker rise times are nicely visible as the separations between the trains of particles. The abort gap at the end of the scheme is also clearly visible.

The filling procedure of the LHC requires the full accelerator chain to be working. At first a so-called pilot bunch is injected. A pilot bunch has 5×10^9 protons which is equals to the amount of charge that can be lost in a magnet without causing a quench[17]. Once the pilot is circulating in the LHC and the beam optics are confirmed, a first train of 12 nominal bunches is injected for additional checks. Once these are completed the nominal injection procedure starts which injects two or three trains of 48 bunches each into the LHC until 2556 bunches are circulating. Once the injection is finished the LHC is ramped from 450 GeV to 6.5 TeV over the course of around 20 min. Once the ramp is finished the so-called FLATTOP plateau is reached. The next step is called SQUEEZE, where a betatron squeeze is performed[18], before the beam is switched to ADJUST for small parameter adaptations and then finally to STABLE [19].

2.3 Beam optics and parameters for the BGV

The BGV demonstrator is located at point four of the LHC with the internal designation *UJ43/C-07L4*. A careful study of available locations was performed and the current location was finally chosen for it's similar β-values in x and y as well as their stability during the energy ramp (see figure 2.5).

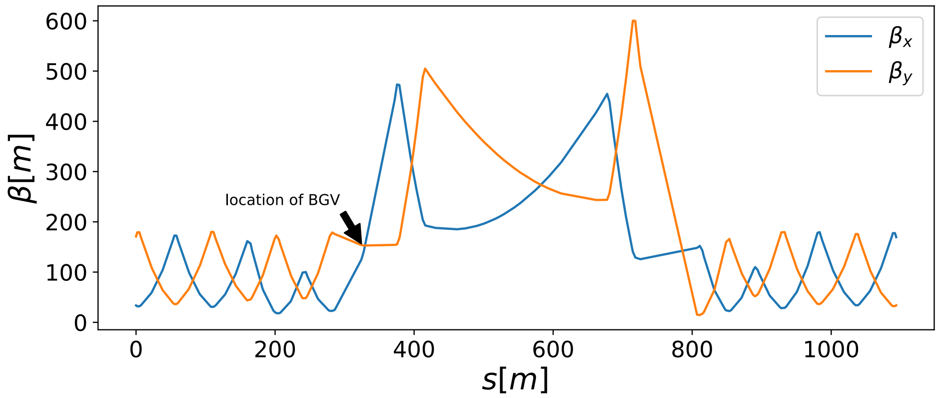

FIGURE 2.5: Plot of the β-function for 450 GeV at point 4 of the LHC for x and y of beam 2 showing the location chosen for the BGV very close to the crossing point of the two functions.

Due to the steep gradient of the β_x function at the location the value varies between 124 m to 132 m over the length of the BGV gas target chamber which introduces a 5 % error for the beam size in x.

From these β values follow the beam sizes the BGV needs to be able to measure. For an emittance of 2.5 µm (which is the target normalized emittance for HL-LHC[1]) one can calculate the expected sizes using

$$\sigma_x = \sqrt{\frac{\varepsilon_n \beta_x}{\gamma_R \beta}} \tag{2.62}$$

which follows from equation (2.58) on page 11.

The expected sizes are summarized in table 2.1.

Energy	β_x	β_y	$\sigma_x^{\text{expected}}$	$\sigma_y^{\text{expected}}$
450 GeV	132.09 m	153.35 m	829 µm	894 µm
6.5 TeV	132.04 m	153.27 m	218 µm	235 µm

TABLE 2.1: Table of beta values and estimated beam sizes at the BGV location for $\varepsilon_n = 2.5$ µm using equation (2.62),

2.4 Emittance measurement at the LHC

At the time of writing multiple different devices capable of measuring the beam profile are installed at the LHC. As given by equation (2.55) on page 10 by knowing the beta function at these locations the beam size obtained from the beam profile can be used to calculate the emittance. The currently installed instruments and their positions are given in table 2.2 and their methods of operation are explained in the following sections.

WS horizontal 1 (main)	LHC.BWS.5L4.B1H2
WS horizontal 2 (spare)	LHC.BWS.5L4.B2H2
WS vertical 1 (main)	LHC.BWS.5L4.B2V1
WS vertical 2 (spare)	LHC.BWS.5L4.B2V2
BSRT	LHC.BSRT.5L4.B2
BGI horizontal	LHC.BGIH.5R4.B2
BGI vertical	LHC.BGIV.5R4.B2
BGV	LHC.BGV.7L4.B2

TABLE 2.2: Emittance measurement devices at the LHC beam 2 and their designations

2.4.1 Wire scanner (WS)

The principle of functionality of a wire scanner is based on a thin wire which is, as the name suggests, used to scan the beam. This procedure is done perpendicular to the direction the beam is travelling in and therefore allows for the measurement of one transverse beam profile axis. To measure the full beam profile therefore two perpendicularly scanning WS are needed. The wire is moved at speeds of multiple metres per second limited by mechanical design constraints towards the actuators. The wire can either be moved by a linear actuator with a lower maximum speed (only a few meters per second) or a rotational motor capable of up to twenty meters per second. The speed of the wire directly limits the intensity that can be measured with it due to the energy transfer between the beam and the wire destroying the latter by either melting or sublimating the material. The position of linear actuators can be measured very precisely whereas the position for a rotating wire needs to be calculated from the reading of the motor shaft position and requires some additional effort.

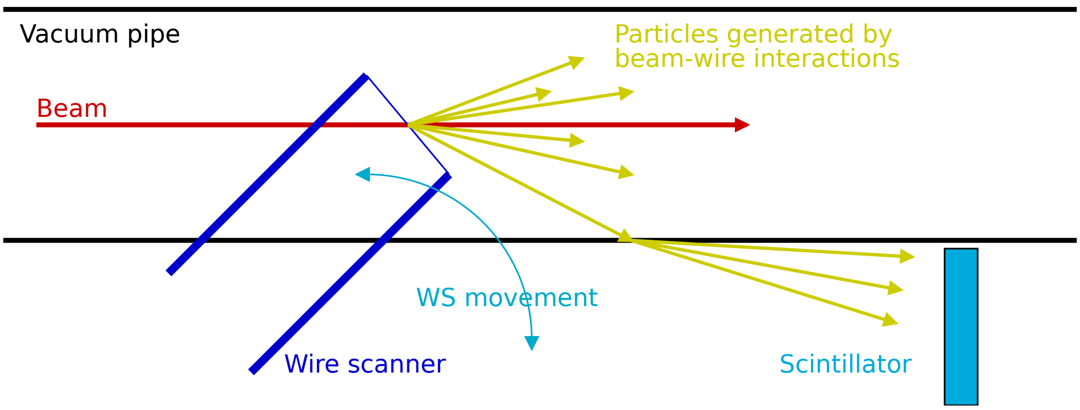

FIGURE 2.6: Schematic drawing of the principle of the wire scanner.

There are two possibilities to measure the beam based on the wire traversing it:

- Measurement of the secondary particle emission produced by the beam colliding with the wire which is proportional to the beam intensity at the wire's position. The secondary particles are measured by a scintillating detector see figure 2.6 on the preceding page.

- Current induced into the wire due to the beam particles creating secondary electron emission in the wire.

For both options the position measurement as well as the signal measurement are synchronized with the revolution frequency. The resulting measurements over the position of the wire gives the beam profile in the corresponding axis.

The operating principle of a wire scanner is in general destructive towards the beam but the effect is negligible if an adequate mode of operation is chosen [20]. Parameters that can be adapted are amongst others wire thickness, speed and material as well as the repetition frequency, the limits for the LHC are given in Ref. [21]. The monitoring of the wire position is the most difficult of the possible parameters and therefore requires the highest precision to keep the error of the WS measurement acceptable.

Generally wire scanners are considered to be very accurate due to the following parameters

- High resolution based on the accuracy of the wire position measurement (down to 1 µm).
- Direct measurement with the accuracy of the intensity solely based on the wire position measurement.
- Very small statistical and systematic errors and high repeatability of results.
- Paired with read-out electronics of sufficiently high speed the measurement can be performed on a bunch by bunch basis (currently in use in the LHC).

Of course there are some drawbacks that need to be considered:

- The resolution is determined by the wire diameter (36 µm for the LHC [22]).
- High energy depositions increase the chance of melting the wire which necessitates higher speeds. Higher speeds are detrimental to the resolution since fewer points are recorded per transition.

To summarize: The LHC has two WS per axis to enable redundancy and check for consistency, with the first being considered the main and the second a spare. When reducing the beam intensity the WS can produce very accurate beam profiles but for higher intensities and/or energies the wire speed needs to be increased reducing the precision. To monitor the emittance during physics fills of the LHC other devices are necessary that are not limited by higher intensities.

2.4.2 Beam synchrotron radiation telescope (BSRT)

Synchrotron radiation is emitted by a charged particle when it is accelerated perpendicular to its trajectory. Due to energy conservation the emission of radiation of course reduces the energy of the particles when they are bent. For the case of the acceleration being perpendicular to the velocity of the particle - as it is the case for dipoles - the total radiated power is given by

$$P_{\text{tot}} = \frac{q^2 a^2 \gamma^4}{6\pi\varepsilon_0 c^3}. \tag{2.63}$$

with q the particle charge and a the bending radius. Since $\gamma = E/mc^2$ the total radiated power goes with m^{-4} which is the main limitation for circular lepton colliders. From the ratio of masses between protons and electron, it follows that the energy loss via synchrotron radiation for electrons is $(m_p/m_e)^4 \approx 10^{13}$ times higher than for protons.

In the LHC, synchrotron radiation is generally produced within the bending magnets. Additionally two undulators (one per beam) are placed to be used by the BSRT. Undulators are special magnetic structures that create (additional) synchrotron radiation by wiggling the particle perpendicularly[23]. For the case of the BSRT at the LHC the undulator is necessary for the energy range below 1.2 TeV because the SR due to the dipole is outside of the detectable spectrum of wavelengths.

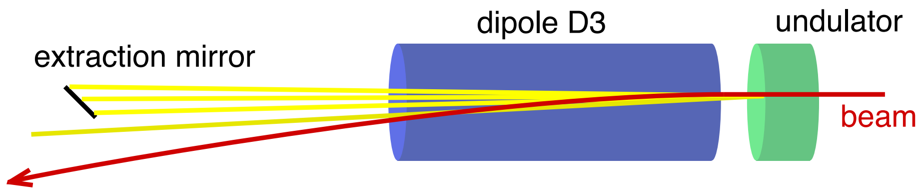

FIGURE 2.7: Sketch of the working principle of the BSRT.

The change in energy during acceleration shifts the emitted wavelength of the synchrotron radiation which changes the peak of the emission. Additionally, since the source of the SR changes from the undulator to the dipole also the focal point moves by 2.8 m. These changes need to be corrected for by adjusting the optical system to change the focal point and applying a correction factor for the change in the wavelength. The BSRT measures the photon beam size emitted at the location of the SR generation (e.g. the undulator or the dipole). Due to the optic parameters the measurements provided by the BSRT are not absolute and need to be cross-calibrated with the wire scanner for the corresponding energies (i.e. 450 GeV and 6.5 TeV). These calibrations also need to be repeated frequently to account for drifts by performing a special calibration run.

Due to its non-invasive nature the BSRT can run continuously and, coupled with readout electronics of sufficiently high speed, provide bunch by bunch measurements. It is currently the only instrument capable of providing these kinds of measurements [24].

2.4.3 Beam-Gas Ionization Monitor (BGI)

As the name suggests the BGI uses the ionization of gas molecules caused by the passing beam to measure the transverse profile. This ionization rate is proportional to the beam intensity. The electrons freed by the ionization are accelerated towards a positive electrode using a high electric field while at the same time being locked in a magnetic field that forces them on straight trajectories to limit the dispersion during transport (see figure 2.8 on the next page). The electrons are amplified using a Micro Channel Plate (MCP) and then directed on a phosphor screen where the electrons are converted to photons. The photons are guided out of the vacuum vessel using a prism and recorded using a CCD camera. To increase the ionization rate a gas injection system is installed which can be used to locally increase the pressure in the vacuum vessel.

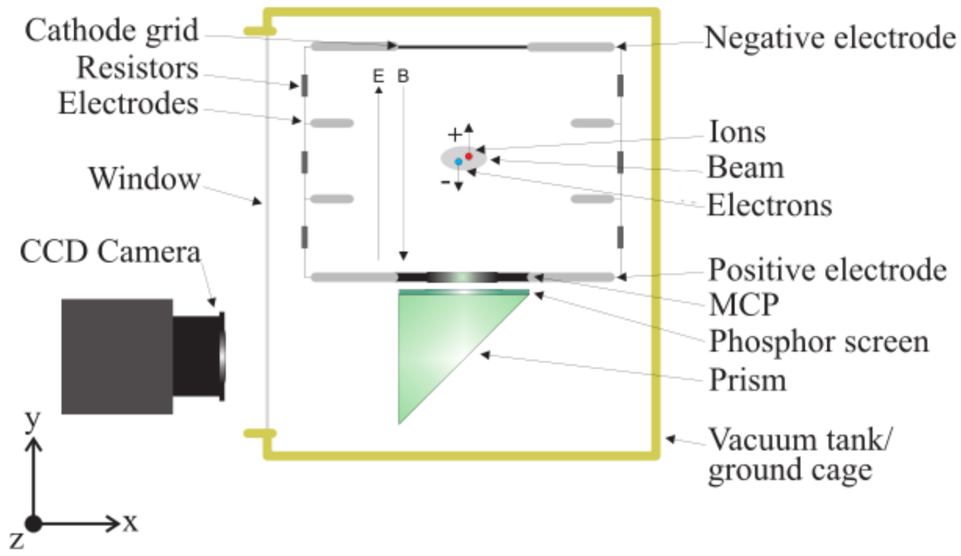

FIGURE 2.8: Schematic of the BGI as it was installed in the LHC.

Two basically identical BGI instruments were installed in the LHC, one for the vertical and one for the horizontal coordinate.

The operation of the BGI was plagued by multiple problems such as the uneven wear-out of the MCP requiring a correction for the decrease in gain, high voltage instabilities and calibration issues.

After some repairs and changes eventually it became apparent, that high impedance problems caused by the geometric design of the BGI lead to localized heating. The final decision was to remove it from the LHC and create a new design tackling all known issues from the beginning. As a consequence the BGI was not in operation at the same time as the BGV and therefore not available as a point of comparison.

Chapter 3

Beam Gas Vertex detector

3.1 Design goals

The goal of the BGV is to measure the beam size with enough precision to calculate the emittance with a precision of better than 5 %. The original goal was 5 % bunch by bunch size within 1 min as well as 2 % average bunch size resolution within the same timeframe [25].

The Beam Gas Vertex (BGV) demonstrator consists of three main components that work together to perform precise beam-size measurements. The final design consists of

A gas target chamber replacing a section of beam pipe combined with an injection system to allow for the variation of the gas pressure to choose the interaction rate.

A trigger system capable of selecting events originating from within the gas chamber and rejecting events originating from the other beam.

A high precision detector capable of detecting the tracks of particles exiting from inside of the target chamber combined with a read-out system capable of processing the data at sufficient speed.

3.2 Measurement principle

The measurement principle of the BGV relies on performing many measurements and then gaining information based on statistical analysis of the collection of measurements. The fundamental assumption is that the rate of beam-gas collisions is directly proportional to the local density and thus the distribution of protons in a bunch. Recording many beam-gas collisions allows for the statistical analysis of the distribution of locations of beam-gas interactions.

3.2.1 Distribution of independent measurements

The individual triggers registered by the trigger system (section 3.4 on page 25) are independent measurements. The localized frequency of the interactions directly represents the density of particles at a given location. To gain insight into the localized distribution, the tracks originating from the location need to be reconstructed as described in section 4.1 on page 35. When accumulating multiple measurements the distribution of these measurements represents the distribution of particles. The higher the number of events the lower the influence of outliers and therefore the higher the precision of the result. According to Poisson statistics the precision should follow $1/\sqrt{N}$ with N the number of events used.

3.2.2 Treatment of multiple collisions per triggered event

Following from equation (3.4) with the parameters $N = 1.1 \times 10^{11}$ protons/bunch, $\sigma_{phys} = \sigma^{inel}_{\mathrm{pNe}}$ and $\Theta = \frac{p}{k_B T} \cdot 2\,\mathrm{m}$ the probability for a beam-gas interaction is 0.0158 for the highest energy and gas pressure values possible. Consequentially the probability for two beam-gas interactions to happen at the same passing of a particle bunch is 2.496×10^{-4} (or $\approx 2.5\,\mathrm{Hz}$/bunch for the LHC revolution frequency). Double collision events therefore are only a small contribution to the overall number of events.

Since the BGV event selection criteria are optimized for single collision events most of these events are already filtered by the cluster filters of the HLT since they have approximately double the amount of clusters. In case they are not filtered by the cluster limits the beam size algorithm (see section 5.2 on page 51) is designed to differentiate between multiple vertices by using the z coordinate of the point of closest approach (POCA) of the tracks. Thus the precision is even improved in the cases of two or more collisions per event.

3.3 Gas target

The target for the BGV is a dedicated volume where the pressure inside of the vacuum of the LHC can be locally increased to in turn increase the beam-gas interaction rate.

3.3.1 Beam-gas interactions

The vacuum system of the beam pipes in the LHC achieves a very low pressure of the order of $10^{-9}\,\mathrm{Pa}$ ($10^{-11}\,\mathrm{mbar}$). This pressure corresponds to around 10^5 particles/cm^3. When a proton beam is circulating in the LHC it continuously interacts with these residual gas molecules in the beam pipe. This leads to a loss of protons in the bunches and therefore beam intensity. These beam-gas interactions are due to either the electromagnetic or the strong force acting on the particles with the kind of interaction provoking different results. If the interaction is electromagnetic the most likely scenario is coulomb scattering (an elastic interaction) which changes the trajectory of one or more protons in the bunch leading to them not following the ideal trajectory of the accelerator anymore. Their behaviour therefore becomes unpredictable and they are lost somewhere along the path of the accelerator. If on the other hand a strong interaction (which is inelastic) takes place the interaction creates a shower of secondary particles around the interaction vertex.

The probability for a beam-gas interaction to happen depends on the number of particles in the bunch N_{bunch}, the total density of the gas in the beam pipe Θ and the cross section σ_{phys} of the process. The total material density is the local density ρ integrated over the length of the relevant volume

$$\Theta = \int \rho(z)dz. \tag{3.1}$$

The local density can be calculated from the ideal gas equation

$$pV = Nk_B T \tag{3.2}$$

which transforms to

$$\frac{N}{V} = \rho = \frac{p}{k_B T}. \tag{3.3}$$

The total probability is therefore given by

$$\mu = \sigma_{\text{phys}} \cdot N_{\text{bunch}} \cdot \Theta. \tag{3.4}$$

The rate of interactions is therefore given by the repetition frequency f and the probability μ

$$R = f \cdot \mu = f \cdot \sigma_{\text{phys}} \cdot N_{\text{bunch}} \cdot \Theta. \tag{3.5}$$

The cross section σ_{phys} for the case of the LHC depends on the hadronic σ_{pp} which depends on the collision energy and has been measured extensively for proton-proton collisions [7]. The proton-nucleus interactions can be approximated with $\sigma_{pA} \approx \sigma_{pp} \cdot A^{0.71}$[26], where A is the mass number of the target gas. The unit of this cross-section is a surface area which in particle physics is commonly given in the unit *barn* with $1\,\text{b} = 1 \times 10^{-28}\,\text{m}^2$.

The total cross-section of the interactions is comprised of the elastic and inelastic components

$$\sigma_{pp}^{\text{tot}} = \sigma_{pp}^{\text{el}} + \sigma_{\text{pp}}^{\text{inel}}. \tag{3.6}$$

When calculating the influence of the BGV on the beam life time the total contribution σ_{pA}^{tot} needs to be considered whereas for the BGV event rate only $\sigma_{pA}^{\text{inel}}$ is relevant. This stems from the fact that elastic collisions have such a forward direction that they cannot hit the detector panels positioned outside of the beam pipe.

	σ_{pp}^{tot}	σ_{pp}^{el}	$\sigma_{\text{pp}}^{\text{inel}}$	$\sigma_{pNe}^{\text{tot}}$	$\sigma_{pNe}^{\text{inel}}$
498 GeV	40.11	6.75	33.36	336.50	279.87
4 TeV	43.00	8.20	34.80	360.75	291.95
10 TeV	48.00	9.00	39.00	402.70	327.19

TABLE 3.1: Particle cross-sections in *mb* taken from [7] or calculated using $\sigma_{pA} \approx \sigma_{pp} A^{0.71}$[26] with $A = 20$

3.3.2 Design of the target volume

The gas target system of the BGV was developed based on the following requirements:

- Fairly uniform longitudinal gas density over a length of at least 1 m,
- Uniform gas density over the transverse size of the beam (≈ 1 mm),
- Control of the gas pressure (i.e. beam–gas interaction rate), by tuning the gas flow,
- No impact on the LHC operation: negligible beam losses and no orbit instabilities,
- Low mass, high coverage exit window for the beam–gas interaction products (radiation length x/X_0 of about 1% or less, polar angle range 10 mrad to 100 mrad),
- Thin, reduced beam pipe diameter in the BGV detector region, to increase the coverage of high-energy, very forward particles.

A detailed description of the proposed BGV parameters can be found in [27].

Among the possible choices for a gas only inert gasses could be considered. Considering all noble gasses led to the following considerations. Helium was discarded as it is used for cooling of the Magnets and its usage would hinder leak detection. Neon and Argon have a mass in the useful range for collision purposes but Argon is also used for leak detection so its usage was discouraged as well. Up the periodic table we also have Krypton and Xenon which have a very high mass and therefore higher cross-section for beam-gas interactions. Due to their high particle multiplicity and higher saturation effects on the ion pumps they would increase the complexity of the clustering and additionally limit the lifetime of the vacuum setup and were thus discarded. The final choice therefore was Neon.

The gas injection system uses a controlled flow valve to increase the pressure in the target chamber up to 1×10^{-7} mbar. The distribution of the gas in the volume is very even with vacuum pumps in front of the volume and behind the detector making sure, that the pressure is only increased locally.

The gas volume itself consists of two parts. A 1873 mm long cylinder made out of 3 mm thick stainless steel (316N) and an aluminum structure made out of alloy AA2219. In beam direction the shape begins with a 5° tapering angle from the default beam pipe diameter (58 mm)and increases up to a diameter of 212 mm (fig: 3.1c). The shape then continues at that size up to the full length.

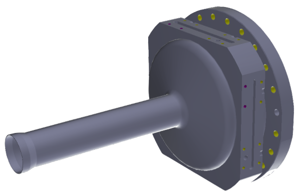

(A) Aluminium exit window and thinned beam-pipe.

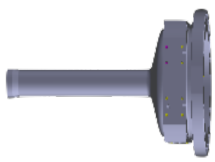

(B) Perpendicular view including attachment flange.

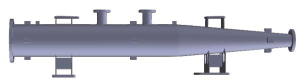

(C) Main chamber of the BGV with it's tapering shape to gradually increase the diameter and attachment flange on the left.

FIGURE 3.1: The two parts of the gas-target chamber of the BGV.

Attached to this cylinder is the aluminium structure (figure 3.1a and 3.1b) which reduces the diameter via a conical shape to 52 mm. This shape is the exit window designed to allow for the passing of the collision products out of the beam vacuum. During the transition from the outer diameter to the thinned beam pipe the window also linearly reduces its thickness from 3.2 mm to 0.9 mm. This is done over a distance along the beam pipe of about 28 mm[28] which can be seen in figure 3.1b. By changing the material to aluminium (alloy AA2219) and also reducing its thickness to 0.9 mm the radiation length (x/X_0) is lowered to about 1 % (Aluminium has a radiation length of $\approx$ 89 mm). AA2219 has a yield strength similar to that of steel but an approximately five times higher radiation length.

To calculate the rate of interactions in this about 2 m long volume we take equation (3.5) on the preceding page with $f = 11\,245$ Hz (LHC revolution frequency [14]), $N = 1.1 \times 10^{11}$ protons/bunch, $\sigma_{phys} = \sigma_{pNe}^{\text{inel}}$ and $\Theta = \frac{p}{k_B T} \cdot 2\,\text{m}$. By injecting neon into the gas volume the local pressure can be increased up to $p = 1 \times 10^{-7}$ mbar giving a theoretical interaction rate of 227 Hz (total) out of which 185.2 Hz are inelastic.

The influence of the locally increased pressure and therefore higher interaction rate on the beam half-life time due to the gas injection is in the order of years and can therefore be neglected (1.1×10^{11} protons per bunch with a collision rate of 227 Hz $\approx$ 10 Years).

3.4 Trigger system

A dedicated trigger system (Level 0: L0) is used to select beam-gas interactions that occured in the interaction region. This section describes the components and their layout and logic.

3.4.1 Trigger hardware setup

The trigger signals are generated by four scintillator panels positioned at three different positions along the beam pipe. Scintillator panels consist of scintillating fibres in which light is emitted when a charged particle passes through them. Due to the coating of the fibres the light is mostly reflected internally and guided along the fibre to a photo multiplier where the signal is amplified. Two panels are positioned in-front of the gas volume (VETO), one right after the SciFi detector (SIGNAL) and one three meters downstream after that (CONFIRM) (see fig 3.2).

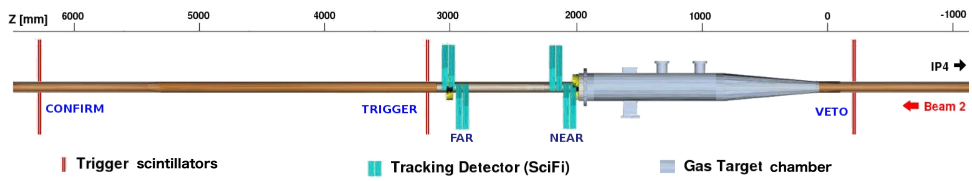

FIGURE 3.2: Drawing of the three main components of the BGV to scale with the positions of the trigger panels along the beam pipe.

The scintillator panels are 30 cm × 30 cm squares with a thickness of 1 cm with the fibres connected to a 60 mm diameter photomultiplier tube assembly (Hamamatsu type H1949-51). The signals are transported via coaxial cables over a distance of 60 m to the service tunnel where the electronics crate is housed. To align the signals roughly in time the signals from the VETO and SIGNAL planes are delayed by ≈20 ns and ≈10 ns respectively by adding the appropriate length of cable to their connections. The remaining spread in the arrival times is caused by the different lengths in the scintillating planes that the generated light needs to travel before it hits the PMT. The PMT itself has a rise-time of about 1.5 ns.

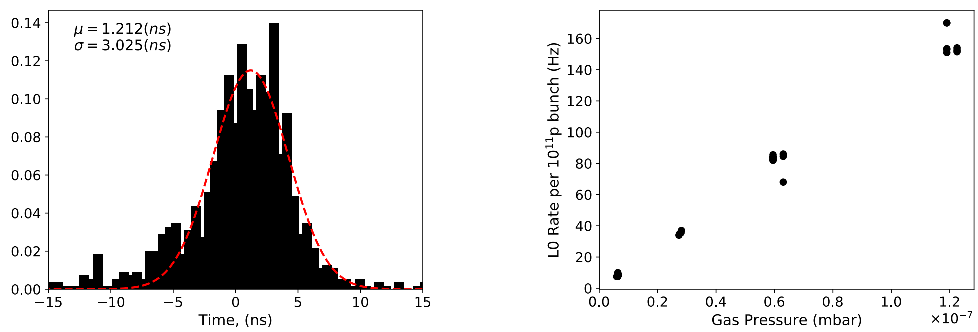

(A) Difference in time between the SIGNAL and CONFIRM planes of the BGV after correcting for the time of flight using cables of appropriate length.

(B) Linear increase of the trigger rate with the change of the gas pressure when injecting gas.

FIGURE 3.3: Plots showing the timing behaviour of the L0 trigger as well as the scaling of the trigger rate with the gas pressure.

The analog signals are then passed through a constant fraction discriminator (CFD, CAEN V812) for digitization. The digitized signals are then passed to a programmable logic unit (CAEN V2495) where they are aligned in time with about 1 ns of precision figure 3.3a on the previous page.

3.4.2 Event selection

A decision algorithm in the logic unit allows for the definition of a trigger mask based on the four input signals. By default a L0 trigger signal is emitted when the SIGNAL and CONFIRM planes have measured a signal and the VETO planes did not. The rejection of VETO signals prevents the acceptance of beam-gas collisions that happened in front of the interaction volume. The coincidence of SIGNAL and CONFIRM inhibits triggers from random noise sources in the panels as well as particles originating from beam 1 of the LHC.

3.5 High precision detector

The precision tracking detector of the BGV consists of scintillating fiber panels positioned outside of the beam pipe in two stations separated by almost 1 m of air (see figure 3.2 on the preceding page). The analog signal pulses of the fibers are read out, amplified and transported to the service tunnel for digitization.

3.5.1 Scintillating fibre panels

Scintillation is the name for the effect of the emission of photons when an energy deposition occurs from a particle by ionization. The amount of light produced behaves almost linearly with the energy deposited by the particle. The detecting planes of the BGV are constructed out of round, double-cladded scintillating fibres (SciFi) with a diameter of 250 µm. The panels were assembled at EPFL as part of the effort for the production of the ones for the LHCb experiment and are mostly equivalent. I will be giving a fair description of the panels for an extensive description of their construction procedure please refer to [29].

The fibres are taken from the roll provided by the manufacturer and transferred on a target roll with a circumfence of 3 m with the goal of creating an even structure. All the fibres are then glued together using a epoxy glue with added TiO_2 powder to reduce cross-talk between the individual fibres. For the BGV either four or five of these layers are rolled on top of each other to increase the light yield and cast together using a casting glue. These slightly pyramidic shapes are then cut into slices of 256 fibres next to each other forming an active area of 65 mm width with 320 mm height. Two SiPM arrays of type H2014 [30] with 128 channels each are mounted together and then fixed to one side of the mat to cover the 256 fibres. The other side of the mat is covered with a mirror to increase the light-yield. Between the two SiPMs is a small dead area of the width of about one fibre which needs to be accounted for in the reconstruction.

Four of these sets of 256 channels are put next to each other to form a BGV SciFi layer. A 97 mm $\times$ 97 mm cut-out at one corner of the mirror-side of the SciFi layer allows positioning close to the beam-pipe and thus a better azimuthal acceptance. Fixing two of these layers together with an angle difference of 2 degrees creates a module. This second layer is refered to as *prime* layer and is used to facilitate pattern recognition [31].

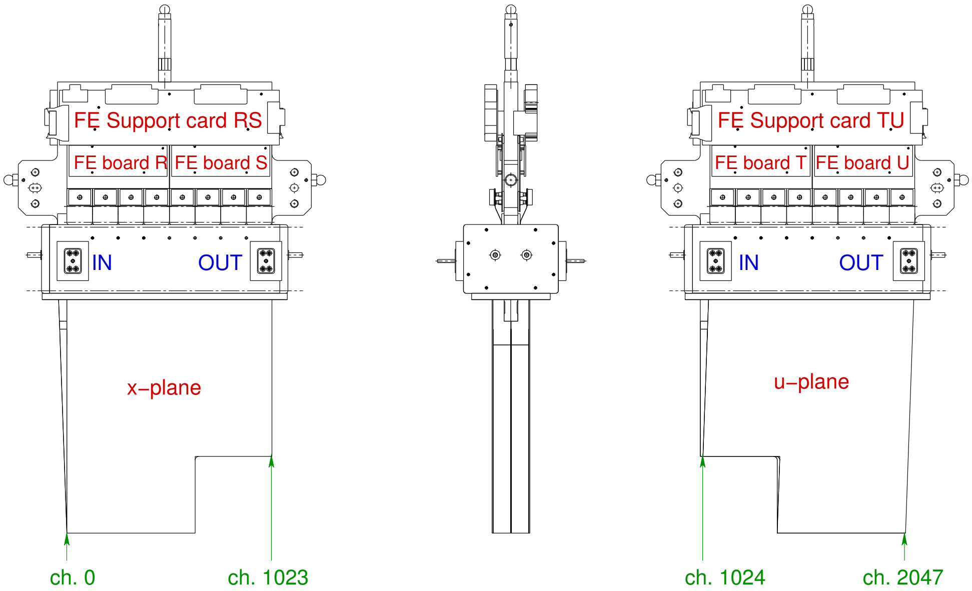

FIGURE 3.4: Drawing of one BGV module

3.5.2 Geometric layout

The BGV is constructed by placing eight of the modules described in the previous subsection in precise locations around the beampipe. Two modules are put together with 90° of rotation with respect to each other to form a detecting station capable of delivering four coordinates (X, X', Y and Y', see fig: 3.5a).

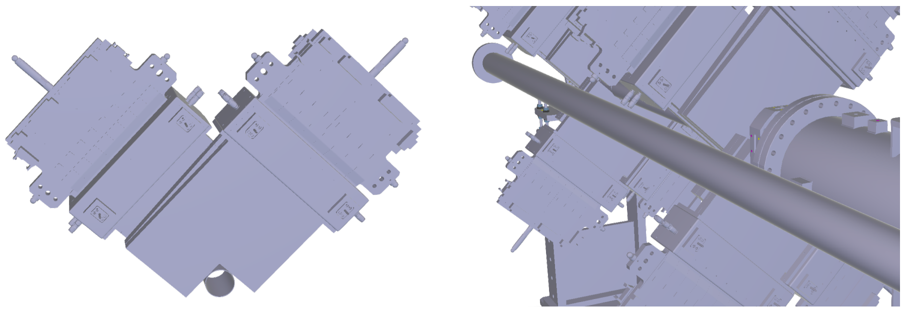

(A) Two modules are put together to provide a four coordinate measurement.

(B) The presence of the beam1 pipe necessitates the placement of the modules in that way.

FIGURE 3.5: CAD drawings of the BGV modules showing their placement with respect to each other and to the beam pipes.

One of each of these detecting stations, with modules containing four layers of fibres, are placed on above and below the beampipe as close as possible to the exit window of the gas target chamber. One metre downstream an equivalent setup is placed with the main difference, that the modules contain five layers of fibres to increase light-yield.

The modules are placed 45° rotated with respect to the horizontal plane to maximise coverage while having to leave space for the beam 1 pipe (see fig: 3.5b).

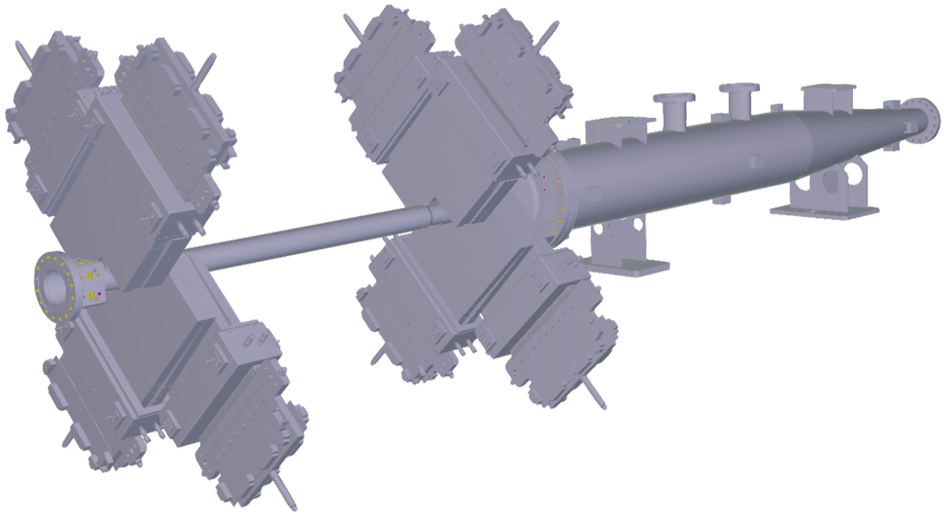

FIGURE 3.6: Placement of all modules around the beam pipe.

3.5.3 Cooling

The BGV sensors and front-end electronics are exposed to background radiation generated by beam losses and beam-gas interactions. Radiation damage leads to an increase in the optical attenuation of the scintillating fibres, but the effect on the detector performance is insignificant due to the small size of the modules. This does however not hold true for the neutron fluence which increases the SiPM dark count rate [29]. This necessitates cooling of the SiPMs in order to maintain an acceptable noise cluster rate [32, 33].

The expected radiation fluence and dose can be estimated from the predicted rate of beam-gas interactions, giving a yearly charged-particle fluence of $4 \times 10^{10}\,\mathrm{cm}^{-2}$ in the region of the BGV tracker. This is the integrated fluence at radii between 22 cm and 26 cm around the LHC beam pipe, where the BGV SiPMs are located. Since most charged particles are highly energetic (more than 1 GeV), this fluence can be translated into about $2 \times 10^{10}\, n_{\mathrm{eq}}\,\mathrm{cm}^{-2}$ (where n_{eq} stands for '1 MeV neutron equivalent') and to a dose of the order of 1 Gy/Year.

A single-phase cooling system is installed to cool down the SiPMs. A brief overview of the system is given here, while a more detailed description can be found in [32, 33]. The cooling system is composed of a commercial refrigerator unit located in the service tunnel and cooled by ambient air. This is operated in a closed loop with C_6F_{14} fed into a pair of 25 m long transfer lines before reaching the main manifold located inside the LHC tunnel. The manifold provides 4 parallel output loops for detector cooling, each individually tunable by a manual needle valve. C_6F_{14} is chosen both for its thermal properties and radiation resistance. The power dissipation per module has been measured to be approximately 20 W (dominated by heat leaks).

A typical flow of $20\,\mathrm{l\,min}^{-1}$ with a supply temperature of $-15\,°\mathrm{C}$ at the refrigerator is used to achieve a detector temperature of approximately $-10\,°\mathrm{C}$. The refrigerator's control system keeps the cooling fluid temperature stable within less than 0.1 °C. Temperature variations between different SiPMs are also measured to be less than 0.1 °C. The SiPM cold-boxes as well as the main manifold are flushed with dry air in order to prevent water vapour condensation.

3.5.4 Analog readout chain

The 128 analog signals emitted by each SiPM are read-out using the radiation tolerant Beetle front-end chip which was developed for LHCb [34]. Each of the 128 channels is sampled synchronously with the 40 MHz LHC bunch clock and stored in an intermediate storage pipline to allow for some time for the trigger signal to reach the beetle chip. Since the Beetle chip was designed for usage with silicon sensors, which have a relatively small input signal (about 10^4 electrons per MIP) the signals originating from the scintillating fibres (about 10^7 electrons per MIP) need to be attenuated to fit into the dynamic range of the Beetle chip. This is achieved by using an RC-circuit that provides an attenuation of about 300x [31].

Upon receival of a trigger signal the corresponding storage cell position is marked for readout and an internal multiplexer transfers the signals via four ports time-multiplexed with the LHC frequency (40 MHz) to the repeater boards. This time-multiplexing limits the maximum data transmission rate to 40 MHz/32 = 1.25 MHz without accounting for overhead. Since the beam-gas interaction rate maxes out at 227 Hz/Bunch (see section 3.3.1) the total L0 trigger rate for up to 2808 bunches is 637 kHz and thus well below this limit. The transfer rate therefore does not limit the overall read-out speed of the setup.

The repeater boards, which are placed a few metres of cable length away from the detector, buffer the signal, amplify it and then send it via 60 m of cables to the read-out Board (TELL1, originally developed for LHCb[35]) which is located in the LHC service tunnel, outside of the radiation environment. In total there are eight TELL1 boards, each handling the signals from one SciFi module.

The management of the readout is done by the ODIN read-out supervisor board which was also developed for LHCb and has been configured with a firmware that is optimized for BGV operations. ODIN handles the input signal coming from the L0 trigger, matches them to the LHC bunch number and checks if the TELL1 boards are all in a 'ready' state by means of the capacity monitoring board HUGIN. If there is capacity available ODIN distributes internal trigger signals to the TELL1 boards prompting them to read-out the Beetle chips.

The supply of low voltages for the repeater boards and the beetle chips as well as the high voltage which is used to bias the SiPMs is provided by CAEN voltage supply boards (four A2518, one A1539 and one A1535D) placed in a crate in the service tunnel.

3.6 Data processing and analysis

This section describes how the analog data is received by the TELL1 board, digitized and several raw data corrections are applied. Furthermore the clustering algorithm and how the data is transmitted via the gigabit ethernet connection to the HLT computing farm is explained. Finally the different functions the HLT can perform are described and the data processing procedure is given.

3.6.1 Data correction, digitisation and clustering

The analog signals received by the TELL1 board are digitized using a 10bit ADC. [36] These raw values are then corrected using a chain of corrections which are applied in the reverse order of the introduction of the distortions due to the read-out chain.

Raw data corrections The raw data is corrected by applying the following steps in the given order. A short overview of each step will be given here, for a complete explanation please refer to [37].

1. *Pedestal subtraction* The value corresponding to "no signal" in the ADC is non-zero. To subtract it from the measured value a calibration measurement is performed without any signals. The average value per channel over all calibration events is the pedestal which is subtracted from the raw values during standard runs.

2. *Header correction* Four pseudo-digital bits precede the 32 analog values for each analogue link which contain header information. The values of these bits influence the first data values transmitted. For this correction it is assumed that only the last two header bits influence the first two data channels. Depending on the four possible combinations of the header bits the deviation is measured during calibration and then applied during standard runs.

3. *Common mode noise suppression* Noise introduced in the analog link varies from event to event and can therefore not be calibrated against. To remove this noise the average of all values in one analog link is calculated for each event and then subtracted. Since channels can (and should) have hits only values close to the zero-value are considered in the average.

4. *Channel correlation correction* Two phenomena have been identified to create a correlation between channels due to cross-talk between signals. The first is cross-talk between the two channels transmitted consecutively in the analog link (offset of five channels). The second is due to the lines on the front-end board.

   For a given channel i the signal amplitude A(i) is corrected by subtracting a fraction $x_{j\to i}$ of the signal amplitude of a neighbouring channel j. Measurements have shown that the most significant correlations (more than 10 %) comes from channels $i+3$ and $i+5$ and therefore only these are corrected for:

$$A_{\text{corrected}}(\text{i}) = A_{\text{raw}}(\text{i}) - x_{\text{i+3}\to\text{i}} \cdot A_{\text{raw}}(\text{i+3}) - x_{\text{i+5}\to\text{i}} \cdot A_{\text{raw}}(\text{i+5}). \qquad (3.7)$$

The correction algorithms are calibrated in the laboratory, tested on raw data and implemented in the TELL1 boards.

Clustering Once all raw data corrections are applied a cluster-finding algorithm is run that combines neighbouring channels into clusters if they fulfill certain criteria [38, 39]. The algorithm consists of four steps and is also illustrated in figure 3.7b on the next page:

1. Identify channels with signal amplitude above a *seed threshold* (seed channels),

2. Identify channels with signal amplitude above a *neighbour threshold* (neighbour channels),

3. Form clusters from adjacent seed channels and, at most, one neighbour channel on the left and one on the right (total size limited to four channels).

4. Discard clusters with total signal amplitude below a given *sum threshold.*

The clustering thresholds are defined per SiPM and have been fine-tuned with the results presented in [31]. They are optimized towards detection efficiency while limiting the average number of noise clusters to below 1.5 noise clusters per module per event.

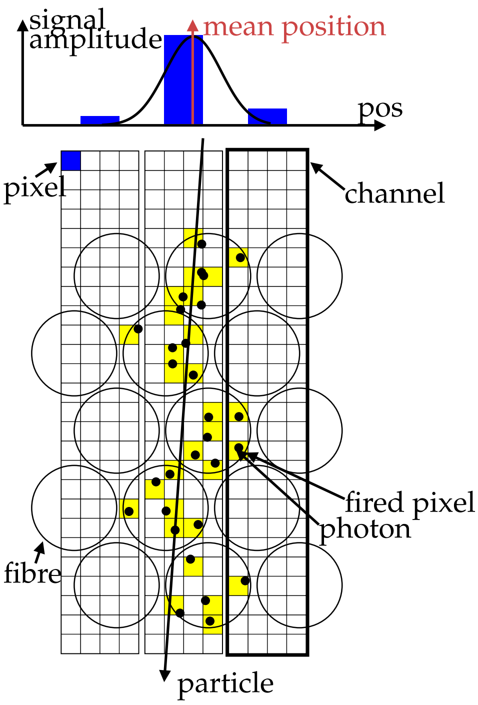

(A) Signal generation due to a charged particle passing through a five-layer SciFi panel as seen from the perspective of the SiPM. The particle is detected by multiple fibres producing a signal in multiple pixels of the SiPM. Only the sum of signals for the 104 pixels of one SiPM channel is read out.

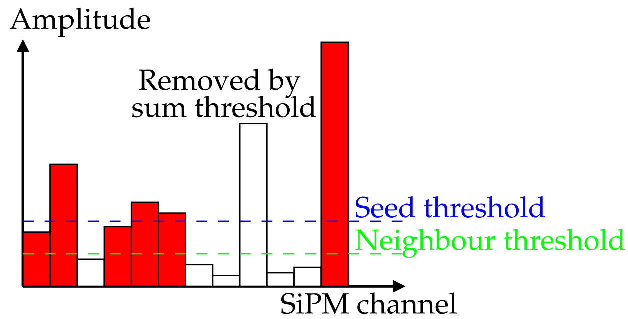

(B) Clusters are recognized when a channel has a signal of more than the *seed threshold* and accepted if the *sum threshold* is met.

FIGURE 3.7: Illustrating the cluster creation and recognition in the SciFi panels.

The information of the cluster is stored into 14 bits, 11 bits to identify the reference channel and the remaining three to store the relative offset (inter-strip-position) in units of 1/8th of a strip width (corresponding to 31 µm).

The data of each TELL1 is packaged together and sent to one of the analysis threads running on the HLT nodes via gigabit ethernet. The package contains either only the (corrected) ADC values (non-zero suppressed [nzs]), the cluster information as calculated by the clustering algorithm (zero suppressed [zs]) or both.

For non-zero suppressed data the event-transfer-rate via gigabit ethernet maxes out around 3.3 kHz. The theoretical maximum equals to 4078 Hz but does not account for protocol overhead. For zero suppressed data the theoretical limit is at around 47 kHz. The practical limit is currently unknown since the bottleneck has shifted to the available cpu capacity of the computing farm.

3.6.2 Online and offline data processing

The data processing and analysis system of the BGV is based on the LHCb analysis framework(GAUDI), specifically on the *Boole*(v29r7) package [40]. Many modules such as the raw decoder, the cluster maker and the SciFiEvent were copied from

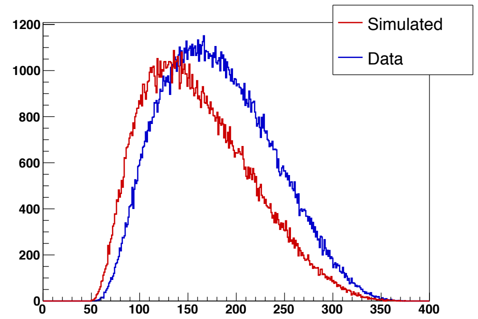

(A) Cluster multiplicity for simulated and recorded data

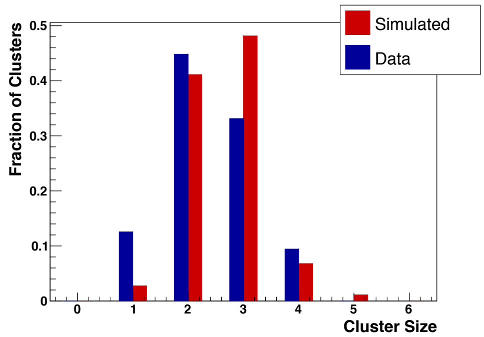

(B) Cluster size distribution for simulated and recorded data

FIGURE 3.8: Comparing fundamental cluster plots between simulated and recorded data. It is important to note that for recorded data, presumably due to effects caused by beam 1, the cluster multiplicity is slightly elevated in comparison to simulation.

LHCb and used for the BGV with only minor adaptations. Additional modules for BGV-specific cases were developed over the course of the project to facilitate pattern recognition, event filtering and monitoring.

The main design idea of the GAUDI software architecture is based on Algorithms which commonly manipulate data objects and store data objects of either the same type or a different one. Algorithms are registered in the required order with the *application manager* which instantiates the correct version and executes the algorithm at the appropriate point in time. Multiple algorithms can be combined into a sequence which can be added or removed from the main sequence of the application manager as one entity. The storage of data is handled transparently using the so-called Transient Event Storage(TES) system which works on an event-by-event basis keeping the relevant data available. Commonly an algorithm accesses one or multiple TES branches, performs the relevant action such as filtering, tagging or more advanced calculations and then stores the result back into a new TES branch. The relevant data is processed on an event by event basis with the TES containing only the values for one Event at a time. A persistency service is in charge of storing selected data in a persistent form once an event has been analyzed. These persistent forms can take multiple forms, for the BGV only LHCb raw data files (mdf) as well as ROOT [41] files were used.

The differentiation between *offline* and *online* analysis originates from the source of the data.

Online refers to the data originating directly from the TELL1s and the algorithms being run directly on the processing infrastructure.

Offline signifies, that the source of the data is some form of persistence storage, usually a mdf file on a disk. This allows for detailed studies of the whole analysis process by analyzing the same data in different ways and comparing the results.

Depending on the type of data stored (zs, nzs or both) different analysis are possible. If the input is nzs data then different noise-cuts and thresholds for the clustering algorithm can be applied to optimize these low-level parameters. Due to the lower data rate as well as the higher processing time (since the filtering and clustering are now done in software) this data is only moderately useful for actual beam-size measurements.

Zero suppressed data can be processed significantly faster and allows for rapid and dynamic parameter optimization due to the reduced processing time and higher amounts of data per second. All results presented in chapter 6 on page 63 are from the analysis of zs data.

3.6.3 Online event selection (HLT)

The HLT used for the BGV consists of six computing blades (type HPE ProLiant BL460c). One of the blades is a dedicated control board (BGVCTRL) managing the remaining five and orchestrating the data transfers between the nodes. The persistency service is executed on the BGVCTRL thus all output files are stored on the RAID1 system of this blade only. The remaining five boards provide a total of 92 cores for the BGV analysis. Once a run is started, the control interface initializes 10 analysis threads per blade which are then offered to the ODIN control board as available capacity. Whenever a package is received by a thread the available capacity is reduced by one. Once a thread has completed the requested analysis and transmitted the results to the BGVCTRL board the available capacity is incremented by one to signal the availability of the thread.

Once a package is received by a thread it decodes the content and performs a selectable sequence of filters and algorithms. The following filters and algorithms have been developed for the BGV

Filters

Total cluster count This very fast filter ensures that the event contains a minimum amount of clusters to even be able to fulfill the next conditions while also limiting the maximum amount of clusters in the event. Events with a very high amount of clusters take disproportionally longer to reconstruct in comparison to their contribution to the result.

Module cluster count Each module needs to have at least two clusters to be able to reconstruct two tracks which is the basic requirement for any kind of BGV measurement. Additionally an upper bound is implemented per module to remove events where one module shows an uncharacteristically large occupancy.

Total track count For an event to be accepted for beam size calculations at least two tracks need to have been found.

Algorithms

Pattern recognition Executes the pattern recognition as described in section 4.1 and stores the tracks in the TES.

Event storage Stores selected data banks from the TES to an mdf raw data file on disk for offline processing.

Publisher Calculates the correlation values as described in section 5.2 and transmits the results to the control machine. The control machine collects the results until a defined amount of time or data is reached, performs the fits and publishes the results to the technical network.

Depending on the current mode of operation of the BGV a certain subset of algorithms and filters is active.

	Protons	Lead-Ions
Total cluster count	$50 \leq 400$	$40 \leq 640$
Module cluster count	$2 \leq 50$	$5 \leq 150$
Total track count	$2 \leq$	$2 \leq$

TABLE 3.2: Selection parameters used for the BGV during the 2017 and 2018 runs.

Passthrough The HLT does not perform any actions except collecting the events from all TELL1 and storing the raw data to disk. This raw data is defined by the TELL1 configuration and can either be ADC data, clusters or both.

Combined mode The HLT applies the *Total cluster count* and *Module cluster count* filters and stores the events that passed the filter to disk. The TELL1 are commonly configured to only transmit the cluster information.

Operational mode The HLT receives clusters only data and applies the filters and algorithms in the order: Total cluster count, Module cluster count, Pattern recognition, Total track count, Publisher with the aim of providing the best result in the shortest amount of time.

Operational debug mode Performs exactly the same steps as the operational mode but additionally calls the *Event storage* algorithm at the end.

The parameters for the filters applied in the HLT were chosen after an extensive study of multiple data-samples and beam-types. They are given in table 3.2 and differ for proton and lead-ion beams to accommodate the different behaviour of the particle showers. These differences are discussed in detail in section 6.2.4 on page 68.

3.6.4 Filter efficiency/passing rate

Multiple steps of filtering are performed and additionally the available capacity leads to throttling of the read-out rate in case of no availability of any component in the chain. The individual steps and their absolute and relative filtering steps are given in table 3.3.

Filter	Rate [kHz]	pass per step	global pass
Theoretical rate	580.0	100.0 %	100.0 %
L0 trigger rate	458.0	79.0 %	79.0 %
HLT availability	22.4	4.9 %	3.9 %
Global cluster cut	17.4	77.7 %	3.0 %
Module cluster cut	11.6	66.7 %	2.0 %
Total track count	4.8	41.4 %	0.8 %

TABLE 3.3: Gives the absolute numbers and percentages of the individual steps and their cuts

The biggest reduction in rate is happening at the level of the availability of the HLT. This is due to insufficient computing capacity. To mitigate this problem additional CPU blades were installed in June 2019 but the increased rate could not be tested before the conclusion of this thesis and would not be relevant for the results presented here either.

Chapter 4

BGV track and vertex reconstruction

During the hardware development period an extensive simulation was developed as well which encompasses all of the components of the BGV. This full simulation was used to develop the pattern recognition algorithm and the corresponding monitoring algorithms. Additionally the simulated data was used to qualify the algorithm.

4.1 Pattern recognition

The clusters created in section 3.6.1 on page 30 ideally represent all particles that have passed through the SciFi layers of the BGV. To find combinations of clusters created by the same particle, which in turn was created by a beam-gas collision in the gas volume, a pattern recognition algorithm needs to be used. There were two pattern recognition algorithms developed for the BGV, *BGVPattern* and *PatRecB*.

4.1.1 Combinatorical approach (BGVPattern)

BGVPattern follows a combinatoric approach by creating all possible cluster combinations between relevant planes with very few selections applied. It is described in detail in [32] by the developer.

The detection efficiency of this algorithm is around 70 % but the computation time scales rather poorly with the number of clusters. The originally expected average computing time was (15 ± 5) ms. Running the algorithm on a more recent computer (i7-3770 CPU @ 3.40GHz) gave an average runtime of about 10 ms/event. This still only equates to 100 events per second which was forseen some time ago and lead to the development of a second, faster algorithm (*PatRecB*) by Plamen Hopchev. It follows a different approach and amongst other things employs knowledge of detailed detector properties to optimize the execution time. A detailed description of the algorithm and the adaptations that had to be made to optimize the algorithm for detector data is given in the next section.

4.1.2 Geometrical approach (PatRecB)

This is the pattern recognition algorithm currently in use by the BGV and used for all results presented in this thesis. It was originally developed by Plamen Hopchev and was originally soley based on the full simulation of the BGV geometry and the clusters generated by the event generator. It is designed to take advantage of the specific layout of the BGV to decrease computation time and reduce the amount of fake tracks recorded.

Since the BGV is symmetric when rotated by 180 degrees around the z-axis (except of a small shift along the beam pipe) the pattern recognition algorithm can be applied to the two halves separately with small parameter modifications for the TOP and BOTTOM halves. Hence, to optimize the computation complexity the first operation of the algorithm is to split the list of clusters into two blocks, one for the top half and one for the bottom half of the detector. Within each of these halves the clusters are split into the eight consecutive layers making up each half. To optimize the speed and memory requirements of the algorithm the clusters are converted to so-called Geometric Identities (GeoIDs). These are integer numbers representing the position of a cluster on a layer while considering the additional distance created by the gap between the SiPMs as well as dead areas (see sec. 3.5.1). They can generally be considered like the consecutive channel numbers but are spaced almost perfectly uniform.

Search windows

Search windows are used to reduce the number of clusters considered for a track candidate. They are calculated by applying basic trigonometric functions to the GeoIDs selected at a given stage with the aim of limiting the amount of GeoIDs that need to be checked. They provide a rough estimate of the range a matching GeoID could be located in and reduce the search range from 1035 GeoIDs per layer to between 300 and 10 (depending on the number of GeoIDs already selected). The exact parametrization of the search windows was at first done using the MC simulation and once data was available additional small adaptations were performed to optimize for acceptance vs runtime.

To mininize the amount of combinations that need to be checked, search windows are calculated for each layer during pattern recognition. They are designed to use the geometry of the BGV to aid pattern recognition. When a search window is calculated all GeoIDs matching it are sequentially chosen and the following window is checked with the new GeoID selected as an option (see also section 4.1.2 on the next page).

Window 0 uses the position of the GeoID in the FAR station to estimate a range in the NEAR station where hits of tracks originating from the gas volume can be found. Depending on the current GeoID under investigation this can lead to a window size of between 30 and 300 (see figure 4.2a on page 38).

WindowPV uses the slope between the GeoIDs of the first layer in the NEAR and FAR plane to estimate the z-coordinate z_{PV} of the primary vertex

$$z_{PV} = \frac{i_{far} * z_{far} - i_{near} * z_{near}}{i_{far} - i_{near}} \tag{4.1}$$

with i_{near} and i_{far} the GeoIDs in the near and far plane respectively. The precision of this estimation depends significantly on the difference in GeoIDs (see figure 4.2b on page 38) and breaks down completely when they have the same value as the denominator becomes zero. Geometrically these GeoIDs represent tracks that are parallel to the z-axis. To allow for recognition of these tracks a higher margin is used for GeoIDs with an absolute difference of less than 12. The window is passed if the estimated z_{PV} is within the range of the gas volume plus margin.

Window 1 uses the slope created by the two selected GeoIDs in the NEAR and FAR layers to define a range for the prime layer which is rotated by 2° with respect to the already chosen layers. As is clearly visible in figure 4.2c on the following page the cutout window allows for the reduction of the window size for a part of the range. The maximum range is defined by the maximal difference between the GeoIDs of the normal and prime layer given by the rotation angle and the strip length ($340\,\text{mm} \cdot \sin(2°) \approx 12\,\text{mm} = 48\,\text{GeoIDs}$), see figure 4.1a.

Window 2 uses the three selected GeoIDs to estimate a range on the perpendicular 3rd layer of a station. This window is responsible to perform the switch from one coordinate to the next and uses the available information from the overlap of the GeoIDs in layers 0 and 1 to define the center of the search range for the layer 2 GeoID (see figure 4.1b). Due to the low angle the overlap region is rather large encompassing 120 GeoIDs figure 4.3a on page 39.

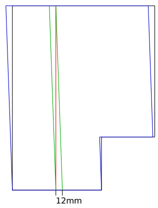

(A) starting from a hit in layer 0 (red) it is clear that the search window in layer 1 (dark blue) has to be in the range of strips equivalent to the 12 mm of offset.

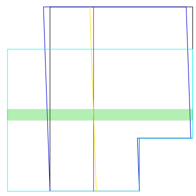

(B) After selecting a GeoID in that range (yellow) the search window on the perpendicular layer 2 (cyan) has to be in the green range

FIGURE 4.1: Graphical representations of search windows 1 and 2.

Window 3 uses the four selected GeoIDs to estimate a range on the last missing layer of the station. This search window is very narrow as can be seen in figure 4.3b on page 39.

The application of the Windows 1, 2 and 3 is collectively known as the completion of the two module assembly (2MA) since it performs the completion of one station. After creating a list of 2MA combinations for the NEAR station a loop calculates all possible 2MAs in the FAR station for each 2MA in the NEAR station and performs a fast fit on the selected eight GeoIDs (after converting them back to clusters). The best combination is added as a track candidate under consideration.

Once GeoIDs in the FAR station have been tried the algorithm finishes and a precise fit is performed of all track candidates to get the final track parameters. If the fit fails or the χ^2 value is greater than 100 the track is discarded.

Since the algorithm was developed against simulated data certain aspects of real data could not be forseen or considered and thus the algorithm needed to be adapted. The most prominent of these changes was the alignment of the fibre mats glued to each other, the change of some search window sizes to better match the actual alignment of the detector as well as the introduction of correct multiple scattering and cluster size based errors into the fit.

Algorithm

The main pattern recognition procedure (see figure 4.4 on page 39) consists of the following steps.

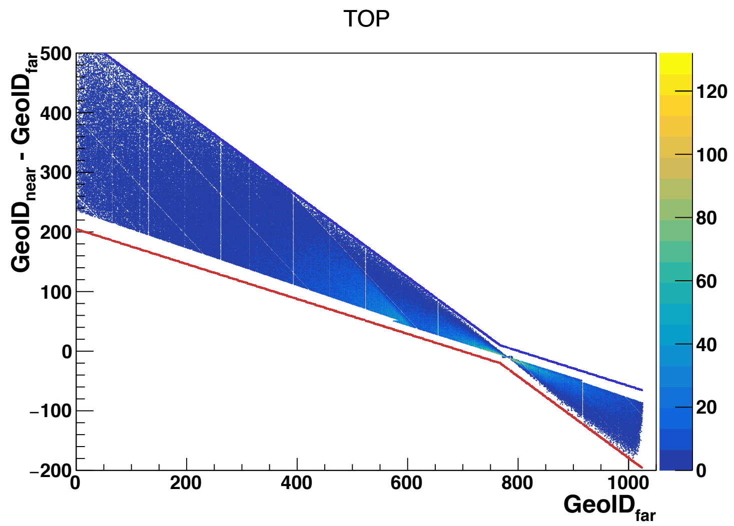

(A) Window 0 limits calculated from the GeoID in the far station. The lower limit is given by the red marking, blue denotes the upper limit.

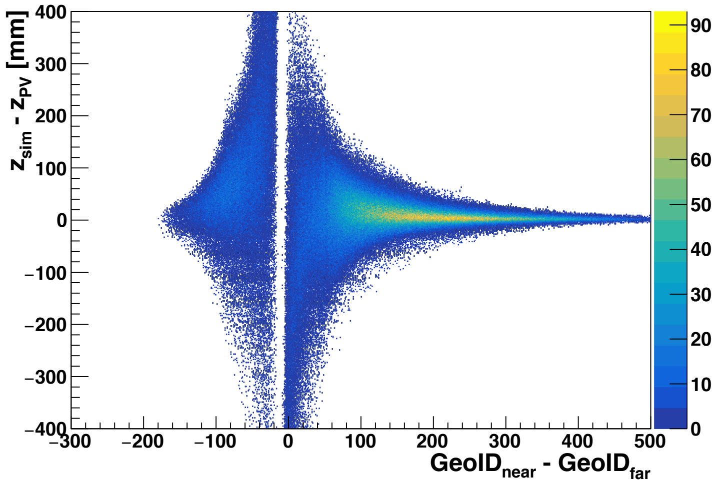

(B) Accuracy of the quick estimation of z_{PV} in comparison to the actual location as given by the simulation.

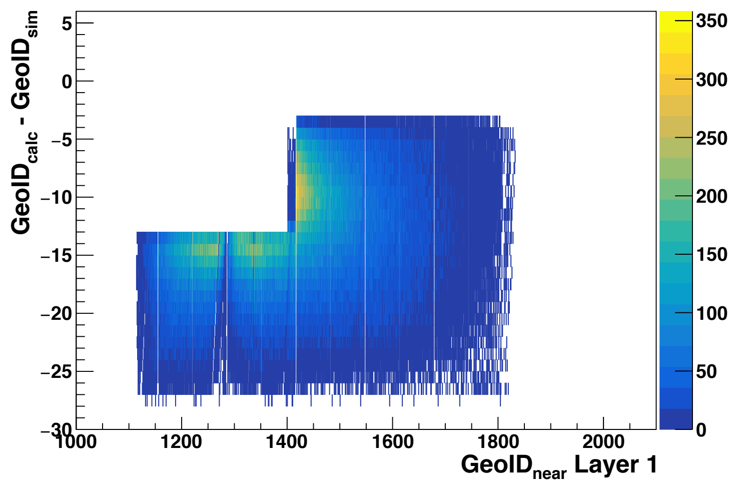

(C) Window 1 - difference between expected and actual value in Layer1 as a function of the position in Layer 1.

FIGURE 4.2: The ranges of GeoIDs that are possible for windows of the NEAR station.

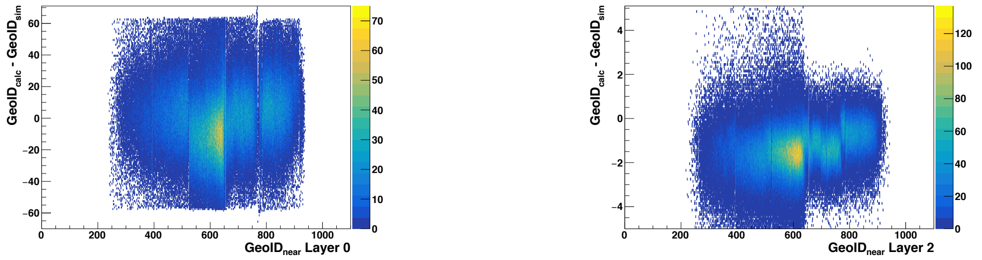

(A) Window 2 possible values with respect to the actual value in layer 0.

(B) Window 3 possible values with respect to the actual value in layer 2.

FIGURE 4.3: The windows for the perpendicular planes of the NEAR station.

- Select one GeoID in the first layer of the FAR station
- Select one GeoID in the first layer of the NEAR station
- Check if the difference between the GeoIDs is accepted in *Window 0*
- Check if the combination passes *Window PV*
- Find possible combinations of four GeoIDs by iteratively adding one per layer in the NEAR station
- Iterate over these combinations and for each iteration find possible combinations of 4 GeoIDs in the FAR station using the same algorithm as in the previous step.
- Perform a fast fit and accept only one combination per near station quad.
- Perform a four parameter fit of the accepted combinations and store those which are below a χ^2 cutoff as accepted tracks.

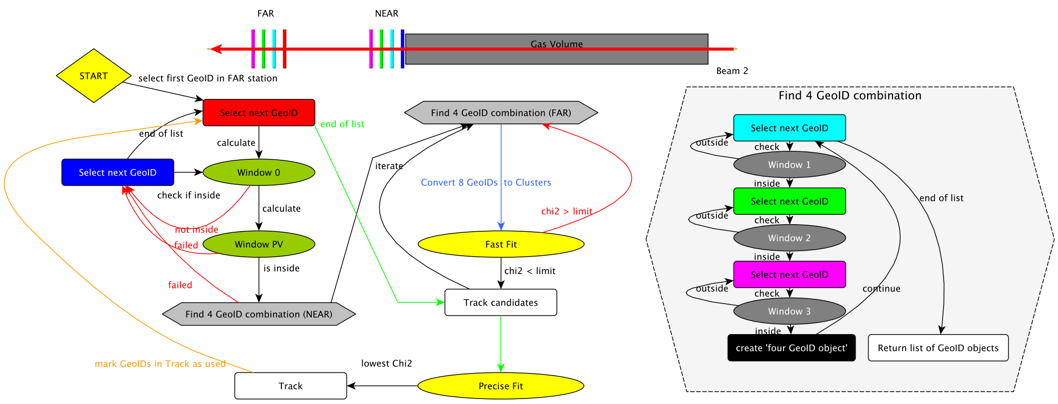

FIGURE 4.4: Flowchart showing the order of operation of the PatRecB algorithm. The representation of the BGV on the top is colour coded to show which layers the windows correspond to.

4.1.3 Algorithm qualification

Using simulated data a thorough check of the pattern recognition algorithm was performed and its behaviour qualified.

Monte Carlo simulation

An extensive simulation of the BGV was developed based on the LHCb software package GAUSS which uses GEANT4 [42] to simulate the particle-material interactions. The proton-Neon interactions were produced by the HIJING [43] generator. The full detector geometry as well as the gas target chamber were designed using the LHCb geometry framework.

At first a collision between a proton and a Neon gas molecule is simulated with the Neon at rest and the proton at a given energy (450 GeV or 6.5 TeV). The secondary particles created by this collision are followed on their path and upon passing through any material GEANT4 calculates the interaction in the relevant material. If the material is part of a SciFi detector plane the generated photons are converted into ADC values as it is done by the detector hardware. A software clustering algorithm then creates clusters to match the information that is available for the hardware detector.

Reconstructability criterion

To accurately qualify the capabilities of the reconstruction algorithm a filter was devised to decide if a particle is reconstructible or not. This *reconstructability criterion* requires the particle to:

- be charged
- originate from the primary vertex
- live long enough to travel until after the far station and
- have created at least eight hits, with all of these hits being either in the top or in the bottom half of the detector.

Using these criteria the acceptance of the detector is modelled intrinsically. Figure 4.5 shows the the angular acceptance of the BGV perpendicular to the z-axis compared to the angular distribution of particles originating from the primary vertex.

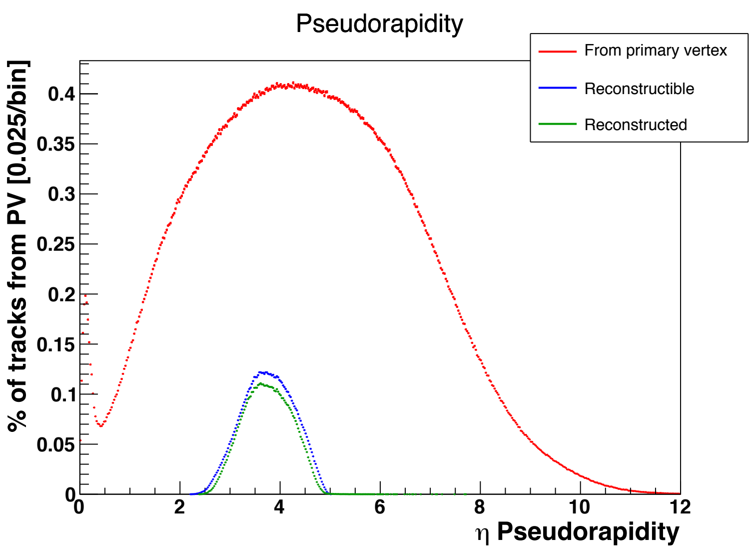

FIGURE 4.5: Comparing the pseudorapidity of simulated tracks (red) with the reconstructible (blue) ones shows the limited coverage of the BGV. Additionally the green curve shows the reconstructed tracks.

Pseudorapidity is frequently used in particle physics to describe angular acceptance and is defined as $\eta = -\ln\left[\tan\left(\frac{\theta}{2}\right)\right]$ with θ being the angle between the track directional vector and the beam axis. A pseudorapidity of greater than five corresponds to an angle of less than 1.56° or a distance to the beam-axis of less than 26 mm after a length of 2 m. This corresponds to the minimum beam-pipe diameter of 52 mm at the first detector station. A significant amount of very forward particles is therefore impossible to detect for the BGV.

Additionally figure 4.6 shows the acceptance in the azimuthal angle as well as the acceptance of the BGV along the z-axis with respect to all simulated particles.

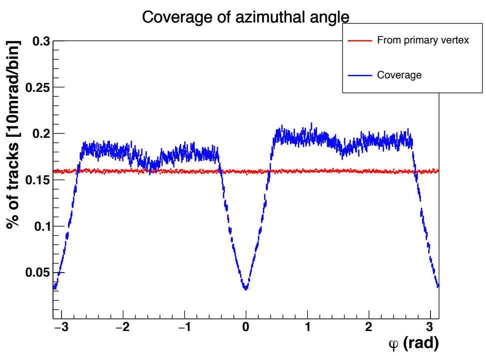

(A) Plot of the polar angle of the track. The visible loss in coverage at 0° and 180° is due to the detector geometry.

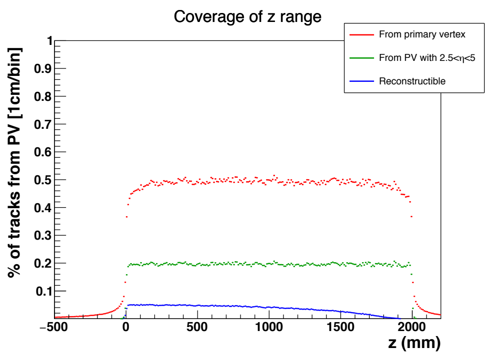

(B) Plot of the z-coordinate of the primary vertex. The decrease in reconstructibility due to the reduced angular acceptance closer to the detector planes (located at 1995 mm) is visible.

FIGURE 4.6: Comparison between all simulated tracks and the ones that are able to be reconstructed based on the detector coverage.

The full MC simulation has been invaluable to the design process and the development of the pattern recognition algorithms for the BGV.

Absolute efficiency

The absolute efficiency of the algorithm is given by the percentage of tracks that should be reconstructable according to the reconstructability criterions defined in section 4.1.3 on the facing page. This is evaluated by taking the clusters of one reconstructable track and passing them to the pattern recognition algorithm. Ideally this should lead to the algorithm returning the combination as there is only one combination possible. If the algorithm failed to produce an output then the window at which it failed to find the only cluster available is recorded as not passed. This is done for all reconstructible tracks of one event individually. The output of the algorithm is given in table 4.1 for one simulated sample of 300 000 events. It shows that the pattern recognition only manages to reconstruct 89.4 % of the reconstructible particles. This defines the upper limit for the overall efficiency of the pattern recognition algorithm.

Efficiency and Purity

Two very important characteristics of a pattern recognition algorithm are its efficiency and purity. They quantify the performance of the pattern recognition algorithm by applying the algorithm to a simulated data sample. Their definitions are:

Efficiency Percentage of reconstructible tracks that are reconstructed.

Purity Percentage of reconstructed tracks that are matched to a simulated particle.

Filter	passed
Window PV	98.3 %
Window 1 (NEAR)	96.9 %
Window 2 (NEAR)	93.4 %
Window 3 (NEAR)	92.2 %
Window 1 (FAR)	91.8 %
Window 2 (FAR)	89.5 %
Window 3 (FAR)	89.4 %

TABLE 4.1: Shows the percentage of reconstructable tracks passing each window consecutively for a simulated sample of 200 µm. Note the larger jumps at both times between the windows 1 and 2. These are the windows responsible for the estimation of the panels which are rotated by 90°.

To have a clear picture the events are grouped by the number of reconstructible tracks they contain. Each event is then passed to the pattern recognition algorithm which returns all the *reconstructed* tracks (i.e. all combinations of eight clusters found). A matching algorithm then checks the clusters of each reconstructed track against the clusters of each reconstructible track. If all eight clusters match, the reconstructed track is marked as matched, otherwise as not matched. We can thus formulate the definitions as:

$$\text{efficiency} = \frac{\text{matched tracks}}{\text{reconstructible tracks}} \tag{4.2}$$

$$\text{purity} = \frac{\text{matched tracks}}{\text{matched} + \text{not matched}}. \tag{4.3}$$

The results of these calculations are shown in figure 4.7 on the next page. The figure shows, that the efficiency is above 70 % for the most important range of 2 to 6 tracks per event, since events with zero or one track cannot be used for calculations. The highest possible value for the efficiency is the aforementioned 89.4 %. This limit is completely independent of the number of tracks per event and just influenced by the pattern recognition algorithm.

The reasons for some tracks not being found come down to the search windows. For computational speed reasons they are chosen to be as narrow as possible to reduce the amount of combinations that need to be checked. This leads to particles that fulfill certain edge cases to not be included in the search window and therefore not found. This trade off is accepted to improve the overall speed of the algorithm and thus the BGV.

As for the purity the increase in reconstructible tracks comes with an increase in occupancy. Some of the clusters in the detector are created by tracks that cannot be reconstructed. These additional clusters are also used by the algorithm during reconstruction leading to tracks including clusters that were not created by the same particle. This leads to so called *ghost tracks*, tracks that are recognized by the system but are not actually created by one single particle. Figure 4.8 shows the percentage of matched clusters for all recognized tracks of a simulated sample. What is especially important to note is, that quite a large percentage of tracks do not contain any clusters of reconstructible tracks.

The fact that clusters not belonging to one track are combined together like this is an intrinsic problem of the number of tracking stations available and cannot be alleviated in the current system.

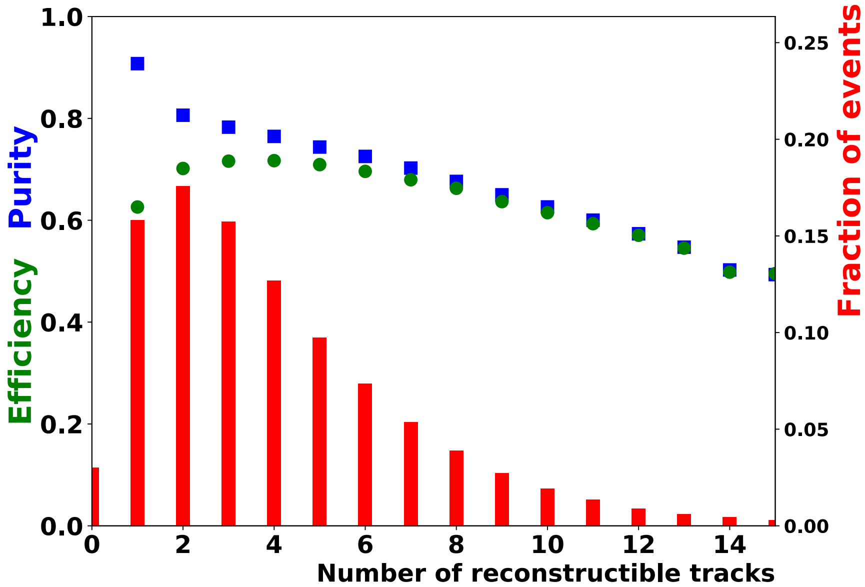

FIGURE 4.7: Shows the efficiency(green circles) and purity (blue squares) of the pattern recognition algorithm as a function of the number of reconstructible tracks. The red bars show fraction of events with the respective number of tracks in a simulated sample with 200 μm and 300k Events.

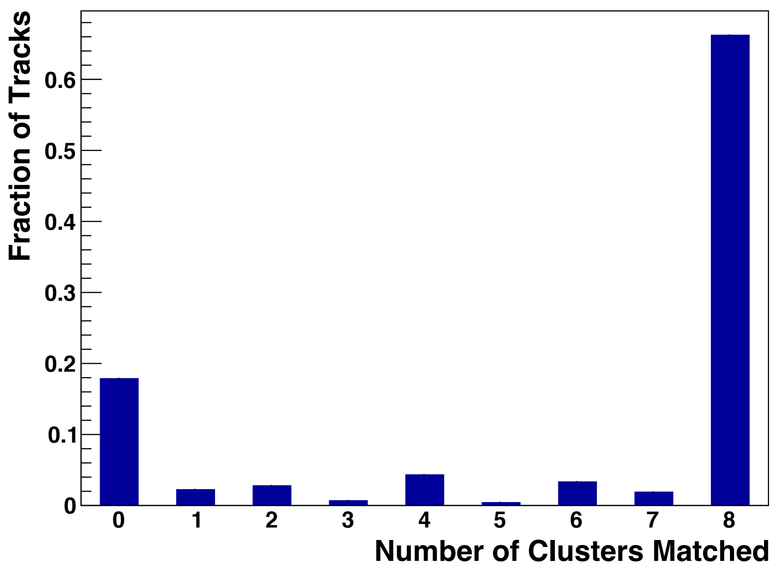

FIGURE 4.8: Showing the percentage of clusters matched for a reconstructed track with eight clusters. It shows that 66 % of recognized tracks match perfectly to one reconstructible and 17.9 % have not a single cluster in common with any reconstructible track.

4.2 Track fitting

Since the BGV does not have a magnetic field and is also only capable of measuring the same coordinate at two locations in z a track is described by a line as point (x, y, z) and vector (tx, ty, tz). To estimate the most optimal parameters for a recognized track the parameters x, y, tx and ty are fitted to the eight selected clusters. The parameter tz is set to 1 to define the direction of the track to be in positive z direction. The position in z is defined as the minimum between the near and far station with different parameters for the top and bottom halves.

A weighted least squares fit is performed by minimizing the squared distance of the track to all eight clusters

$$\min \sum_{i=i}^{8} d_i^2 \cdot w_i \tag{4.4}$$

with w_i the weight of each cluster. The weights are given as $w_i = \frac{1}{\sigma_i^2}$ with σ_i^2 the sum of squared errors relevant for each cluster i. It is calculated as a linear combination of the cluster resolution ($\sigma^2_{\text{cluster}}$) and the multiple scattering error ($\sigma^2_{\text{MS}}(p, z)$).

The cluster resolution of the SciFi modules used by the BGV was measured during a beam test. The resulting σ_{hit} were (38 ± 3) µm for the normal and (43 ± 4) µm for the prime layer [31]. The resolution used for each cluster is calculated from the cluster size and its weight distribution based on

$$\sigma_{\text{cluster}} = \frac{0.25}{\sqrt{12}} \frac{\sum q_i^2}{(\sum q_i)^2} \tag{4.5}$$

with q the charge measured at a strip i of a given cluster.

The multiple scattering error depends on the momentum of the particle as well as the distance of extrapolation from the scattering surface. The error introduced by multiple scattering as a function of the momentum of the particle can be calculated using

$$\sigma(p) = \frac{13.6\,\text{MeV}}{p\beta} \sqrt{\frac{\text{X}}{\text{X}_0}} \left[1 + 0.088 \log_{10}\left(\frac{\text{X}}{\text{X}_0}\right)\right] \tag{4.6}$$

as per [44]. β in this case is the relativistic beta which can be approximated with 1 for most collision products and X/X_0 is the depth of scattering material in units of radiation length. The error a distance z after the scattering surface is given by

$$\sigma_{\text{MS}}(p, z) = \sqrt{z^2 \cdot \sigma^2(p)} \tag{4.7}$$

for a given radiation length. The extrapolation error as derived in [32, Equation 2.7] is given by

$$\sigma_{\text{extrap}}(z) = \frac{\sqrt{(z_2 - z)^2 + (z_1 - z)^2}}{z_2 - z1} \sigma_{\text{cluster}} \tag{4.8}$$

with z_i the positions of the NEAR(1) and FAR(2) planes along the z-axis.

To finally calculate the error of a track at a given position z in the gas target volume we combine the two equations equation (4.7) and (4.8) to form

$$\sigma_{\text{IP}}(z, p) = \sqrt{\sigma_{\text{extrap}}(z)^2 + \sigma^2_{\text{MS}}(p, z)} \tag{4.9}$$

shown in figure 4.9 on the next page.

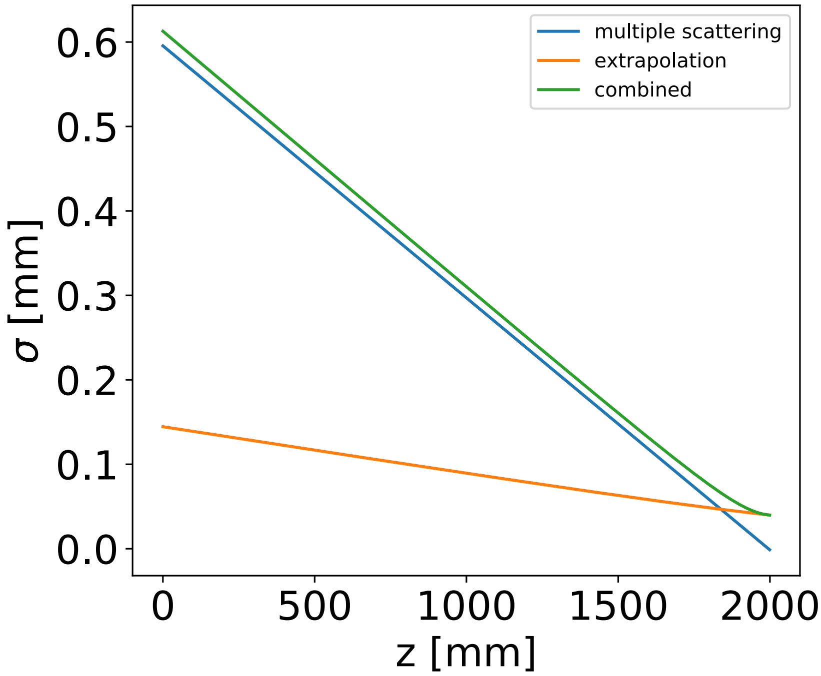

FIGURE 4.9: Extrapolation and multiple scattering errors for the BGV for a secondary particle energy of 9 GeV.

The multiple scattering introduced by the exit window as well as the near station is considered in the far station by adding the corresponding error. Since the MS error depends on the energy of the particle creating the track, which cannot be measured by the BGV, an energy assumption needs to be made. Following from the simulation it is known that 50 % of the particles in the coverage of the BGV are in the range from 0.5 GeV to 7 GeV see figure 4.10a. Investigations with different attempts of estimated errors using monte carlo data show, that the optimal assumption for the energy of a track is 9 GeV as shown in figure 4.10b.

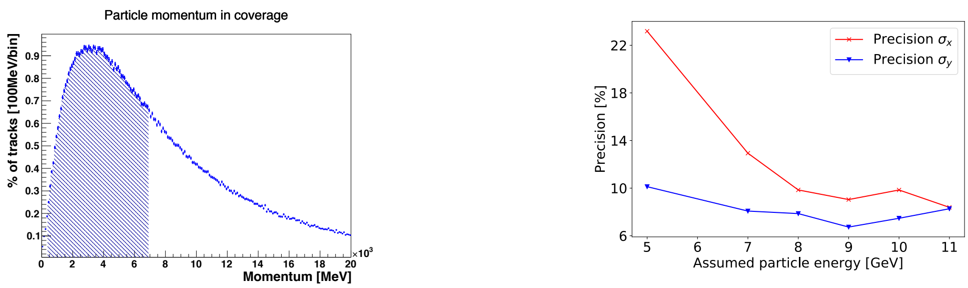

(A) Simulated momentum distribution of particles in the coverage of the BGV. The marked area indicates 50 % of the tracks in the coverage.

(B) Reconstructing the data from a 200 µm sample using different assumptions for particle energy reveals the optimal point around 9 GeV

FIGURE 4.10: Using the momentum information available from simulation to estimate the optimal parameters for track fitting.

Therefore it was decided to use the value for 9 GeV for the fit since it is the mean value for the number of entries per momentum. As a consequence of this, tracks with higher energy have an overestimated error leading lower precision achieved than possible. For tracks with lower energy a higher precision than actually possible is assumed which can lead to a higher χ^2 value during the fit thus removing them.

4.3 Vertexing algorithm

To reconstruct a vertex at least two tracks are required. The addition of more tracks increases the precision of the found vertex known as the vertex resolution.

The BGV vertexing algorithm starts by selecting the first track and checking it's shortest distance to the next track. If this shortest distance is below 0.5 mm the two tracks are considered a starting pair, otherwise the next track is compared to the first. If a pair is chosen the centre on the line of closest approach between the two selected tracks is considered as a temporary vertex. Consecutively the distance of all remaining tracks is computed to this temporary vertex and if the distance is below the limit the temporary vertex is updated to the point closest to all tracks under consideration using the geometric mean. Once all tracks have been considered, the temporary vertex is stored as an accepted vertex and all associated Tracks are marked as used.

4.4 Detector alignment

Great care was taken in placing the components of the BGV at the designated locations. An extensive metrology study was performed to control all aspects of positions within the layers, modules and the modules with respect to each other [32, Appendix A]. To operate at the high precision possible with the BGV a software alignment of the internal components was necessary. The difficulty with this process is the lack of a reference frame due to the low number of measurements available per coordinate (effectively only two per coordinate). To overcome these limitations a multi-step approach was devised that uses all known parameters of the BGV and performs alignment steps consecutively until the whole BGV is aligned.

To align the layers with respect to each other cluster residuals were used. The cluster residual is the distance of a cluster to the track of the particle it was created by. Additionally the concept of unbiased cluster residuals was introduced which are the distance of the cluster to the track without actually using them when fitting the track. Two individual levels are employed to allow for individual corrections.

- Fit using seven clusters and calculate the distance to the eighth for all layers.
- Fit using six clusters of three modules and calculate the distance to the remaining two clusters on the fourth module.

The first allows to correct for offsets between the two layers of one module with the cluster residuals giving similar values on the same module once they are aligned. The second allows to position the module with respect to the other three modules, most importantly the other module of the station it belongs to.

The alignment of the modules with respect to each other was performed using the results from the vertexing algorithm (see section 4.3) because the important parameters for alignment are the mean position and slope of the vertices in the volume. These values can be gained from the simple vertexing algorithm despite its shortcomings regarding beam size measurements discussed in section 5.1 on page 51.

A first noticeable improvement when performing simple alignment steps is the increase in tracks found by the pattern recognition algorithm. This is due to the prefit performed during recognition where a χ^2 cut is performed to select only tracks with an acceptable fit quality.

Following from the higher number of tracks found also more vertices are found. This again improves the alignment capabilities since more information is available to calculate the next alignment step. To increase the accuracy of the alignment every step was performed twice making use of the higher statistics available.

The alignment is a critical component of the BGV performance. When not aligned the results returned by the BGV for the beam size are not correct since the correlation method requires the beam to be centered around the z-axis for the results to make sense.

4.4.1 Alignment corrections

Using Cluster residual plots

Movement of panels within a module, this is generally an alignment of the SiPMs of the normal and prime layers with respect to each other. This movement creates an offset when moving from normal to prime layer that is constant with respect to the other layer thus creating a constant shift in the mean value of the differences between the two layers. This alignment step is complicated by the fact that shifts in one layer influence the offsets in the other layers.

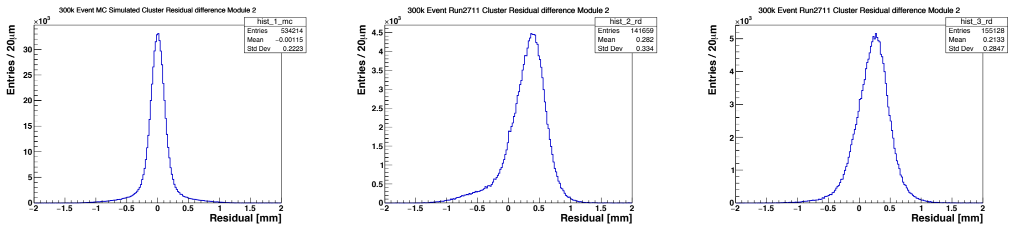

(A) Simulated (B) Before correction (C) After correction

FIGURE 4.11: Difference of the residuals of normal and prime layer of one module on a per track basis to correct for the offset between SIPMs on normal and prime layers. After correction the tail visible in *b* on the left side is gone but the offset is not yet corrected as this is done in the next step.

Once the difference between two layers has been minimized the absolute offset of the parent module to the perpendicular neighbour-module needs to be minimized. To achieve this each module is moved perpendicularly to the strip direction of its normal layer.

Movements of modules with respect to each other, generate a constant offset when switching from one module to the next, this is to some extent equivalent to window 2 which does not actually consider misalignment at all.

Using vertex alignment plots

The vertex alignment is performed with a slightly modified vertexing function that looks for vertices in the top and bottom halves independently. This allows to completely disentangle the two halves and align them individually.

Movements of stations with respect to each other change the positions of the vertices along the z-axis to shapes that are not parallel to the z-axis. The most apparent effect is a slope in x and y direction as shown in figure 4.12 on the following page. Fitting a linear function to the profile of this result gives the slope of the difference between the NEAR and FAR station.

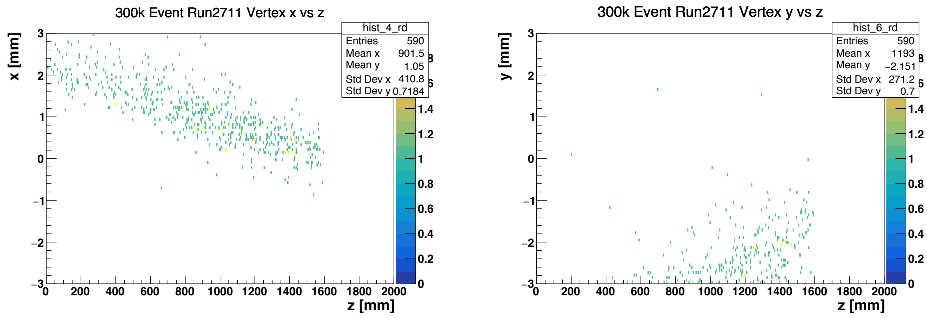

(A) x vs z

(B) y vs z

FIGURE 4.12: After performing only the cluster residual alignment the vertices have a large slope.

To perform the correction the first step is to move one station with respect to the other in a way that minimizes this slope. This needs to be done for the top and bottom halves independently leading to two independently aligned halves. After performing this first correction the number of vertices found increases significantly due to the higher number of tracks found. To improve the alignment further the procedure is repeated with the now higher amount of values and the previous correction values are adapted using the new results.

The next step is to move the independent halves with respect to the z-axis with the goal of minimizing the difference between the centre of the reconstructed vertices and the beam axis figure 4.14 on the next page. This correction is a perpendicular shift leading to an overlapping of the vertices in the two halves.

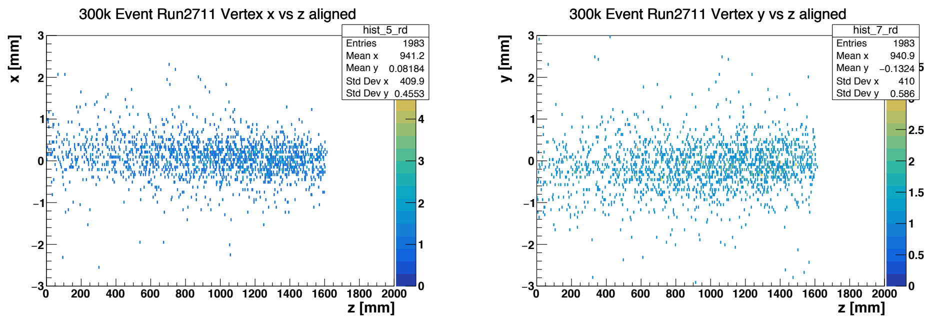

(A) x vs z

(B) y vs z

FIGURE 4.13: After performing the alignment of the near station with respect to the far station and moving the whole bottom layer to its appropriate location the vertices are centered on the z-axis. Additionally the significantly increased number of entries with respect to the previous figure is visible.

As a final check the vertexing algorithm is changed to find vertices using both tracks from the top and bottom half at the same time.

4.4.2 Application of alignment

The parameters resulting from these procedures are then used to move the objects in the geometry model of the analysis framework to as closely as possible resemble the positions of the physical modules of the BGV in the tunnel. These geometry values are used throughout the analysis for all fitting procedures during the reconstruction.

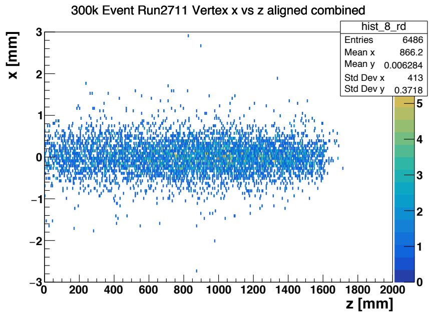

(A) x vs z

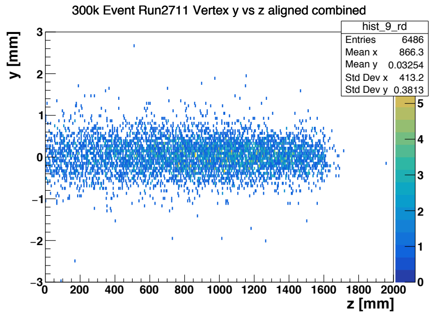

(B) y vs z

FIGURE 4.14: Requiring vertices to have tracks from top and bottom gives the confirmation that the combined alignment suceeded.

Additionally, since the first search window requires the information on the strip closest to the beam pipe centre this value is updated after the alignment is performed to achieve the highest possible efficiency of the search windows. Since all remaining search windows are relative to the GeoIDs selected in the first step this correction propagates automatically.

4.5 Summary of performance with real data

After performing the alignment of the BGV the performance of the algorithm is evaluated and compared to the simulated dataset. One of the fundamental comparisons is the track multiplicity per event when applying the same cluster filtering limits to simulated data as they are applied to acquired data in the HLT (see table 3.2 on page 34) but not filtering by tracks. The result shown in figure 4.15 shows a reasonable equivalence between simulated and acquired data. One can also use the reconstructible track multiplicity from figure 4.7 on page 43 as a point of comparison which also matches very well with the exception of the events with no tracks.

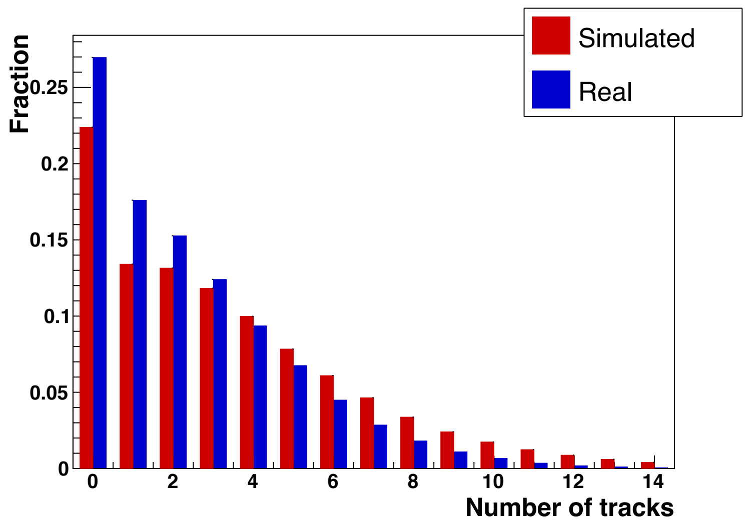

FIGURE 4.15: Comparison of the track multiplicity of simulated and real data. The real data sample is only filtered using the cluster filters to provide a complete picture of all events.

Another comparison of reconstructed tracks with predictions can be performed by comparing the DOCA error calculated using equation (4.9) on page 44 and shown in figure 4.9 on page 45 with figure 4.16. The extrapolation error is calculated using

$$\sigma_x(z) = \sqrt{\sigma_x^2 + (z - z_1)^2 \cdot \sigma_{t_x}^2} \quad (4.10)$$

with σ_x^2 and $\sigma_{t_x}^2$ taken from the covariance matrix of the four parameter fit described in section 4.2 on page 44. An equivalent equation can be constructed using σ_y and σ_{t_y}. Again the prediction matches the values calculated from the measurements very closely.

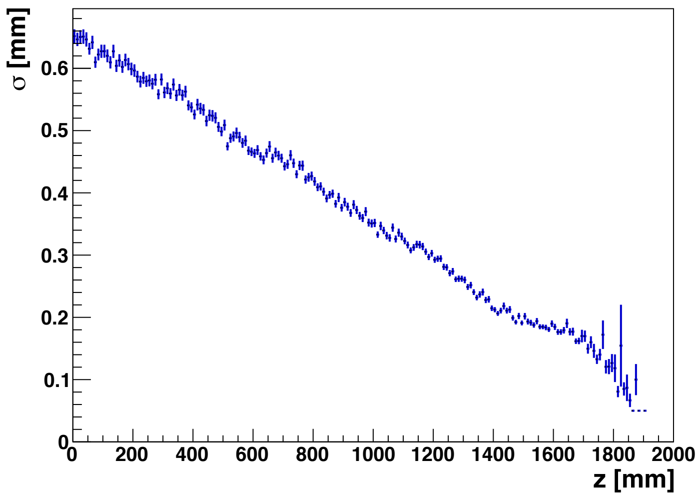

FIGURE 4.16: Plotting the extrapolation error of the track at the POCA over the z-coordinate of the POCA shows, that the expected extrapolation error (see figure 4.9 on page 45) matches closely to the one calculated using the covariance matrix of the track fit.

Chapter 5

Beam profile measurement

This chapter explores two possible methods to perform a beam size measurement using the tracks provided by the BGV and reviews the benefits and shortcomings of each.

5.1 Vertexing method

One method to gain knowledge about the beam size and position is to reconstruct the vertex of the collision between the proton of the beam and the gas-molecule. The statistical distribution of these vertices is directly correlated to the size of the bunch. The vertexing algorithm developed for the BGV is given in section 4.3 on page 46.

Even with this very generous acceptance region of 0.5 mm half of the events with two or more tracks do not contain a recognized vertex as shown in figure 5.1a on the following page.

The measured (raw) distribution is a convolution of the vertex resolution and the beam sigma as given by

$$\sigma_{\text{raw}}^2 = \sigma_{\text{beam}}^2 + \sigma_{\text{vertex}}^2. \tag{5.1}$$

Thus to calculate σ_{beam} from the measured sigma the vertex resolution needs to be known with high precision. At first there was no clear way of independently assessing the vertex resolution and thus a second method, the correlation method described in the next section, was used to calculate the beam size. Now, since the beam sizes are known for any given run, the vertex resolution can be calculated and the vertexing method revisited. The results, as shown in figure 5.2a on the next page, reveal that the vertex resolution depends to a large degree on the number of tracks used.

Additionally, it becomes immediately apparent that the vertex resolution in most cases is larger than the sigma of the beam to be measured. Starting from vertices with 5 or more tracks measurements for x have a σ_{vtx} lower than the measured values (approx 220 µm). For the y axis this limit is never reached. This introduces a significant systematic error into the calculations leading to a very large error on the measurement of σ_{beam}. Additionally, vertices with 5 or more tracks in them make up around 0.09 % of all vertices (figure 5.1b on the following page) which themselves make up only 54 % of all filtered events. A different method of calculating the beam size is therefore required to achieve the goal of the BGV.

5.2 Correlation method

Another method of calculating the beam size is to use the correlation between the tracks originating from the same vertex. This method was previously applied in the

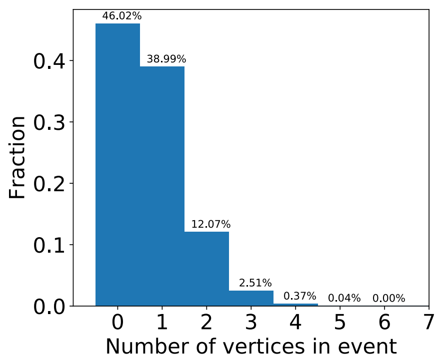

(A) Multiplicity of vertices per event for LHC fill 7334.

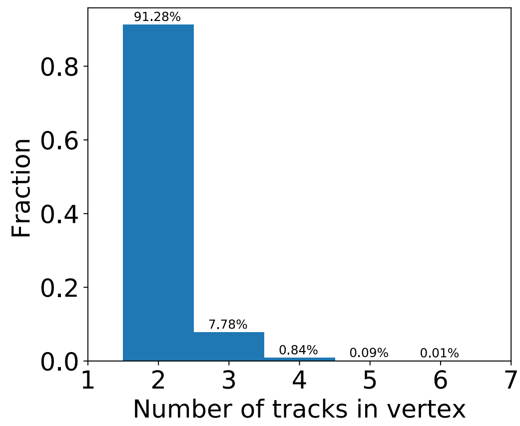

(B) Multiplicity of vertices with different numbers of tracks for LHC fill 7334

FIGURE 5.1: Vertex multiplicities

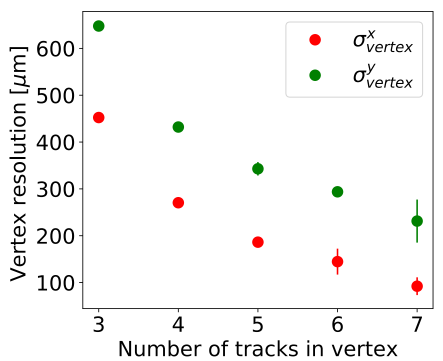

(A) Shows the vertex resolution for four independent runs calculated separately for the horizontal and vertical axis calculated from $\sigma^2_{\text{vertex}} = \sigma^2_{\text{raw}} - \sigma^2_{\text{beam}}$. The values for σ^2_{beam} are calculated using the correlation method.

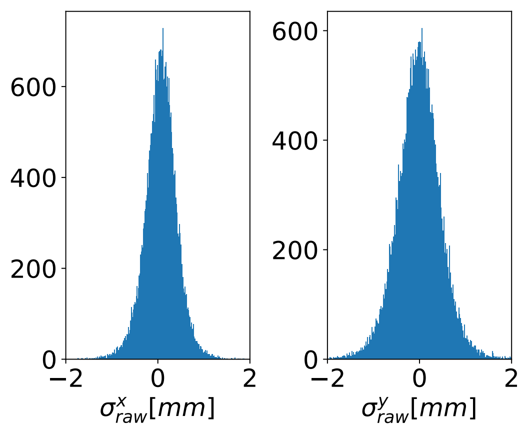

(B) Profiles of the raw vertices in x and y for vertices with 4 tracks.

FIGURE 5.2: Vertex resolution plots

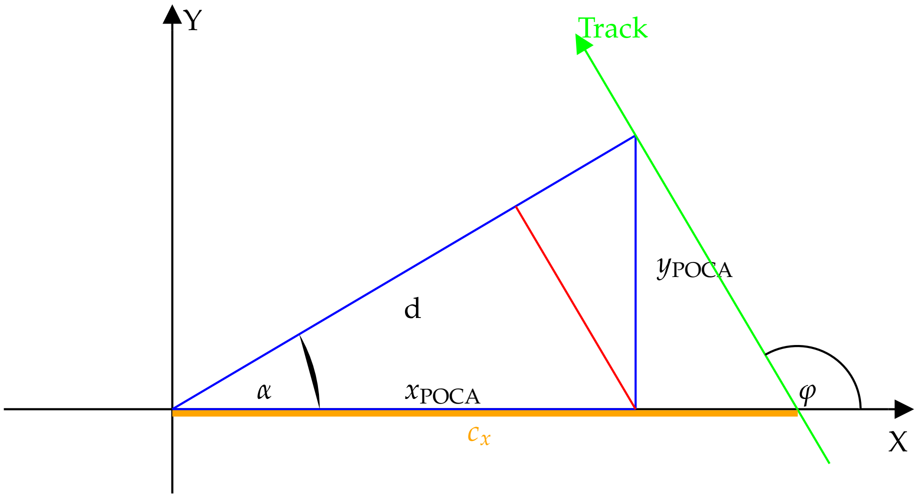

FIGURE 5.3: The length of the side d can also be represented using $d = x_{\text{POCA}} \cos\alpha + y_{\text{POCA}} \sin\alpha$ by splitting the triangle in two.

CDF experiment [45] and also used as an additional source of information in the CMS experiment [46].

5.2.1 Impact parameter

Any two lines in three dimensional space that are not parallel have a minimal distance to each other called the Distance Of Closest Approach (DOCA). Following from this there is a point on each line that has the shortest distance to the other line, the Point Of Closest Approach (POCA). The impact parameter is the DOCA between a given line and the z-axis in three dimensional space. The POCA on the line is then given by the coordinates $(x_{\text{POCA}}, y_{\text{POCA}}, z_{\text{POCA}})$. The DOCA vector is always perpendicular to the z-axis allowing us to consider the situation in two dimensions using $(x_{\text{POCA}}, y_{\text{POCA}})$. The distance is given by the hypotenuse of the triangle as given by

$$d = x\cos\alpha + y\sin\alpha \tag{5.2}$$

which, as shown in figure 5.3 can be applied to the impact parameter (IP). Since one doesn't have the angle α of this triangle but only the angle φ of the track in its x-y projection the following conversion needs to be applied.

$$\sin\alpha = \sin(\varphi - \frac{\pi}{2}) = \cos(\frac{\pi}{2})\sin\varphi - \sin(\frac{\pi}{2})\cos\varphi \tag{5.3}$$

$$\cos\alpha = \cos(\varphi - \frac{\pi}{2}) = \sin(\frac{\pi}{2})\sin\varphi + \cos(\frac{\pi}{2})\cos\varphi \tag{5.4}$$

From these equations follow the following relations: $\sin\alpha = -\cos\varphi$ and $\cos\alpha = \sin\varphi$. Inserting this into equation (5.2) leads to:

$$d = x \cdot \sin\varphi - y \cdot \cos\varphi \tag{5.5}$$

Another way of deriving this relation can be done by starting with the track equation $y = a \cdot x + b$. The slope of the track is given by $a = \frac{s_y}{s_x} = \frac{\sin\varphi}{\cos\varphi} = \tan\varphi$. Using an arbitrary point of the track one can define $p_y = p_x \cdot \tan\varphi + b$ therefore $b = p_y - p_x \cdot \tan\varphi$. Another representation, using the distance where the track cuts the x-axis (c_x) and the angle α gives $d = c_x \cdot \cos\alpha$ which (using the representation

$\alpha = \varphi - \frac{\pi}{2}$) gives $d = c_x \cdot \sin\varphi$. Evaluating at the point where the track cuts the x-axis we can say $0 = \tan\varphi \cdot \frac{d}{\sin\varphi} + b$ which with our previous definition of b leads to $0 = \tan\varphi \cdot \frac{d}{\sin\varphi} + p_y - p_x \cdot \tan\varphi$. Solving this for d gives

$$d = p_x \cdot \sin\varphi - p_y \cdot \cos\varphi. \tag{5.6}$$

Since we used an arbitrary point on the track for the definition this equation works with any point on the track but always returns the minimal distance to the reference point.

This can be used to calculate the offset of the beam center from the mathematical center by plotting the track angle φ over the impact parameter. As shown in figure 5.4 for a simulated sample the parameters x and y of the fit return an offset. The offset is smaller than the simulated one due to the amount of ghost tracks present in the sample.

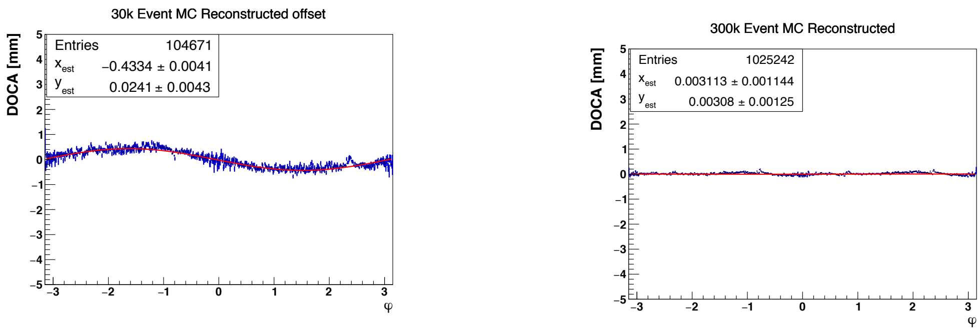

(A) Simulated sample shifted from the beam axis by 0.6 mm in x. The DOCA-φ fit returns an offset smaller than expected. This is due to ghost tracks as described in the next section.

(B) After centering the beam on the coordinate center (e.g. after the alignment has been performed).

FIGURE 5.4: The impact parameter can be used to calculate the offset of the beam center from the axis center. A fit using equation (5.5) on the previous page for the parameters x and y returns the offset in both.

5.2.2 Impact parameter correlation

We can evaluate the correlation between impact parameters of track pairs originating from the same vertex as follows:

$$\langle d_1 d_2 \rangle = \langle (x_v \cdot \sin\varphi_1 - y_v \cdot \cos\varphi_1) \cdot (x_v \cdot \sin\varphi_2 - y_v \cdot \cos\varphi_2) \rangle \tag{5.7}$$

With $d_1 d_2$ signifying the multiplication of two DOCAs from the same event and the brackets signifying the averaging over multiple events. An equivalent calculation is performed for the φ_i dependent terms where φ_i is calculated for each track i individually. Thus at first the values for each pair of tracks recognized in one event are calculated and then the average of the results are used.

Expanding this equation gives

$$\langle d_1 d_2 \rangle = \langle y^2 \rangle \cdot \cos\varphi_1 \cos\varphi_2 + \langle x^2 \rangle \cdot \sin\varphi_1 \sin\varphi_2 - \langle xy \rangle \sin(\varphi_1 + \varphi_2) \tag{5.8}$$

which is equivalent to

$$\frac{1}{2}(\langle y^2\rangle - \langle x^2\rangle)\cos(\varphi_1+\varphi_2) + \frac{1}{2}(\langle y^2\rangle + \langle x^2\rangle)\cos(\varphi_1-\varphi_2) - \langle xy\rangle\sin(\varphi_1+\varphi_2). \tag{5.9}$$

We can now define a rotation matrix between the local coordinate system and the beam rotation coordinate system to fulfill the condition that the symmetric matrix

$$\begin{bmatrix} \langle\zeta_1^2\rangle & \langle\zeta_1\zeta_2\rangle \\ \langle\zeta_1\zeta_2\rangle & \langle\zeta_2^2\rangle \end{bmatrix}$$

is diagonal ($\langle\zeta_1\zeta_2\rangle = 0$).

By defining $\langle\zeta_1^2\rangle = \sigma_1^2$ and $\langle\zeta_2^2\rangle = \sigma_2^2$ and applying the rotation matrix to equation (5.9) we obtain

$$\langle d_1 d_2\rangle = \frac{1}{2}(\sigma_1^2+\sigma_2^2)\cos(\varphi_1-\varphi_2) + \frac{1}{2}(\sigma_1^2-\sigma_2^2)\cos(\varphi_1+\varphi_2-2\alpha) \tag{5.10}$$

with α being the angle of rotation between the beam frame and the accelerator frame.

It should be noted that the average IP correlation is independent of the IP measurement resolution. By adding a random error ϵ to each measurement, one gets:

$$\langle(d_1+\epsilon_1)(d_2+\epsilon_2)\rangle = \langle d_1 d_2\rangle + \langle d_1\epsilon_2\rangle + \langle d_2\epsilon_1\rangle + \langle\epsilon_1\epsilon_2\rangle. \tag{5.11}$$

Assuming statistical independence between errors and measurements, $\langle d_i\epsilon_j\rangle = \langle d_i\rangle\langle\epsilon_j\rangle$ and $\langle\epsilon_1\epsilon_2\rangle = \langle\epsilon_1\rangle\langle\epsilon_2\rangle$, giving $\langle(d_1+\epsilon_1)(d_2+\epsilon_2)\rangle = \langle d_1 d_2\rangle$ (provided the measurements do not introduce any systematic bias, $\langle\epsilon\rangle = 0$).

If the beam is circular equation (5.10) simplifies to

$$\langle d_1 d_2\rangle = \sigma_b^2 \cdot \cos(\varphi_1-\varphi_2) \tag{5.12}$$

For the case of a non-circular beam as it is expected with the LHC the second term in equation 5.10 with the usage of a fixed α allows for the calculation of the difference between the two beam axis. By fitting the values $\sigma_{sum}^2 = \frac{1}{2}(\sigma_1^2+\sigma_2^2)$ and $\sigma_{diff}^2 = \frac{1}{2}(\sigma_1^2-\sigma_2^2)$ the individual σ_i^2 values can be calculated:

$$\begin{aligned} \sigma_1^2 &= \sigma_{sum}^2 + \sigma_{diff}^2 \\ \sigma_2^2 &= \sigma_{sum}^2 - \sigma_{diff}^2 \end{aligned} \tag{5.13}$$

The values σ_{sum}^2 and σ_{diff}^2 can be calculated by fitting a line to the points in a correlation vs $\cos(\Delta\varphi)$ and $\cos(\Sigma\varphi)$ plot respectively (figure 5.5 on the following page).

To determine the accuracy of the correlation method a simulated dataset of 300 000 collisions was generated using the full monte carlo simulation. The beam size of the simulated sample was chosen to be 200 µm to be representative of the smallest beam size to be measured by the BGV at LHC top energies (6.5 TeV).

The first step was to confirm that the mathematical model works by using the MCTruth values, the perfect tracks originating from the interaction point. This data is per definition without any measurement or reconstruction errors and should return the exact values simulated.

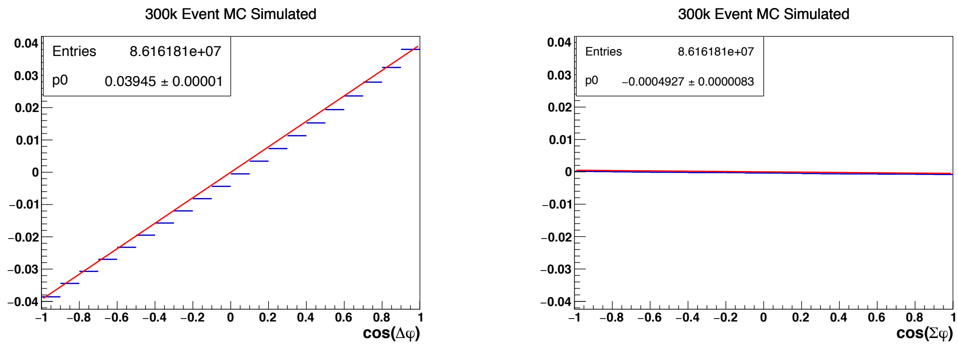

(A) Correlation vs $\cos\Delta\varphi$ fit (B) Correlation vs $\cos\Sigma\varphi$ fit

FIGURE 5.5: Using the Monte Carlo truth values the applicability of the method can be shown for a sample with a simulated round beam of 200 µm.

For the values given in figure 5.5 the results are

$$\begin{aligned}\sigma_1 &= \sqrt{0.03945 - 0.00049} = 0.197\,\text{mm and} \\ \sigma_2 &= \sqrt{0.03945 + 0.00049} = 0.200\,\text{mm}\end{aligned} \tag{5.14}$$

confirming, that the mathematical model can be used to calculate the beam size using BGV tracking data.

The next step was to impose the geometry and by extension the angular coverage of the BGV on the MCTruth values by switching to the usage of *reconstructible tracks* (as defined in section 4.1.3 on page 40). This reduces the amount of tracks available substantially as can be seen in the number of entries between figure 5.5 and figure 5.6.

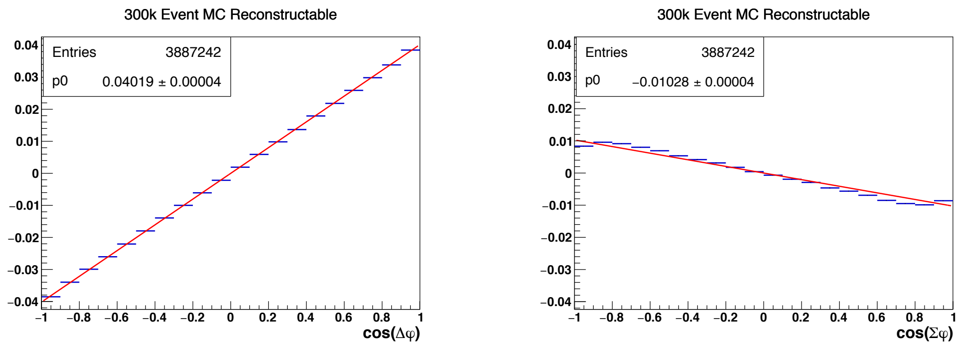

(A) Correlation vs $\cos\Delta\varphi$ fit (B) Correlation vs $\cos\Sigma\varphi$ fit

FIGURE 5.6: Correlation plots for only reconstructible tracks from the same 200 µm MC sample.

Calculating the beam size from these fits the results are

$$\begin{aligned}\sigma_1 &= \sqrt{0.04 - 0.01} = 0.173\,\text{mm and} \\ \sigma_2 &= \sqrt{0.04 + 0.01} = 0.224\,\text{mm}\end{aligned} \tag{5.15}$$

with a clear difference between the two sigma axies although a round beam was simulated. Since the only change between the two calculations is the introduction of the geometry of the BGV this effect must be due to the asymmetric coverage created by the space required by the beam 1 pipe. The result comes out correctly if we impose the knowledge of the beams roundness on the calculation by using equation (5.12) on page 55 but we cannot assume this for BGV measurements in general. It is therefore clear, that this effect will also exist in reconstructed tracks and needs to be corrected for.

Continuing on with the same MC sample but this time using the tracks reconstructed from the simulated clusters gives the result shown in figure 5.7.

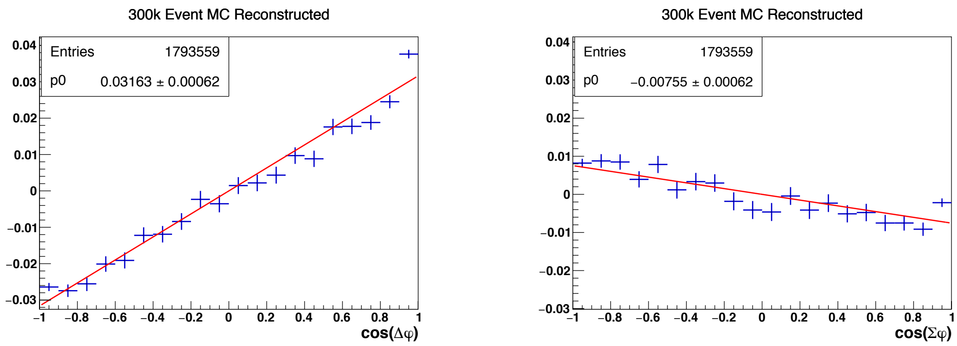

(A) Example of a correlation vs cos $\Delta\varphi$ fit

(B) Example of a correlation vs cos $\Sigma\varphi$ fit

FIGURE 5.7: Correlation plots for reconstructed tracks from the same 200 µm MC sample.

The results of this fit are giving the following values:

$$\begin{aligned} \sigma_1 &= \sqrt{0.0316 - 0.0075} = 0.155\,\text{mm and} \\ \sigma_2 &= \sqrt{0.0316 + 0.0075} = 0.198\,\text{mm.} \end{aligned} \tag{5.16}$$

The change from reconstructible to reconstructed tracks includes a lot of changes, amongst other things:

- Imprecision of each measured cluster applied to cluster measurements
- Multiple scattering error applied during track fitting
- Not all possible tracks are found (efficiency)
- Not all found tracks are actually created by one particle (purity)

All these additional factors need to be considered when examining this result. The first three affect the precision of the measurement by introducing random errors on the tracks. As previously shown these random errors don not actually influence the result but do increase the amount of entries required to achieve the same precision.

On the other hand the fourth change, the introduction of ghost tracks, influences the accuracy of the measurement. Since they are randomly distributed they are not correlated to each other. Averaging over non-correlated track correlations leads to a mean value of zero but since the beam size measurement depends on the slope of the correlations an increase of values around zero decreases the overall slope. This leads to an underestimation of the beam size as is shown in the values of equation (5.16) in comparison to equation (5.15) on the facing page. To minimize the inclusion of ghost tracks in the correlation calculation a limit was introduced requiring the distance between the z-coordinate of the POCA of the tracks to be correlated to be less than 40 mm.

5.2.3 Correction functions

To compensate for the under-estimation due to ghost tracks and the value offset due to the asymmetric coverage a correction function needed to be developed. To this end multiple different beam-sizes were simulated using the full MC simulation to also categorize the behaviour with different beam sizes. The results of these efforts are shown in figure 5.8 for the two axes independently.

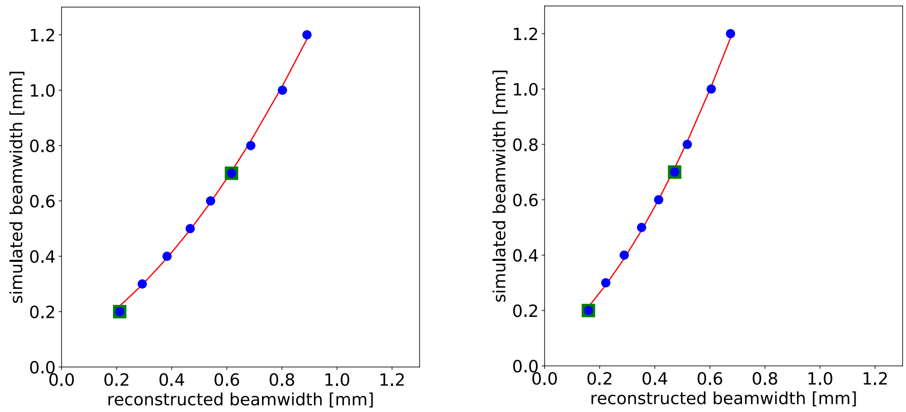

(A) σ_x^{MC} vs σ_x^{rec} (B) σ_y^{MC} vs σ_y^{rec}

FIGURE 5.8: Reconstructed beam size σ^{rec} plotted against the corresponding MC generated beam size σ^{MC}. The red line is a quadratic fit to the data. The two green squares are beam size estimations for two additional MC samples that were not used in the line fit.

The numerical values for the correction function are

$$\begin{aligned} \sigma_x^{\mathrm{cor}} &= 0.81(\sigma_x^{\mathrm{rec}})^2 + 0.53\sigma_x^{\mathrm{rec}} + 0.07 \text{ and} \\ \sigma_y^{\mathrm{cor}} &= 1.39(\sigma_y^{\mathrm{rec}})^2 + 0.72\sigma_y^{\mathrm{rec}} + 0.06\,. \end{aligned} \tag{5.17}$$

The correction requirement introduces a systematic error into the measurement that cannot be removed.

5.2.4 Beam size reconstruction of rotated, elliptical beams

The beam does not necessarily need to be aligned with the beam axis. Using equation (5.10) on page 55 the size of the two primary axis of such a beam as well as the angle of rotation with respect to the beam axis can be calculated. To do this the function needs to be fitted to the three parameters σ^2_{sum}, σ^2_{diff} and α. The values for σ_x and σ_y can again be calculated using equation (5.13) on page 55. Again, just as with the fits described in the previous section, the values need to be corrected using the simulated samples. The values for this function differ from the previous and are

$$\begin{aligned} \sigma_x^{\mathrm{cor}} &= 0.65(\sigma_x^{\mathrm{rec}})^2 + 0.86\sigma_x^{\mathrm{rec}} + 0.02 \text{ and} \\ \sigma_y^{\mathrm{cor}} &= 0.79(\sigma_y^{\mathrm{rec}})^2 + 0.88\sigma_y^{\mathrm{rec}} + 0.03\,. \end{aligned} \tag{5.18}$$

For the beam to exhibit a behaviour that can be considered rotated the beam sizes need to differ for the two axis of the beam, giving the beam an elliptical shape. The fit used returns the length of these two axis as well as the angle of rotation with respect to the accelerator coordinate system.

One interesting question now is, how much the lengths of the axis of the ellipse need to differ to register a rotation. To this end a toy simulation was developed that allows the simulation of beams with arbitrary sizes for the beam axis. The results given in figure 5.9 shows, that after a difference of about 10 % the simulated angle of 20° is correctly recognized.

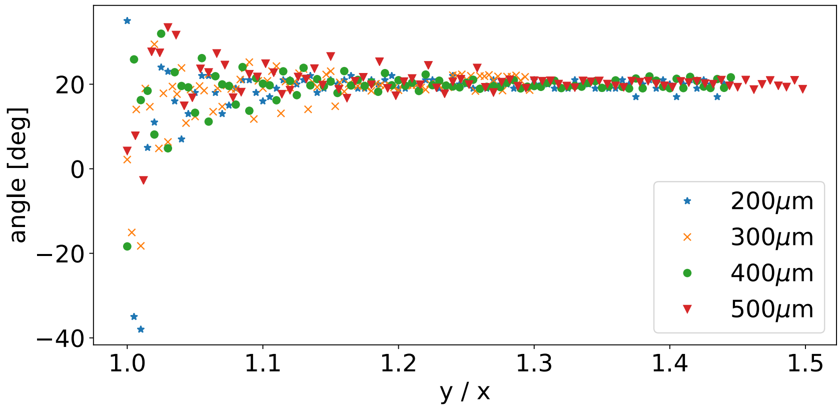

FIGURE 5.9: Shows the angle recognized by the fit in dependance on the ratio of sizes for x and y. The color denotes the size of the x coordinate of the ellipse.

An additional interesting point is the fact that to the fit function a beam rotated by δ looks equivalent to a beam rotated by $\pi - \delta$ with the primary axis swapped. This leads to a problem with the correction function since the functions differ for x and y and give wrong results when the values returned by the fit are swapped. This fit method can therefore not be used independently but can aid with providing additional information that might be interesting during the operation of the LHC.

5.2.5 Reconstruction using half of the detector

Due to a hardware problem only one half of the BGV was available during a period of operation in 2017. This revealed, that the BGV can also be run using only one half of the detector. The results for the same amount of events are less precice due to only half of the tracks being available. Additionally a slightly different correction value is necessary due to the different coverage of only one half.

In figure 5.10 on the next page the figures from figure 5.7 on page 57 are given using only one half of the detector for the same datasample.

The reduction of the precision of the measurement when using only half of the detector is equivalent to halving the amount of tracks per event. The effective loss in precision is a reduction of the number of entries to one quarter which is equivalent to half the precision. Therefore half of the detector gives half of the precision which in turn requires a fourfold increase in integration time to achieve the same precision as with the full detector as described in the next section.

5.3 Uncertainties and Precision

To understand the precision of any individual measurement multiple consecutive measurements with the same number of entries per correlation plot were plotted in a histogram (figure 5.11 on the next page). The histograms show Gaussian distributions, indicating, that the accuracy of the individual measurements follows Gaussian

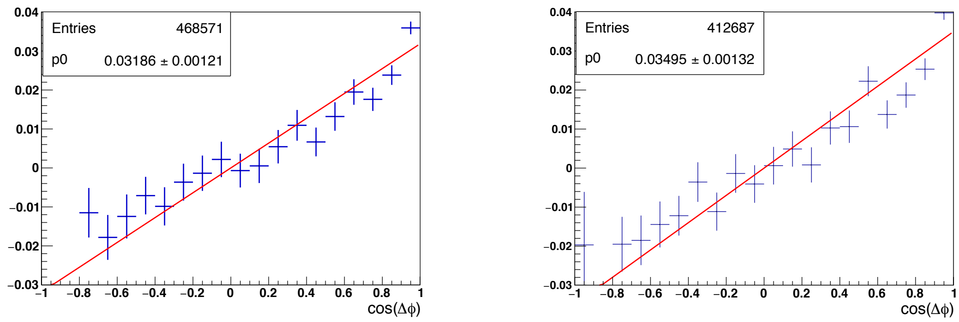

(A) Correlation vs $\cos\Delta\varphi$ using only tracks from the top half of the detector.

(B) Correlation vs $\cos\Delta\varphi$ using only tracks from the bottom half of the detector.

FIGURE 5.10: Correlation plots for reconstructed tracks from the same 200 µm MC sample split into results for the two halves. Note the amount of entries being less than half of figure 5.7 due to the lower amount of combinations possible per event.

statistics. Changing the number of entries required per integration window for the same dataset reduces the amount of entries per histogram and at the same time narrows the distribution.

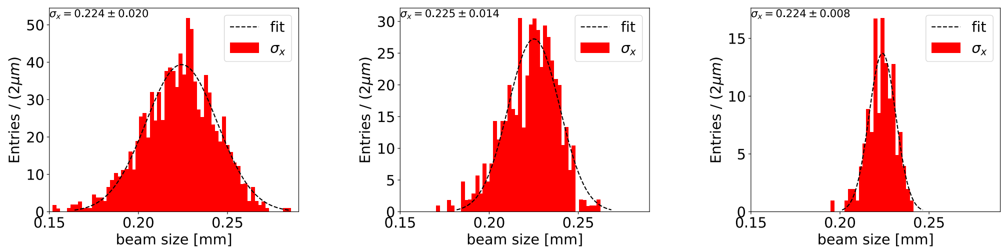

(A) 25 000 Entries

(B) 50 000 Entries

(C) 200 000 Entries

FIGURE 5.11: Putting consecutive measurements with the BGV at constant energy in a histogram shows a nice gaussian distribution. Changing the integration time leads to a narrower distribution i.e. an increase in precision.

Following from this we can conclude that the statistical error of any individual BGV measurement at a given energy depends solely on the amount of entries in the correlation plot. The expected behaviour for a gaussian distribution is that the precision increases with $1/\sqrt{N}$ with N the number of entries. This is the case for the BGV measurements as can be observed in figure 5.12 on the facing page. At some point the precision does not continue to increase as expected but instead remains constant (about 8 µm for 450 GeV) which corresponds to an error of 1 % for the beam size at this energy.

The number of entries is not really a good way to communicate the precision. To equate the number of entries in the correlation plot with the number of events used one has to look at the number of entries per event which is dependent on the beam energy (figure 5.13 on the next page). The higher number of entries per event for higher energies increases the absolute precision but for a smaller beam size.

The resulting plot in figure 5.14a on page 62 can be used to calculate the precision achievable for a given range of events recorded. It is also very valuable to estimate

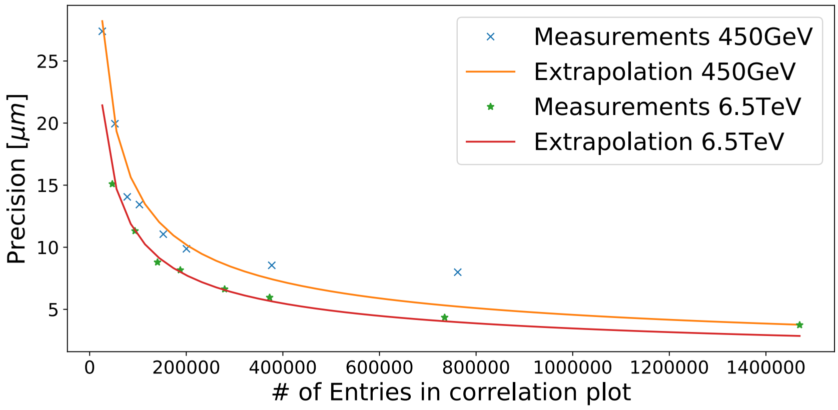

FIGURE 5.12: Plotting the sigma of histograms from different amounts of entries per correlation plot shows a clear $1/\sqrt{N}$ dependence before remaining constant.

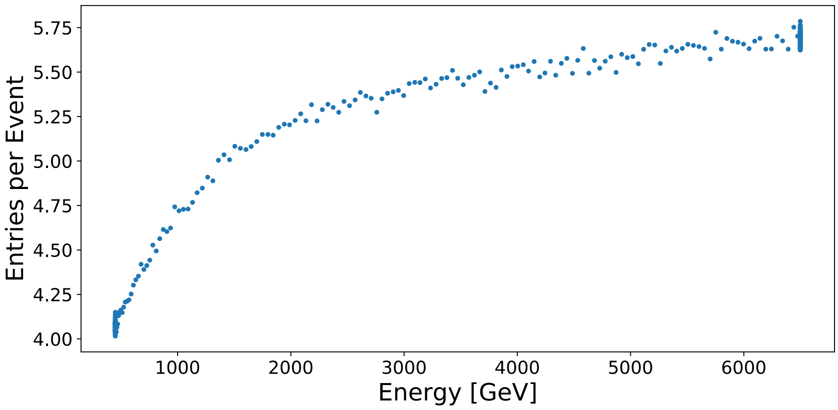

FIGURE 5.13: Number of entries per event based on accelerator energy.

the bunch-by-bunch precision of the BGV which is limited by the beam-gas interaction rate. When assuming an interaction rate of 200 Hz and a required precision of 10 µm the number of required events is 20 000 equal to 100 s of integration time. Following from the $1/\sqrt{N}$ dependence it is clear that to achieve 5 µm precision the integration time needs to be increased to 400 s.

When averaging over all bunches the trigger rate of the BGV demonstrator is currently limited to around 4.5 kHz due to the available CPU capacity. Using the precision based on number of events one can also express the precision based on integration time for a given event rate (figure 5.14b).

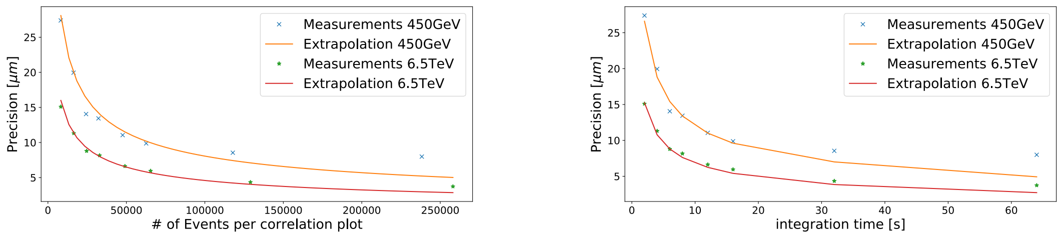

(A) Precision of measurement based on number of events used.

(B) Precision of measurement based on integration time for an event rate of 4 kHz

FIGURE 5.14: The precision achievable with the BGV demonstrator.

Or, equivalently, these values can also be expressed as relative precision of the measurement for a given integration time figure 5.15. This allows us show, that the BGV is capable of achieving the 2 % precision set forth by the requirements given in section 3.1 on page 21 for average beam size measurements.

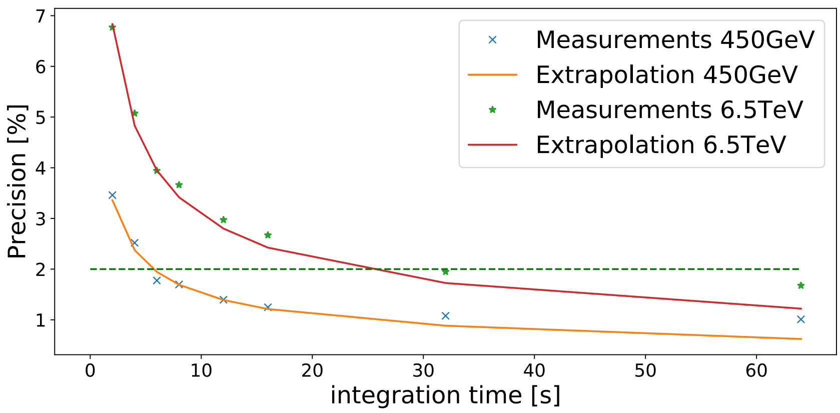

FIGURE 5.15: Relative precision achieved for figure 5.14b.

The systematic uncertainties are introduced by the misalignment of the detector and the correction function required to correct for the incomplete coverage of the BGV and the precision achieved. To characterize these kinds of uncertainties a comparison with another measurement device is necessary. Two such comparisons are performed in section 6.4 on page 71

Chapter 6

Results

6.1 Types of measurements

The BGV can be used to measure the beam size of individual bunches, selected trains or up to the average beam size of the whole LHC fill. The most common usage is the measurement of the average beam size since it provides the most precise result in the shortest amount of time.

6.1.1 Average beam size

When measuring the average beam size every datasample that passes the event selection criteria defined in section 3.6.3 on page 33 is taken into consideration. Integrating over samples from many different bunches has the inherent problem that not all bunches have the same size. The average beam size is therefore influenced by the number of contributions taken from the selection of bunches. This selection is firstly based on the trigger selection, which is inherently random, followed by the available processing capacity of the TELL1 boards which depends on the time since the last event happened. At the same time the availability of the HLT is checked which depends in part on the duration the previous event took to compute. All of this combined leads to an uneven acquisition of data per bunch as can be seen in figure 6.1 on the following page. The cause for this shape of the rate per bunch is a combination of the dead time of the trigger caused by the constant fraction discriminator combined with the probability that a part of the system is still occupied with a previous event.

As can be seen in figure 6.2 on the next page the absolute result is not influenced by this beyond the expected error of the measurement in general. This plot again shows the increase in precision with the increase in acquired data in the narrowing spread of measured beam size.

As a consequence the result of an average beam size measurement is representative of the actual average beam size despite the bias towards the first bunch of each train.

The BGV in its current configuration is capable of reaching a measurement precision of better than 5 µm in under 30 s for average beam size measurements.

6.1.2 Bunch by bunch measurements

Measurements of individual bunch sizes can easily be performed since the bunch ID is stored with every event. As shown in the previous subsection individual bunch sizes can be calculated for a standard average beam profile dataset. With the current system the per bunch data rate for such a dataset is too low to achieve a meaningful precision in a reasonable time.

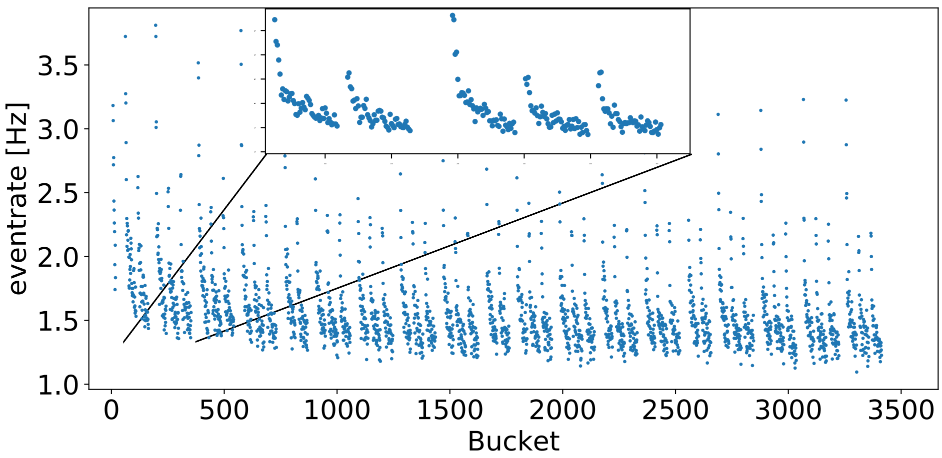

FIGURE 6.1: Eventrate per bunch for fill 7334 with 2556 bunches. The zoomed plot shows the bucket range from 55 to 375. The decrease in acquired events for the bunches later on in the train is visible. It is also visible that the gap between two trains determines the acquisition rate of the following train.

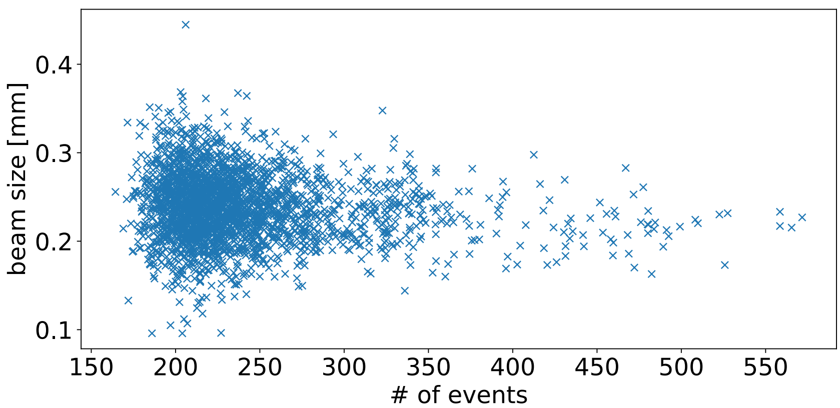

FIGURE 6.2: Shows the beam size with respect to the number of events used for calculating it. It shows, that the beam size estimate for the individual bunches only varies within the error of the measurement and again shows the increase in precision with the increase in events used.

When looking at a fill with a lower amount of injected bunches, 14 in this case, the read-out rate is not limited by the maximum data rate. As can be seen in figure 6.3 the data rate is much higher in general and the per bunch rate, which depends on the bunch intensity, behaves similarly to the intensitites measured by the beam current transformer (BCT).

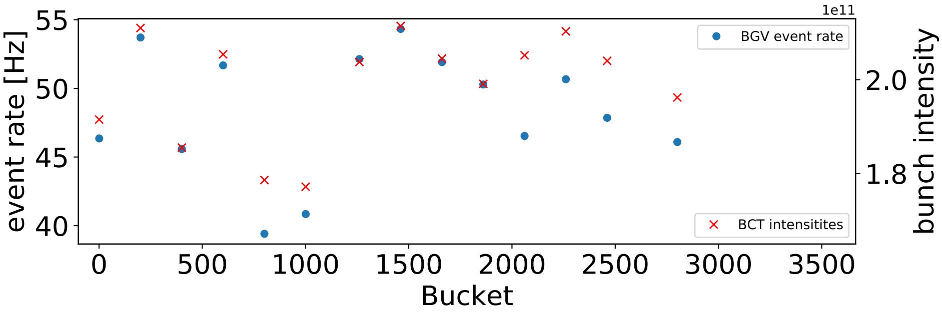

FIGURE 6.3: Event rate per bunch for fill 7377 with 14 bunches. In comparison to the full LHC fill the per bunch rate is significantly higher. The rate shown here corresponds to the event rate after filtering. The red crosses are the intensity values taken from the BCT for the corresponding fill.

For fills with too many bunches for the available bandwidth the bunches need to be selected in advance to dedicate the full BGV readout bandwidth to them. The bunch selection should be performed at the trigger level i.e. a L0 trigger is only accepted if it coincides with a chosen bunch number. Sadly this could not be achieved during the runtime of the BGV so the selection needed to be done using the HLT which led to an unnecessary increase in deadtime and a decrease of the event rate.

The event rate per bunch is fundamentally limited by the beam-gas interaction rate in the chamber. Additionally not every interaction creates a valid trigger or passes the HLT filters reducing the event rate further. Using the final event rate the achievable precision per bunch needs to be predicted as described previously.

A more severe problem for bunch by bunch measurements is the reduction of triggers for consecutive bunches as described in the previous section. This is very visible in figure 6.4 where a subset of 96 bunches was selected out of 852 but the consecutive bunches produce different trigger rates despite their very similar intensities measured by the BCT.

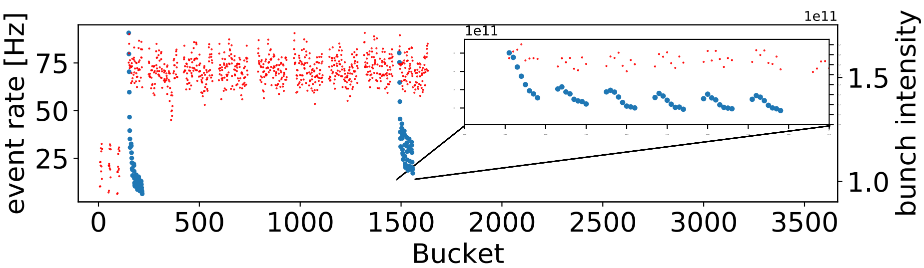

FIGURE 6.4: Event rate per bunch for fill 7365 with a selection of 96 bunches out of 852 injected. Here the reduction of the rate for the later bunches in a train is again visible. Again the BCT values are plotted for comparison showing no such behaviour.

Overall, bunch by bunch measurements with the BGV are possible but to take full advantage of the system the dead time of the trigger needs to be significantly reduced and additional computing and network capacity need to be added to the HLT to allow for a higher number of bunches to be measured at once.

6.2 Types of beam

6.2.1 LHC standard proton beam

Proton acceleration is the most common scenario for the LHC thus the BGV was mostly used in that environment and a very thorough optimization of all parameters was performed during the three years of Run2.

The configuration of the LHC beam was not the same for all years due to adaptations performed by the LHC operations team. In 2017 a standard fill had 1836 bunches with 1.1×10^{11} protons each. For 2018 the maximum number of bunches was increased to 2556 with the same intensity.

6.2.2 BSRT calibration fill

As described in section 2.4.2 on page 18 the BSRT needs to be cross-calibrated with the wire scanner to provide accurate measurements [24]. During this procedure the magnification as well as the resolution (line spread function, LSF) of the BSRT are determined.

To perform this calibration a special fill is injected into the LHC containing 12 bunches of defined different emittances to cover a wide range of possible measurement values. During this type of fill the wire scanner is measuring every 30 s allowing for an in-depth comparison during all stages of the acceleration cycle.

Fill 7220 of the LHC is such a fill at a point in time where the BGV was fully operational. During this fill bunches with almost nominal intensity (1.1×10^{11} protons) were injected with emittances from 1 µm to 4 µm. This allowed to measure multiple different emittances at the same time and perform comparisons with both the expected and measured values. For this fill the BGV was only parasitically using the beam by taking data while the actual calibration of the BSRT was performed. A comparison of the BGV data to the BSRT is therefore not really feasible since the calibration influences the results provided by the BSRT.

At the same time a comparison to the WS measurements is possible and allows to understand the results with respect to each other. The results of this comparison are given in section 6.4.1 on page 71.

6.2.3 Machine Development

Machine Development (MD) runs are performed regularly to test new parameters or operation modes of the accelerators. They offer the opportunity to measure bunches with different emittances, different bunch spacing, intensities and other specialities such as long injection energy runs to measure the emittance blowup. During the MD in October of 2018 the BGV acquired data for multiple fills, the results of which are presented in this section.

MD4510

The first result presented here is from MD4510, which was testing beam lifetime optimization. Due to the procedures performed there should be three emittance and therefore beam size blow-ups visible, which were observed with the BGV and can be seen in figure 6.5.

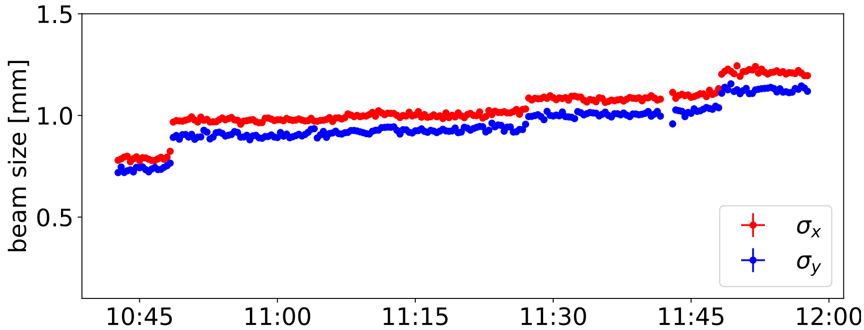

FIGURE 6.5: Fill 7347 for MD4510 for beam liftetime optimization at injection. Three jumps in beam size are visible when actions were taken by the operators.

MD4507

Another interesting MD fill was Fill 7336 for MD4507 where the aim was to compare two ramping procedures with each other. The data taken with the BGV shows, that the emittances in horizontal and vertical direction differed significantly. This allows to check and confirm the fit method which can also provide the rotation angle as discussed in section 5.2.4 on page 58. The expected result is a non-rotated beam with significantly different horizontal and vertical beam size (see figure 6.6a) and a non-rotated beam shape which can be seen in figure 6.6b.

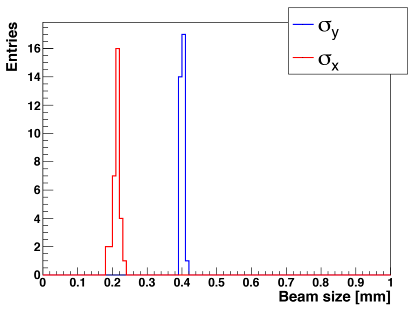

(A) Beam sizes

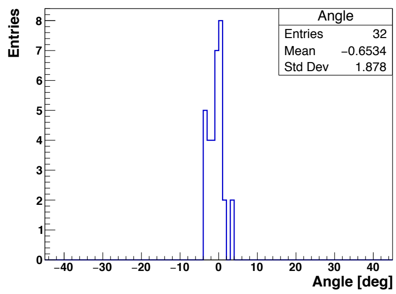

(B) Rotation angle of the measured beam ellipse

FIGURE 6.6: Shows the results from Fill 7336 for MD4507 which allowed to use the elliptical fit method to measure the rotation of the beam ellipse.

This plot also shows, that the three parameter fit cannot distinguish between x and y in an absolute way due to the mathematical equivalency of a beam rotated by $\frac{\pi}{2}$ with swapped axis as discussed in section 5.2.4 on page 58. Looking at the results of the two individual two parameter fits reveals, that the expected values are $\sigma_x = 400\,\mu m$ and $\sigma_y = 200\,\mu m$ which is also confirmed by the BSRT measurement.

Therefore the results always need to be cross-checked with another method and the angle result needs to be adapted if necessary.

Furthermore this fill allows to investigate the trigger rate for single LHC bunches. The injected intensities of fill 7336 were 1.98×10^{11} protons per bunch. The L0 trigger rate for 14 bunches with this intensity was 1200 Hz which gives about 85 Hz of L0 trigger per bunch. In figure 6.7 the per bunch trigger rate after HLT filtering is plotted showing a data reduction by around 35 %.

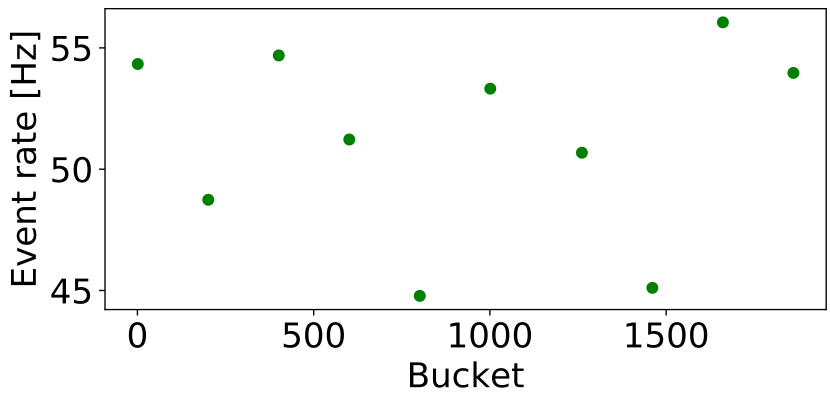

FIGURE 6.7: Shows the frequency of events with two or more tracks as recorded by the HLT for individual bunches in fill 7336.

Using the data rate of about 50 Hz and the requirement for bunch by bunch measurements to be done within one minute we arrive at 3000 events recorded. The absolute precision of these measurements, as given by figure 5.14a on page 62, is around 25 µm for a 220 µm beam. This is much more than the expected 5 % precision given by the design goal. To achieve the design goal the data rate would need to be around 200 Hz or in other words the data rate would need to match the interaction rate in the volume.

MD3270

Yet another MD interesting for the BGV was the Fill 7362 for MD3270 which was aimed at testing a new ramping procedure. To that end 157 bunches were injected in a 1, 12, 3x48 configuration. Each of the trains with 48 bunches consisted of 6x8 bunches. The plots in figure 6.8 on the next page show the results from that fill with (a) showing the result when integrating over each train and (b) showing when only accumulating the data for each block of 8 bunches (or 12 in the case of the first injected train).

6.2.4 Ion beam measurements

During November 2018 the LHC was operating in ion beam mode enabling the study of the BGV with respect to ion beams. The first significant observation was the difference in collision products showing as a difference in cluster multiplicity (figure 6.9 on the facing page).

Consequently the cluster thresholds for the selection of events in the HLT needed to be updated to better represent the expected cluster multiplicity.

The most significant change is the increase of the per module cluster threshold from 50 to 150. Additionally the total cluster acceptance is increased slightly from

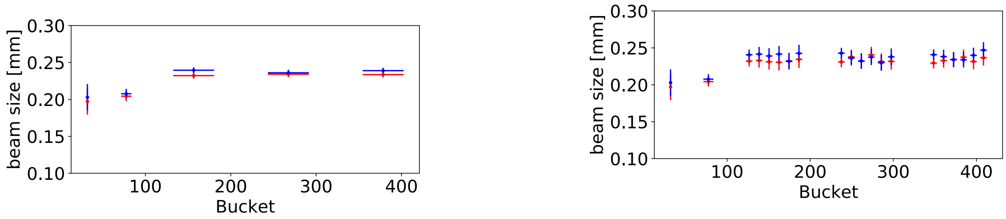

(A) The 4 trains average size

(B) Size of the 8 bunch large sequences in the 48 bunch trains.

FIGURE 6.8: Shows the beam size measurement at 6.5 eV from Fill 7362 for MD3270 which allowed for the bunch by bunch and train by train study of BGV measurements. The horizontal errorbar gives the range of bunches integrated over.

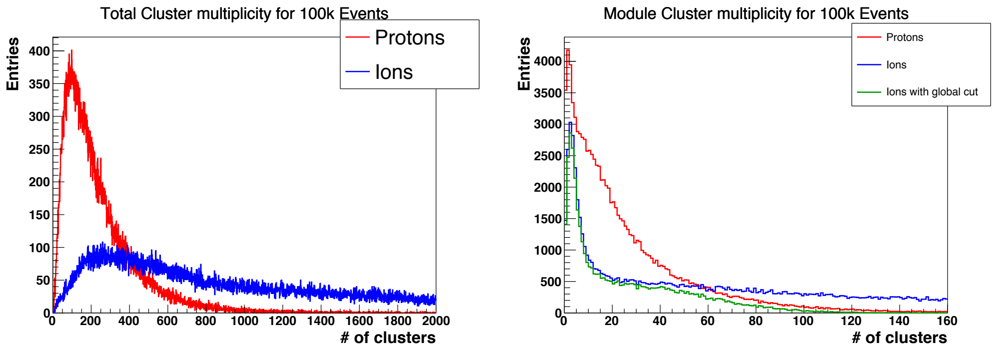

(A) Total cluster multiplicity

(B) Cluster multiplicity per module

FIGURE 6.9: Comparisons of cluster multiplicities for protons and ions for a sample of 100k unfiltered events.

400 to 640. This has an insignificant effect on the low cluster count events but reduces the per module cluster cut to a similar level as for protons (see green curve in figure 6.9b).

The upper limit on the total cluster acceptance increases the computation time due to the higher number of possible combinations to be checked by the pattern recognition algorithm without at the same time increasing the number of tracks found by an equivalent amount. It is therefore a parameter that needs to be increased with care to prevent runtime increases with no improvement to the measurement.

6.3 Emittance measurements

Measuring the beam emittance and by extension the normalized beam emittance is one of the main goals of beam profile monitors. Using equation 2.58 in section 2.1.6 the normalized emittance can be calculated by knowing the local beam size, beta function and energy. The results of some selected fills where the emittance was calculated are presented in this section. Additional emittance comparison plots are given in the following section where the BGV is compared to other beam size measurements on the basis of the normalized emittance.

6.3.1 Emittance blow-up at injection

The emittance of the beam circulating in the LHC increases at injection energies, mostly due to intra beam scattering, by approximately 10 % within 20 minutes. A detailed explanation of all effects and countermeasures can be found in [47, 48]. Since the filling procedure itself requires a certain amount of time (around 30 min) this effect always occurs. To limit the blow-up to the lowest level the ramp of the LHC is usually started as soon as possible after the last train has been injected. Due to limitations with the BGV software it was never possible to acquire data before the filling procedure was completed. Consequentially the BGV could never measure this effect during normal conditions.

For LHC fill 7334, the last proton fill of Run 2, the energy ramp was delayed by almost 20 minutes allowing for the BGV to take sufficient amounts of data at injection energy to record this effect as shown in figure 6.10.

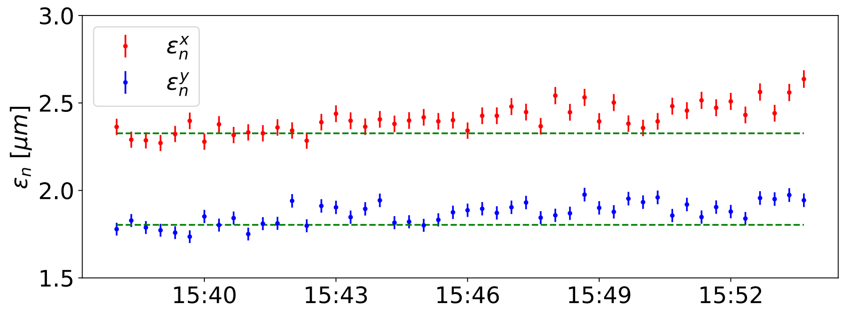

FIGURE 6.10: Emittance blow-up at injection energy of Fill 7334.

The same blow-up is also visible in the full dataset shown in figure 6.12 on the next page.

6.3.2 Emittance evolution during ramp

The physical size of the beam shrinks during acceleration due to adiabatic damping [4]. Assuming a constant normalized emittance this change is given by

$$\sigma(E) = \sigma_{\text{inj}} \sqrt{E_{\text{inj}}/E}. \tag{6.1}$$

As can be seen in figure 6.11 the beam size measured by the BGV follows this expected behaviour quite nicely.

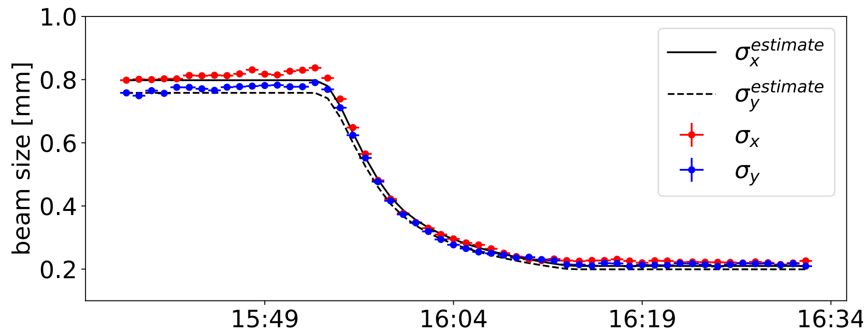

FIGURE 6.11: Beam size evolution before, during and after the energy ramp for LHC Fill 7334.

Calculating the emittance from the beam size using the beta function at the location of the BGV gives the emittance evolution (figure 6.12). The emittance blow up at injection energy, described in the previous section, is again visible in the first 20 minutes of the ramp. Once the ramp, indicated by the solid black line, starts, the emittance begins to behave unphysically. This is caused by a changing beta function which is not precisely known and can therefore not be corrected for. Once top energy is reached the beta function stabilizes and the emittance result is reliable again.

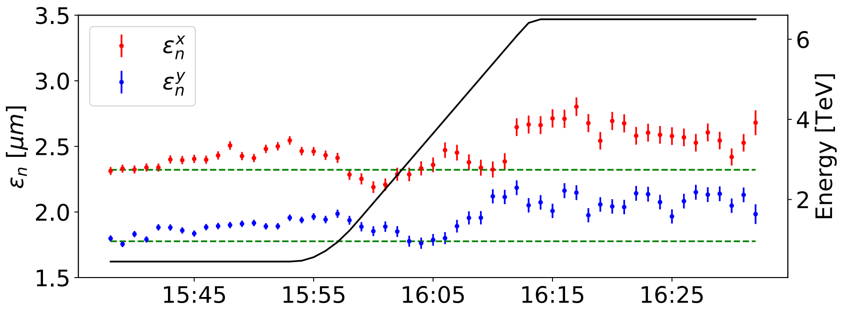

FIGURE 6.12: Emittance evolution before, during and after the energy ramp for LHC Fill 7334.

6.3.3 Long term emittance evolution of ion beam

The emittance of ion beams exhibits a different behaviour than proton beams which can be interesting to study. Due to the higher charge number of the ions the radiation dampening of the beam is twice as high as for protons [49]. One therefore expects to see a difference in the long term behaviour of the emittances of ion beams in comparison to proton beams. The increased dampening is beneficial to the emittance preservation in the LHC leading to a decrease over time which increases the luminosity. The effect of intra-beam scattering on the other hand is detrimental to the emittance and leads to an increase. Since the IBS is significantly lower for the vertical emittance a shrinkage is visible in figure 6.13 on the following page while the horizontal emittance stays constant due to both effects compensating each other [50].

6.4 Comparison with other monitors

Beam size measurement devices are located at different positions along the LHC ring. To allow their results to be compared they need to be normalized using their local beta function value given by the beam optics to calculate the emittances as given by equation (2.55) on page 10. This approach is valid for any scenario where the energy does not change, for the situation of changing energy equation (2.58) on page 11 needs to be used.

6.4.1 BGV vs Wire scanner

The wire scanner scanner is considered the most precise measurement device installed in the LHC as of now. Due to the nature of its principle of operation it cannot be used during fills with more than 12 bunches. It is therefore mostly used to check the pilot bunch and the first 10 bunches of each LHC fill before handing over to the

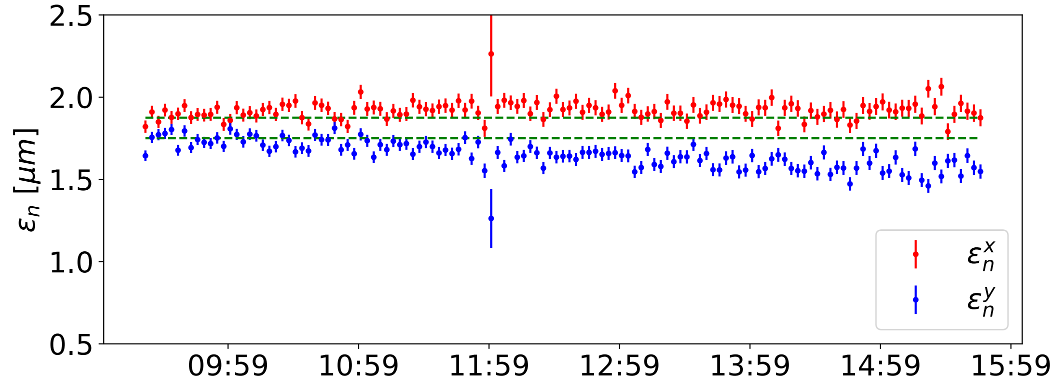

FIGURE 6.13: Shows the decrease of the vertical emittance at flat top energy (6.3 TeV) of lead ion LHC Fill 7486 during six hours of data acquisition with 180 s of integration time per measurement. The dashed line denotes the expected constant emittance extrapolated from the first five measurements. The measurement with large error bars indicates the point where the gas injection needed to be restarted.

BSRT for continuous measurements. A comparison of the BGV with the wire scanner is therefore only possible during the first few minutes of an injection or during special runs such as the BSRT calibration run as described in section 6.2.2 on page 66. Fill 7220 is used here to show the comparisons between the BGV and WS measurements.

As described in section 2.4.1 on page 17, measurements with the wire scanner are performed by measuring the intensity of secondary particles with respect to the position of the wire passing through the beam. When multiple bunches are circulating in the LHC they are all measured at once and then separated by using timing information. By plotting the intensity vs the position of the wire (e.g. figure 6.14a) the distribution of the protons in the beam, with respect to the axis the wire passed through, is measured. A gaussian fit to this profile gives the beam size as σ_{WS}. Plotting this sigma over time gives the beam size evolution at the location of the wire scanner before, during and after the ramp (figure 6.14b).

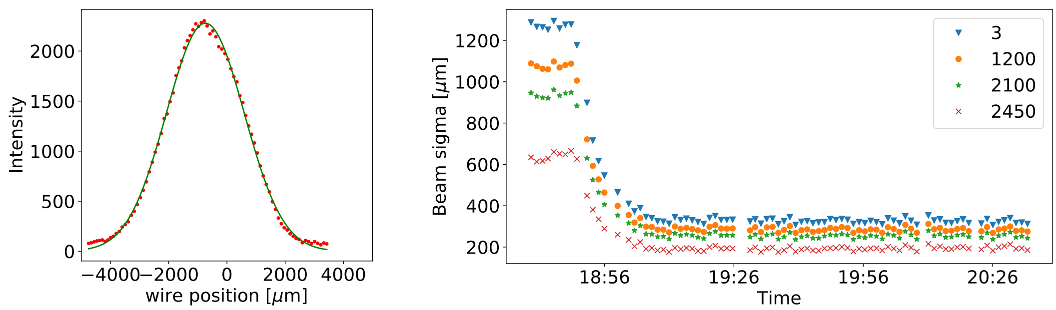

(A) Intensity measurement of wire scanner vs wire position

(B) Sigma of the horizontal intensity measurements over time for four selected bunches.

FIGURE 6.14: Wire scanner measurements for fill 7220 taken directly from the raw data stored in the logging database. The expected shrinking of the beam size happens during the energy ramp.

To compare the measurements of the WS with the BGV they need to be converted to normalized emittances using equation (2.58) on page 11. For this fill the injected emittances were chosen to be 4 µm for bunch 3, 3 µm for bunch 1200, 2 µm for bunch 2100 and 1 µm for bunch 2450. Figures 6.15 and 6.16 show the horizontal and vertical emittance over time measured by the BGV and WS in comparison to the intended injection emittance as a dashed line.

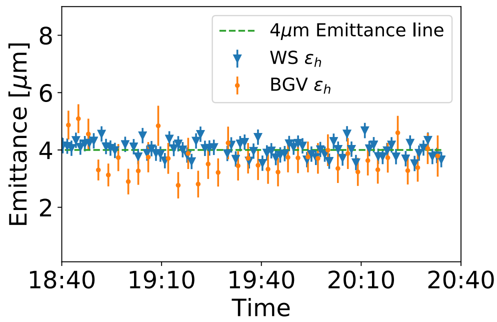

(A) 4 µm (bunch 3)

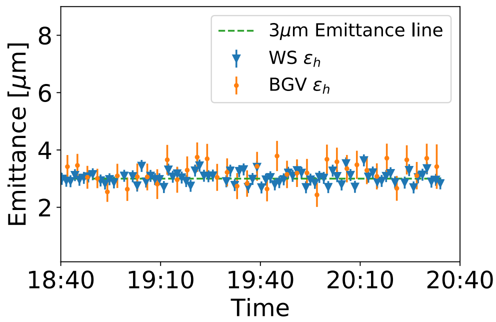

(B) 3 µm (bunch 1200)

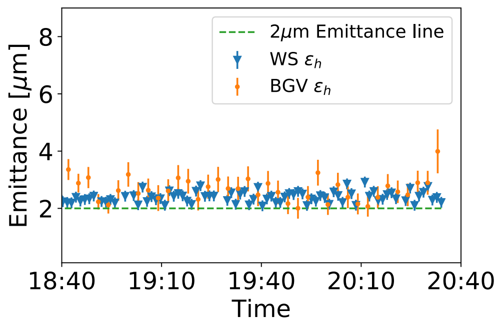

(C) 2 µm (bunch 2100)

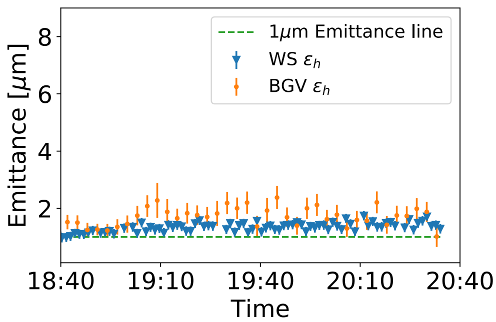

(D) 1 µm (bunch 2450)

FIGURE 6.15: Measured horizontal emittances for four bunches of different emittances during the BSRT calibration run.

Additionally figure 6.17b on the following page shows the comparison of the vertical emittances of all bunches in the fill.

6.4.2 BGV vs BSRT

The BSRT is currently the only other device installed in the LHC capable of performing continuous non-invasive beam size measurements. It is therefore the prime candidate for a comparison with the BGV results. Again, as with the wire scanners, the best way to compare the results of the two devices is to compare the normalized emittances. By doing that the results of both devices are processed in a similar manner and need to have the same propagated errors applied. The propagated errors take into consideration the fact that the measurement of both the device and the β function at it's location have a certain precision. For the BGV the precision depends on the number of events as previously established in section 5.3 on page 59. The error of the BSRT is estimated to be around 7 %. Additionally the BSRT is prone to a loss in accuracy due to drifts of the optics system necessitating frequent recalibrations. This effect is visible in the following results.

After comparing these results it is immediately apparent that the results coincide very well for the vertical measurement but don't do so for the horizontal. Looking at the WS results in figure 6.17a on the facing page a similar behaviour can be observed for the bunches with 1 µm emittance.

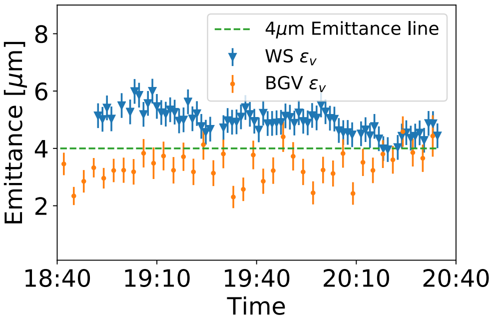

(A) 4 μm (bunch 3)

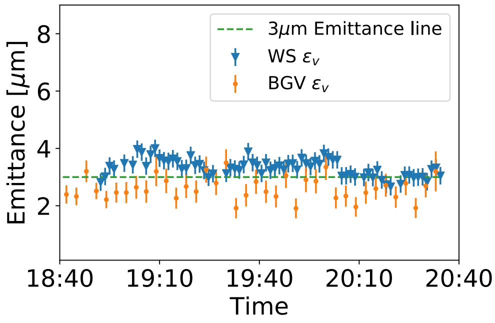

(B) 3 μm (bunch 1200)

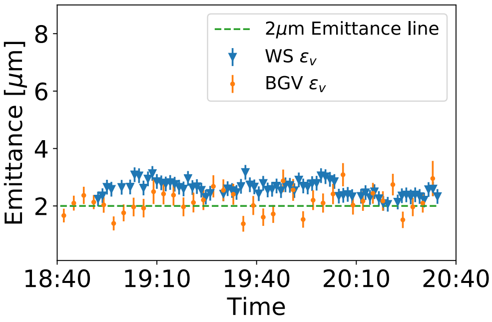

(C) 2 μm (bunch 2100)

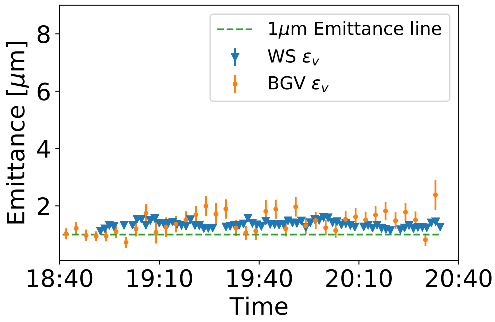

(D) 1 μm (bunch 2450)

FIGURE 6.16: Measured vertical emittances for four bunches of different emittances during the BSRT calibration run.

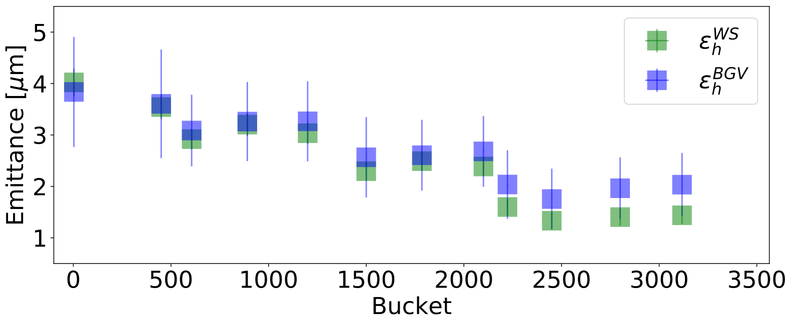

(A) horizontal

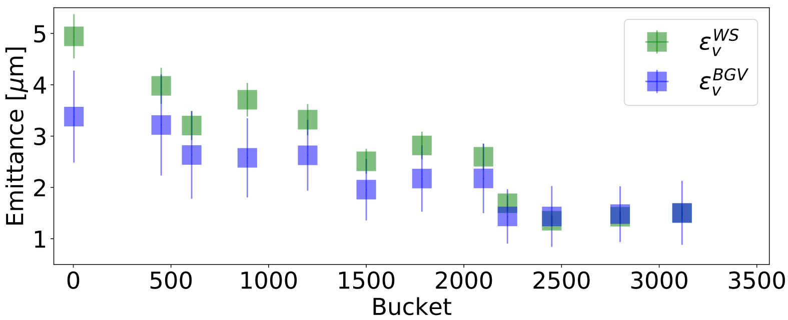

(B) vertical

FIGURE 6.17: Comparison of all bunches in fill 7220 with the design sizes of 2x4 μm 3x3 μm, 3x2 μm and 4x1 μm.

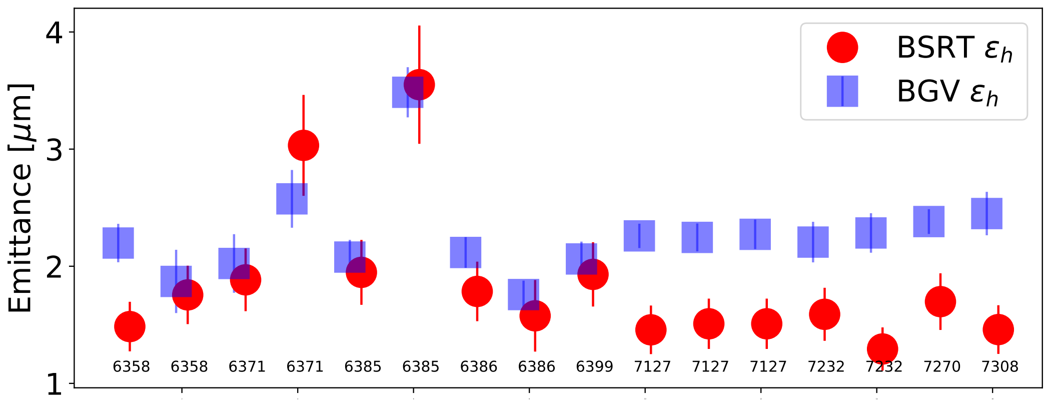

FIGURE 6.18: Horizontal beam size measurements of the BGV compared to the equivalent BSRT measurements for multiple fills and beam types. The number at the bottom indicates the number of the fill.

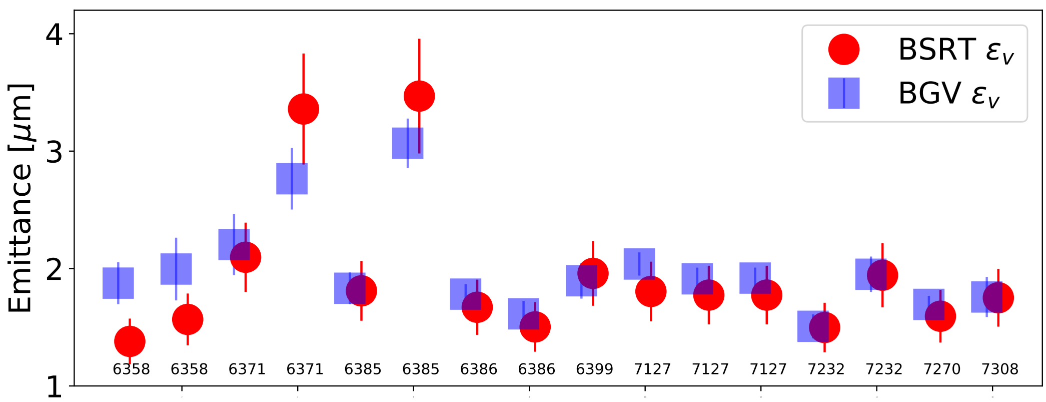

FIGURE 6.19: Vertical beam size measurements of the BGV compared to the equivalent BSRT measurements for multiple fills and beam types. The number at the bottom indicates the number of the fill.

Chapter 7

Summary and Outlook

7.1 Summary

The results obtained with the BGV over the course of 2 years of data taking have been presented in this thesis. To achieve these results, thorough studies of the data acquired with the BGV were performed and relevant parameters optimized.

Furthermore the correlation method was picked up as an alternative to the vertexing algorithm when it became apparent that the setup could not provide the required data at sufficient rate. The implementation and verification of the algorithm coupled with the alignment of the detector represent the brunt of the work performed. Using this algorithm it was possible to provide precise and, with the help of the correction, also accurate results using the data provided by the BGV. The design goal of achieving 2 % average beam size resolution within one minute was successfully shown.

The goal of achieving 5 % bunch by bunch resolution for all bunches at the same time could not be shown due to the limited computing capacity available. Using machine development fills, which provided the opportunity to perform this measurement with a reduced number of bunches, it was shown that the measurement is not possible with the current setup due to a too low trigger rate.

Overall the BGV has fulfilled its goal of providing fast, non-invasive beam size measurements. Additionally it allowed for many studies to be performed and many insights into the applicability of the BGV as a beam instrumentation device. The already ongoing design process for a future beam gas beam-size monitor is influenced significantly the knowledge gained during this study [51] and will continue to be by running the BGV again during Run3.

7.2 Towards the final system

Since the BGV was designed to be a demonstrator to investigate the feasibility of the method and learn more about possible optimizations here are a few key lessons learned:

A precise alignment, as with every other tracking detector, is extremely important for the accuracy and precision of the results provided by the BGV. The alignment as it was performed by me was hindered a lot by the lack of a reference frame which is why I would strongly suggest the use of at least three tracking stations in any future design. The alignment could possibly have been performed better using some form of alignment algorithm like Millepede but the time required to understand and implement this procedure was not available in the time allotted for this thesis.

Multiple scattering is currently the main limit to all of the BGVs measurements. The MS introduced by the exit window in combination with the MS in the first detector layer limits the distance of extrapolation in the gas target volume on the basis of extrapolation errors. Investigations into a thinned exit window and detectors with a lower radiation length could yield significant improvements in these areas, allowing for a higher tracking precision. As a part of this an investigation in the distances between the tracking planes should be performed to optimize their positions along the z-axis.

Following from the results shown in this thesis it has become apparent that a 2 m long gas volume is not aiding the beam size measurement goal since the extrapolation error becomes larger than the beam size to be measured. A possible way of mitigating this would be to decrease the length of the volume while at the same time increasing the pressure accordingly. When looking at the interaction rate given by equation (3.5) on page 23 we see that $R \propto p \cdot z$ and therefore the factor of reduction for the length is also the factor the gas pressure needs to be increased by to keep the rate the same. The actual scenario is a bit more complicated due to the interactions close to the exit window not being in the coverage of the detector.

A second approach to this problem is the introduction of a gas-jet as is already being investigated by other projects such as the Beam Gas Curtain (BGC) detector [52, 53]. Such a gas-jet would allow for a large localized increase in pressure leading to an equivalent interaction rate. The benefit would be, that the reconstruction software would have the knowledge of the z-origin of the tracks that it needs to reconstruct. Possible synergies between the BGV and the BGC are currently being investigated [51].

The expectation of having many events with 5 or more tracks originating from the vertex was not observed in the current BGV detector. The applicability of the vertexing method was therefore not given, leading to the reliance on the correlation method.

The fact that the BGV uses components sourced from the LHCb experiment helped it to be constructed and brought up to speed in very short time while being extremely capable. The downside of this reliance on LHCb hardware was that it was designed to be handled by a much larger team of experts and not designed for the single use case as a beam instrumentation device. Although the experts were available for us throughout Run 2 the basic design of the readout electronics was not designed for some BGV applications which is something not easily changed. It was, for example, not easily possible to choose only a subset of Buckets to take data for or change this value easily between two datasets. Additionally the LHCb system was of course not designed to take data before the injection was finished leading to multiple issues with the BGV where we would have liked to do this.

During Run2 the BGV trigger was updated by adding a constant fraction discriminator to the readout in the hope of improving the timing performance of the L0 trigger. What was overlooked in that process and decision was the significant dead-time introduced by the CFD leading to the uneven triggering shown in section 6.1.2 on page 63. A possible change would be to revert back to the old system and accept the slightly worse time resolution instead of introducing unnecessary downtime. This is especially interesting as one of the easiest possible upgrades to the BGV was an increase in processing capacity by adding more computing blades. Now, after the end of Run2, 9 additional CPU blades have been added to the HLT which should lead to significantly reduced computing times during Run3.

Bibliography

[1] G. Apollinari et al. *HL-LHC Preliminary Design Report: Deliverable: D1.5*. Tech. rep. Geneva, Switzerland: CERN, Nov. 2014. URL: https://cds.cern.ch/record/1972604 (cit. on pp. 1, 16).

[2] Colin Barschel. "Precision luminosity measurement at LHCb with beam-gas imaging". Presented 05 Mar 2014. 2014. URL: http://cds.cern.ch/record/1693671 (cit. on p. 1).

[3] A. Einstein. "Ist die Trägheit eines Körpers von seinem Energieinhalt abhängig?" In: *Annalen der Physik* 323 (1905), pp. 639–641. DOI: 10.1002/andp.19053231314 (cit. on p. 3).

[4] Donald A Edwards and Michael J Syphers. *An introduction to the physics of high energy accelerators*. Wiley Beam Phys. Accel. Technol. New York, NY: Wiley, 1993. URL: https://cds.cern.ch/record/249993 (cit. on pp. 5, 6, 10, 70).

[5] G. W. Hill. "On the part of the motion of the lunar perigee which is a function of the mean motions of the sun and moon". In: *Acta Math.* 8 (1886), pp. 1–36. DOI: 10.1007/BF02417081. URL: https://doi.org/10.1007/BF02417081 (cit. on p. 7).

[6] E D Courant and H S Snyder. "Theory of the Alternating-Gradient Synchrotron". In: *Ann. Phys.* 3 (1958), pp. 1–48. URL: https://cds.cern.ch/record/593259 (cit. on p. 8).

[7] M. Tanabashi et al. "Review of Particle Physics". In: *Phys. Rev. D* 98 (3 Aug. 2018), p. 030001. DOI: 10.1103/PhysRevD.98.030001. URL: https://link.aps.org/doi/10.1103/PhysRevD.98.030001 (cit. on pp. 11, 23).

[8] M A Hone. *The duoplasmatron ion source for the new CERN Linac preinjector*. Tech. rep. CERN-PS-LR-79-37. Geneva: CERN, Nov. 1979. URL: http://cds.cern.ch/record/2640736 (cit. on p. 13).

[9] E Boltezar et al. *The new CERN 50 MeV Linac*. Tech. rep. CERN-PS-LR-79-28. Geneva: CERN, Sept. 1979. URL: https://cds.cern.ch/record/2640695 (cit. on p. 13).

[10] Karlheinz Schindl. *The PS Booster as Pre-Injector for LHC*. Tech. rep. CERN-PS-97-011-DI. Geneva: CERN, Apr. 1997. URL: https://cds.cern.ch/record/323757 (cit. on p. 13).

[11] *CERN's 25 GeV proton synchroton*. Geneva: CERN, 1960. URL: https://cds.cern.ch/record/445034 (cit. on p. 13).

[12] R Garoby. "RF Gymnastics in Synchrotrons". In: CERN-PS-2000-022-RF (June 2000), 16 p. URL: https://cds.cern.ch/record/446600 (cit. on p. 13).

[13] Michael Benedikt et al. *LHC Design Report v.3 - LHC Injector Chain*. CERN Yellow Reports: Monographs. Geneva: CERN, 2004. URL: https://cds.cern.ch/record/823808 (cit. on p. 13).

[14] Oliver Sim Brüning et al. *LHC Design Report v.1 - LHC Main Ring*. CERN Yellow Reports: Monographs. Geneva: CERN, 2004. URL: https://cds.cern.ch/record/782076 (cit. on pp. 14, 24).

[15] Carlo Wyss. *LEP design report, v.3: LEP2*. Vol. 1-2 publ. in 1983-84. Geneva: CERN, 1996. URL: https://cds.cern.ch/record/314187 (cit. on p. 14).

[16] R Bailey and Paul Collier. *Standard Filling Schemes for Various LHC Operation Modes*. Tech. rep. LHC-PROJECT-NOTE-323. Geneva: CERN, Sept. 2003. URL: http://cds.cern.ch/record/691782 (cit. on p. 15).

[17] J B Jeanneret et al. *Quench levels and transient beam losses in LHC magnets*. Tech. rep. LHC-Project-Report-44. CERN-LHC-Project-Report-44. Geneva: CERN, May 1996. URL: http://cds.cern.ch/record/308241 (cit. on p. 15).

[18] M Lamont et al. "Betatron squeeze: status, strategy and issues. Squeeze. strategy and issues". In: (2010). DOI: oai:cds.cern.ch:1281622. URL: https://cds.cern.ch/record/1281622 (cit. on p. 15).

[19] Reyes Alemany, Mike Lamont, and Stephen Page. *LHC modes*. Tech. rep. Functional specification LHC MODES. Geneva, Switzerland: CERN, 2007 (cit. on p. 15).

[20] Jacques Bosser and Claude Bovet. *Wire Scanners For LHC*. Tech. rep. LHC-Project-Note-108. revised version number 1 submitted on 2001-11-13 14:37:03. Geneva: CERN, Sept. 1997. URL: https://cds.cern.ch/record/692054 (cit. on p. 18).

[21] M Sapinski. "Beam Interaction with Thin Materials: Heat Deposition, Cooling Phenomena and Damage Limits". In: *Conf. Proc.* C1204151.CERN-ATS-2012-155 (Apr. 2012), WECP04. 5 p. URL: https://cds.cern.ch/record/1461301 (cit. on p. 18).

[22] Maria Kuhn, Joerg Rossbach, and Verena Kain. "Emittance Preservation at the LHC". Presented 05 Apr 2013. Mar. 2013. URL: https://cds.cern.ch/record/1544573 (cit. on p. 18).

[23] Hideo Onuki. *Wigglers, undulators and their applications*. Abingdon: CRC Press, 2002. URL: https://cds.cern.ch/record/898667 (cit. on p. 19).

[24] Georges Trad, Jean-Marie De Conto, and Federico Roncarolo. "Development and Optimisation of the SPS and LHC beam diagnostics based on Synchrotron Radiation monitors". Presented 22 Jan 2015. Oct. 2014. URL: https://cds.cern.ch/record/2266055 (cit. on pp. 19, 66).

[25] P. Hopchev et al. "A Beam Gas Vertex Detector for Beam Size Measurement in the LHC". In: *Proc. 5th International Particle Accelerator Conference (IPAC'14), Dresden, Germany, June 15-20, 2014* (Dresden, Germany). International Particle Accelerator Conference 5. https://doi.org/10.18429/JACoW-IPAC2014-THPME175. Geneva, Switzerland: JACoW, July 2014, pp. 3680–3683. ISBN: 978-3-95450-132-8. DOI: https://doi.org/10.18429/JACoW-IPAC2014-THPME175. URL: http://jacow.org/ipac2014/papers/thpme175.pdf (cit. on p. 21).

[26] J. Carvalho. "Compilation of cross sections for proton–nucleus interactions at the HERA energy". In: *Nuclear Physics A* 725 (2003), pp. 269 –275. ISSN: 0375-9474. DOI: https://doi.org/10.1016/S0375-9474(03)01597-5. URL: http://www.sciencedirect.com/science/article/pii/S0375947403015975 (cit. on p. 23).

[27] B. Dehning et al. *Beam Gas Vertex (BGV) Demonstrator of a Beam Profile Monitor in LHC*. Tech. rep. LHC-BGV-EC-0002 v.1.0. Geneva, Switzerland: CERN, 2014. URL: https://edms.cern.ch/document/1324635/1.0 (cit. on p. 23).

[28] P. Magagnin. *BGV Window Design Report*. Tech. rep. Geneva, Switzerland: CERN, 2015. URL: https://edms.cern.ch/document/1568314/1 (cit. on p. 24).

[29] LHCb Collaboration. *LHCb Tracker Upgrade Technical Design Report*. Tech. rep. CERN-LHCC-2014-001. LHCB-TDR-015. Feb. 2014. URL: https://cds.cern.ch/record/1647400 (cit. on pp. 26, 28).

[30] Axel Kuonen, Olivier Girard, and Guido Haefeli. *Characterisation of the Hamamatsu MPPC multichannel array for LHCb SciFi Tracker v.9.2014*. Tech. rep. 2015-001. Lausanne, Switzerland: EPFL, 2015. URL: https://lphe.epfl.ch/publications/2015/LPHE-2015-001.pdf (cit. on p. 26).

[31] Olivier Goran Girard, Tatsuya Nakada, and Guido Haefeli. "Development of the scintillating fibre tracker technology for the LHCb upgrade and the LHC beam profile monitoring system". Presented 23 Jul 2018. May 2018. URL: https://cds.cern.ch/record/2646587 (cit. on pp. 26, 29, 31, 44).

[32] Valdir Salustino Guimaraes and Murilo Santana Rangel. "Associated vector boson production with b-jets at LHCb and Beam-Gas Vertexing at LHC for beam instrumentation". Presented 27 Apr 2016. Mar. 2012. URL: https://cds.cern.ch/record/2212758 (cit. on pp. 28, 35, 44, 46).

[33] P. Hopchev et al. *Detector Cooling for the BGV Demonstrator in the LHC*. Tech. rep. Engineering Change Request LHC-BGV-EC-0003 v.1.0. Geneva, Switzerland: CERN, 2015. URL: https://edms.cern.ch/document/1439028/1.0 (cit. on p. 28).

[34] S Löchner and M Schmelling. *The Beetle Reference Manual - chip version 1.3, 1.4 and 1.5*. Tech. rep. LHCb-2005-105. CERN-LHCb-2005-105. Geneva: CERN, Nov. 2006. URL: https://cds.cern.ch/record/1000429 (cit. on p. 29).

[35] G. Haefeli et al. "The LHCb DAQ interface board TELL1". In: *Nucl. Instrum. Methods A* 560.2 (2006), pp. 494 –502. ISSN: 0168-9002. DOI: https://doi.org/10.1016/j.nima.2005.12.212. URL: http://www.sciencedirect.com/science/article/pii/S0168900205026100 (cit. on p. 29).

[36] G. Haefeli et al. *Specification note about the TELL1 board*. Tech. rep. Geneva, Switzerland: CERN, 2003. URL: https://edms.cern.ch/document/487730/1 (cit. on p. 29).

[37] O. Girard et al. *BGV fibre module read-out, signal correction and clustering*. Tech. rep. Lausanne, Switzerland: EPFL, 2016. URL: http://lphe.epfl.ch/publications/2016/LPHE-2016-002.pdf (cit. on p. 30).

[38] S. Giani et al. *Digitization of SiPM signals for the LHCb Upgrade SciFi tracker*. Tech. rep. CERN-LHCb-PUB-2014-025. Geneva, Switzerland: CERN, Feb. 2014. URL: https://cds.cern.ch/record/1662549 (cit. on p. 30).

[39] G. Haefeli and A. Gong. *LHCb VELO and ST clusterization on TELL1*. Tech. rep. Lausanne, Switzerland: EPFL, 2006. URL: https://edms.cern.ch/document/690585/3 (cit. on p. 30).

[40] Gloria Corti et al. "Software for the LHCb experiment". In: *IEEE Trans. Nucl. Sci.* 53 (2006), pp. 1323–1328. URL: https://cds.cern.ch/record/913834 (cit. on p. 31).

[41] R. Brun and F. Rademakers. "ROOT: An object oriented data analysis framework". In: *Nucl. Instrum. Meth.* A389 (1997), pp. 81–86. DOI: 10.1016/S0168-9002(97)00048-X (cit. on p. 32).

[42] *GAUSS – The LHCb simulation application*. 2018. URL: http://lhcbdoc.web.cern.ch/lhcbdoc/gauss/ (cit. on p. 40).

[43] M Gyulassy and X. N. Wang. *HIJING Monte Carlo Model*. 1997. URL: http://www-nsdth.lbl.gov/~xnwang/hijing (cit. on p. 40).

[44] Gerald R. Lynch and Orin I. Dahl. "Approximations to multiple Coulomb scattering". In: *Nuclear Instruments and Methods in Physics Research Section B: Beam Interactions with Materials and Atoms* 58.1 (1991), pp. 6 –10. ISSN: 0168-583X. DOI: https://doi.org/10.1016/0168-583X(91)95671-Y. URL: http://www.sciencedirect.com/science/article/pii/0168583X9195671Y (cit. on p. 44).

[45] S. Donati and L. Ristori. *Measuring beam width and SVX impact parameter resolution*. Tech. rep. CDF-Note-4189. Batavia, USA: FERMILAB, 2003. URL: http://beamdocs.fnal.gov/AD-public/DocDB/ShowDocument?docid=609 (cit. on p. 53).

[46] R. Mankel. *Measurement of the Transverse Beam Line Width Using Impact Parameter Correlations*. Tech. rep. CMS-AN-2010/196. Hambourg, Germany: DESY, 2010 (cit. on p. 53).

[47] Maria Kuhn. "Transverse Emittance Measurement and Preservation at the LHC". Presented 20 Jun 2016. 2016. URL: https://cds.cern.ch/record/2229712 (cit. on p. 70).

[48] V Kain et al. "Emittance preservation". In: (2012), 8 p. DOI: 10.5170/CERN-2012-006.81. URL: https://cds.cern.ch/record/1492580 (cit. on p. 70).

[49] W Fischer and J M Jowett. "Ion Colliders". In: *Rev. Accel. Sci. Technol.* 7.CERN-ACC-2015-0015 (Jan. 2015), 49–76. mult. p. DOI: 10.1142/S1793626814300047. URL: http://cds.cern.ch/record/1983191 (cit. on p. 71).

[50] John M Jowett et al. "Limits to the Performance of the LHC with Ion Beams". In: LHC-Project-Report-772. CERN-LHC-Project-Report-772 (Aug. 2004). revised version submitted on 2004-10-21 11:24:16, 4 p. URL: http://cds.cern.ch/record/791378 (cit. on p. 71).

[51] R. Kieffer et al. "The Beam Gas Vertex Profile Monitoring Station for HL-LHC". In: *Proc. 10th International Partile Accelerator Conference (IPAC'19), Melbourne, Australia, 19-24 May 2019* (Melbourne, Australia). International Partile Accelerator Conference 10. https://doi.org/10.18429/JACoW-IPAC2019-WEPGW082. Geneva, Switzerland: JACoW Publishing, June 2019, pp. 2672–2675. ISBN: 978-3-95450-208-0. DOI: doi:10.18429/JACoW-IPAC2019-WEPGW082. URL: http://jacow.org/ipac2019/papers/wepgw082.pdf (cit. on pp. 77, 78).

[52] Hao Zhang et al. "A Supersonic Gas-Jet Based Beam Induced Fluorescence Prototype Monitor for Transverse Profile Determination". In: CERN-ACC-2017-278 (2017), MOPAB139. 4 p. DOI: 10.18429/JACoW-IPAC2017-MOPAB139. URL: http://cds.cern.ch/record/2289127 (cit. on p. 78).

[53] Hao Zhang et al. "A Supersonic Gas Jet-Based Beam Profile Monitor Using Fluorescence for HL-LHC". In: (2018), WEPAF034. 4 p. DOI: 10.18429/JACoW-IPAC2018-WEPAF034. URL: http://cds.cern.ch/record/2667530 (cit. on p. 78).

Benedikt WÜRKNER

Bloch-Bauer-Promenade 24
1100 Wien
+43664 569 7770
b.wuerkner@gmail.com

Education and Qualifications

CERN, European Organization for Nuclear Research, Geneva, Switzerland

- **Doctoral Student** in the Beam Instrumentation Group. 2016-2019
  Measurement of the LHC beam profile using the Beam Gas Vertex detector

TU Wien, Vienna University of Technology

- **Master** in Physical Measurement and Energy Engineering 2012-2015
  Analysis of silicon strip sensor data with focus on determining the sensor resolution

- **Bachelor** in Physical Engineering 2008-2012
  Development of the control software for a high-quality vacuum system.

Loughborough University, United Kingdom

- Exchange Semester 02/2013 – 06/2013

Associated Experiences

TTTech Auto AG, Vienna

Software Developer 10/2019 – present

Helwo GmbH, Vienna

Freelancer in a small marketing company 2010 – 02/2016

- Linux system administration
- HTML, CSS, JavaScript, jQuery
- PHP & MySQL, Python

HEPHY, Institute of High Energy Physics of the Austrian Academy of Sciences, Vienna

Development of a control interface running in an ARM based Linux environment using GPIO, 1Wire, EIB/KNX — 04/2016 – 06/2016

Main developer of the construction database for the VXD of the Belle II experiment — 06/2014 – 01/2016

- PHP5 and MySQL database environment
- Based on the cakePHP MVC framework

Other Experiences

Buddynetwork (ESN), Vienna

Member (and later on Treasurer) of a student association taking care of exchange students — 09/2013 – 06/2016

Languages

German	Mother tongue
English	C2, working language
French	B1, three years of living in a French speaking environment

Technical Skills

- Experience with all three major operating systems: Windows, macOS, Linux
- Proficient in Python including knowledge of a plethora of scientific packages like numpy, pandas, scipy,
- Knowledge of multiple additional programming languages including PHP, JavaScript, HTML and C++
- Knowledge of GIT and distributed development
- Proficiency in bash and related subjects (e.g. command line)
- Familiar with server hardware and software

Personal Interests

- Avid volleyball player with decent skill and a lot of joy
- Snowboarder whenever it is possible